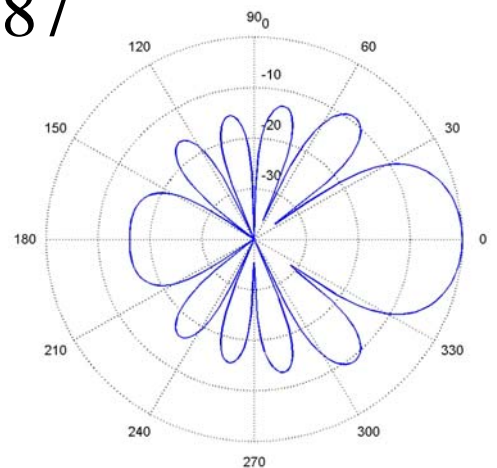
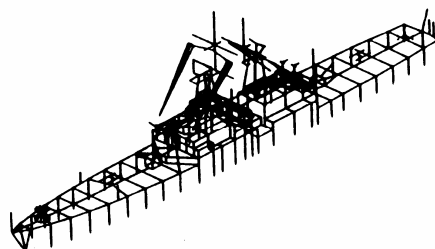
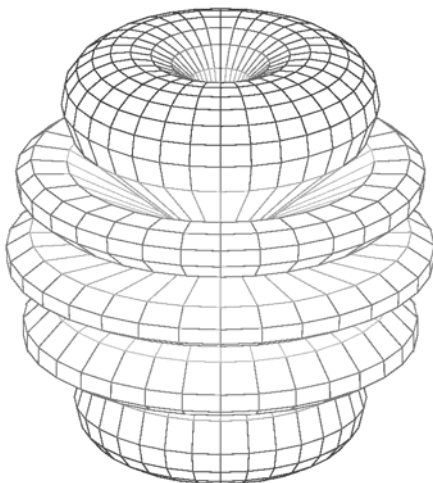
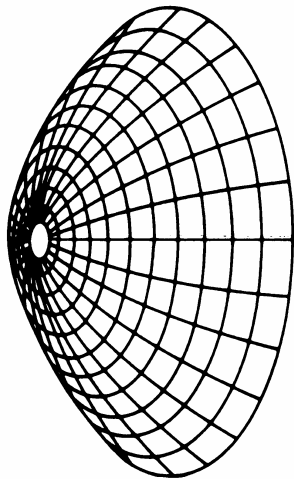
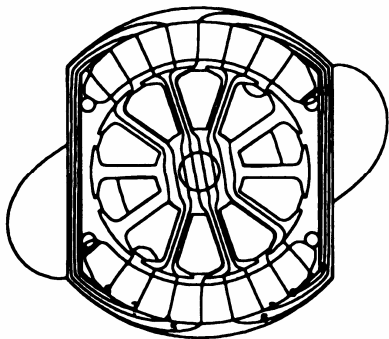


Applied Computational Electromagnetics Society Journal

Special Issue on
ACES 2009 Conference Part II

Guest Editor
Sami Barmada

January 2010
Vol. 25 No. 1
ISSN 1054-4887



GENERAL PURPOSE AND SCOPE: The Applied Computational Electromagnetics Society (*ACES*) Journal hereinafter known as the *ACES Journal* is devoted to the exchange of information in computational electromagnetics, to the advancement of the state-of-the art, and the promotion of related technical activities. A primary objective of the information exchange is the elimination of the need to “re-invent the wheel” to solve a previously-solved computational problem in electrical engineering, physics, or related fields of study. The technical activities promoted by this publication include code validation, performance analysis, and input/output standardization; code or technique optimization and error minimization; innovations in solution technique or in data input/output; identification of new applications for electromagnetics modeling codes and techniques; integration of computational electromagnetics techniques with new computer architectures; and correlation of computational parameters with physical mechanisms.

SUBMISSIONS: The *ACES Journal* welcomes original, previously unpublished papers, relating to applied computational electromagnetics. Typical papers will represent the computational electromagnetics aspects of research in electrical engineering, physics, or related disciplines. However, papers which represent research in applied computational electromagnetics itself are equally acceptable.

Manuscripts are to be submitted through the upload system of *ACES* web site <http://aces.ee.olemiss.edu> See “Information for Authors” on inside of back cover and at *ACES* web site. For additional information contact the Editor-in-Chief:

Dr. Atef Elsherbeni
Department of Electrical Engineering
The University of Mississippi
University, MS 386377 USA
Phone: 662-915-5382 Fax: 662-915-7231
Email: atef@olemiss.edu

SUBSCRIPTIONS: All members of the Applied Computational Electromagnetics Society who have paid their subscription fees are entitled to receive the *ACES Journal* with a minimum of three issues per calendar year and are entitled to download any published journal article available at <http://aces.ee.olemiss.edu>.

Back issues, when available, are \$15 each. Subscriptions to *ACES* is through the web site. Orders for back issues of the *ACES Journal* and changes of addresses should be sent directly to *ACES*:

Dr. Allen W. Glisson
302 Anderson Hall
Dept. of Electrical Engineering
Fax: 662-915-7231
Email: aglisson@olemiss.edu

Allow four week’s advance notice for change of address. Claims for missing issues will not be honored because of insufficient notice or address change or loss in mail unless the Executive Officer is notified within 60 days for USA and Canadian subscribers or 90 days for subscribers in other countries, from the last day of the month of publication. For information regarding reprints of individual papers or other materials, see “Information for Authors”.

LIABILITY. Neither *ACES*, nor the *ACES Journal* editors, are responsible for any consequence of misinformation or claims, express or implied, in any published material in an *ACES Journal* issue. This also applies to advertising, for which only camera-ready copies are accepted. Authors are responsible for information contained in their papers. If any material submitted for publication includes material which has already been published elsewhere, it is the author’s responsibility to obtain written permission to reproduce such material.

APPLIED COMPUTATIONAL ELECTROMAGNETICS SOCIETY JOURNAL

Guest Editor
Sami Barmada

January 2010
Vol. 25 No. 1
ISSN 1054-4887

The ACES Journal is abstracted in INSPEC, in Engineering Index, DTIC, Science Citation Index Expanded, the Research Alert, and to Current Contents/Engineering, Computing & Technology.

The first, fourth, and sixth illustrations on the front cover have been obtained from the Department of Electrical Engineering at the University of Mississippi.

The third and fifth illustrations on the front cover have been obtained from Lawrence Livermore National Laboratory.

The second illustration on the front cover has been obtained from FLUX2D software, CEDRAT S.S. France, MAGSOFT Corporation, New York.

THE APPLIED COMPUTATIONAL ELECTROMAGNETICS SOCIETY
<http://aces.ee.olemiss.edu>

ACES JOURNAL EDITOR-IN-CHIEF

Atef Elsherbeni
University of Mississippi, EE Dept.
University, MS 38677, USA

ACES JOURNAL ASSOCIATE EDITORS-IN-CHIEF

Sami Barmada
University of Pisa, EE Dept.
Pisa, Italy, 56126

Fan Yang
University of Mississippi, EE Dept.
University, MS 38677, USA

ACES JOURNAL EDITORIAL ASSISTANTS

Matthew J. Inman
University of Mississippi, EE Dept.
University, MS 38677, USA

Mohamed Al Sharkawy
Arab Academy for Science and Technology
ECE Dept.
Alexandria, Egypt

ACES JOURNAL EMERITUS EDITORS-IN-CHIEF

Duncan C. Baker
EE Dept. U. of Pretoria
0002 Pretoria, South Africa

Allen Glisson
University of Mississippi, EE Dept.
University, MS 38677, USA

David E. Stein
USAF Scientific Advisory Board
Washington, DC 20330, USA

Robert M. Bevensee
Box 812
Alamo, CA 94507-0516, USA

Ahmed Kishk
University of Mississippi, EE Dept.
University, MS 38677, USA

ACES JOURNAL EMERITUS ASSOCIATE EDITORS-IN-CHIEF

Alexander Yakovlev
University of Mississippi, EE Dept.
University, MS 38677, USA

Erdem Topsakal
Mississippi State University, EE Dept.
Mississippi State, MS 39762, USA

JANUARY 2010 REVIEWERS

Rodolfo Araneo
Giulio Antonini
Sami Barmada
Adalbert Beyer
Malgorzata Celuch

Stephen Gedney
Mingyu Lu
Paolo Nepa
Rui Qiang

C. J. Reddy
Costas Sarris
Warren Stutzman
Alan Taflove

THE APPLIED COMPUTATIONAL ELECTROMAGNETICS SOCIETY
JOURNAL

Vol. 25 No. 1

January 2010

TABLE OF CONTENTS

“A Summary Review on 25 Years of Progress and Future Challenges in FDTD and FETD Techniques” F. L. Teixeira.....	1
“Integral Equation Methods for Near-Field Far-Field Transformation” C. H. Schmidt and T. F. Eibert.....	15
“FPGA Accelerated Phased Array Design Using the Ant Colony Optimization” O. Kilic.....	23
“A Simplified Model for Normal Mode Helical Antennas” C. Su, H. Ke, and T. Hubing.....	32
“Antenna Developments for Military Applications” A. I. Zaghoul, S. J. Weiss, and W. Coburn.....	41
“Low-profile, Broadband Polarization Converting Surface Ground Planes for Antenna Polarization Diversity” B. A. Lail and K. Y. Han.....	54
“A Numerical Study of Coaxial Helical Antennas” W. Coburn.....	61
“Analysis of Multi-Layer Composite Cavity Using FEKO” J. E. Stanley, D. H. Trout, S. K Earles, I. N. Kostanic, and P. F. Wahid.....	69
“Calibration and Evaluation of Body Interaction Effects for the Enhancement of a Body-Borne Radio Direction Finding System” A. Lalezari, F. Lalezari, and D. S. Filipović.....	75
“Application of the Normalized Surface Magnetic Source Model to a Blind Unexploded Ordnance Discrimination Test” F. Shubitidze, J. P. Fernández, I. Shamatava, L. R. Pasion, B. E. Barrows, and K. O’Neill...	85

A Summary Review on 25 Years of Progress and Future Challenges in FDTD and FETD Techniques

F. L. Teixeira

ElectroScience Laboratory and Department of Electrical and Computer Engineering
The Ohio State University
Columbus Ohio, 43210 USA
teixeira@ece.osu.edu

Abstract—The finite-difference time-domain (FDTD) method has established itself among the most popular methods for the numerical solution of Maxwell equations. Reasons for its popularity include its versatility, matrix-free characteristic, ease for parallelization, and low computational complexity. In recent years, the finite-element time-domain (FETD) has also become another very popular algorithm for solving time-domain Maxwell equations due to its geometrical flexibility and the steady growth in hardware computing power. In this review, we succinctly recollect some of the milestones in the development of FDTD and FETD over the last 25 years, and briefly discuss some challenges for the future development of these two algorithms.

Index terms— finite-difference time-domain, finite-element time-domain, Maxwell equations.

I. INTRODUCTION

In its basic form as introduced by Yee [1] and pioneered by Taflove [2], the finite-difference time-domain (FDTD) method is a conceptually very simple algorithm for solving Maxwell equations. FDTD basically relies on the approximation of the space-derivatives in the (Ampere's and Faraday's) first-order curl equations by central-differences on a staggered Cartesian (rectangular or hexahedral) grid and on a time-discretization following a "leap-frog" update. This leads to an algorithm that is second-order accurate in both space and time, i.e., which converges with the second power both on the spatial cell size Δs and the time-step size Δt . The conceptual simplicity of FDTD should not belittle

its power. Because FDTD is a matrix-free algorithm (i.e., it requires no linear algebra), its memory requirements scale only linearly with the number of unknowns. This, added to the fact that FDTD is massively parallelizable, makes it well suited for next-generation petascale machines and beyond.

Another popular algorithm for solving Maxwell equations is the finite-element time-domain (FETD) method. There are two basic popular approaches for constructing FETD methods for Maxwell equations. The first one is based on the discretization of the second-order vector Helmholtz wave equation for either the electric or magnetic field (after elimination of the other field) through an expansion of the unknown field in terms of vector basis functions [3], [4]. The second FETD approach is based on the discretization of the first-order coupled Maxwell curl equations (i.e., Faraday's and Ampere's laws) by expanding the electric and magnetic fields in terms of mixed elements—most often edge elements for the electric field and face elements for the magnetic flux density [5]. Because of their efficiency and versatility, FDTD and FETD have enjoyed widespread use by the computational electromagnetics (CEM) community.

Figure 1 purports to show the steady growth in the popularity of FDTD, as exemplified by the yearly number of papers in the 1986-2007 period obtained from a search under title/topic fields "finite-difference time-domain" or "FDTD" in the *ISI Web of Science*TM database, as of earlier 2009 (this plot is not intended to indicate the total number of FDTD-related papers, which is much higher).

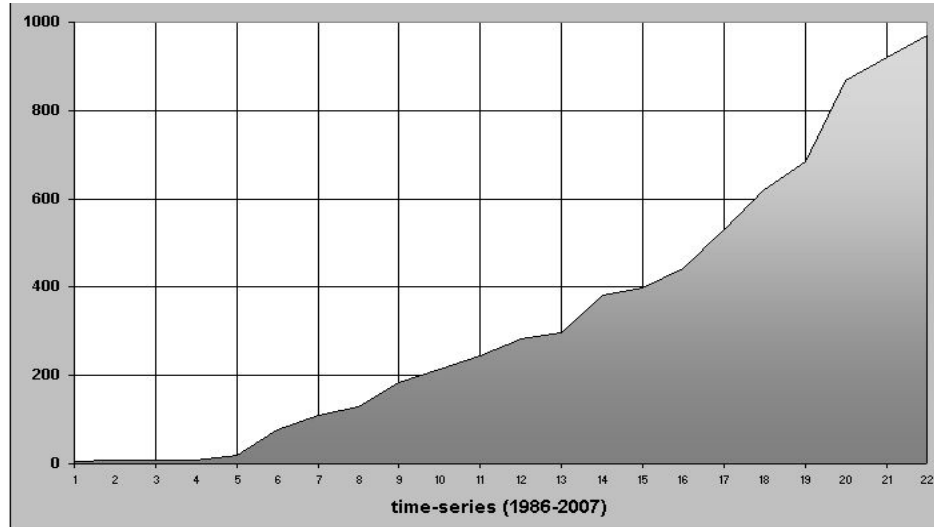


Fig. 1. Evolution on the popularity of FDTD exemplified by the yearly number of papers (1986-2007 period) obtained by a search under title/topic fields “finite-difference time-domain” or “FDTD” in the *ISI Web of Science™* database, as of earlier 2009.

In this summary review, we recollect some of milestones in the development and applications of FDTD and FETD for Maxwell’s equations during the last 25 years, and discuss some its future challenges. The list of references included here is relatively brief and by no means representative of the full extension of the volume of research efforts in this 25-year period.

A good source of references on FDTD is the book by Taflove and Hagness [2]. On FETD, a good reference source is the book by Jin [4]. A quite comprehensive list of catalogued references on FDTD in the period up to 1995 is available in [6]. A recent review on FDTD and FETD algorithms for complex (i.e., dispersive, anisotropic, inhomogeneous, nonlinear) media can be found in [7].

II. 25 YEARS OF PROGRESS IN FDTD: A BIRD’S EYE VIEW

Despite its introduction by Yee 18 years earlier (1966), FDTD was still a relatively incipient method 25 years ago (1984). This can be explained by the fact FDTD is a volumetric method and the computer memory resources for solving practical engineering problems were well beyond the reach of the average user at that time. The numerical method of choice in those years was the (frequency-domain) method of

moments. Early pioneers in FDTD algorithmic developments in the 1970s were Taflove [8], Holland [9], and Kunz [10] in the U.S. The acronym “FDTD” was actually not present in the 1966 Yee’s paper, and was coined by Taflove only in 1980 [11]. In Europe, Weiland independently developed a twin discretization methodology dubbed finite-integration-technique (FIT) [12]. The latter is based on the *integral* representation of Maxwell equations akin to a finite volume approach that, in a Cartesian grid, reduces to a set of equations identical to FDTD. We will not delve here into the FIT method and its extensions.

The early 1980s witnessed a surge in the development of absorbing boundary conditions (ABCs) for FDTD, including Mur and Liao ABCs that allowed for accurate simulations of open-space problems [13-16]. At that time, the first electromagnetic scattering FDTD models computing radar cross-section structures were developed [17,18]. The late 1980s were the period when FDTD applications to waveguides [19], microstrip circuits [20], and biological media [21] became feasible under (then) milder computational resources. This was facilitated not only by the continual growth of computational power, but also by concurrent algorithmic developments such as contour-path conformal modeling techniques [22-26] to reduce staircasing

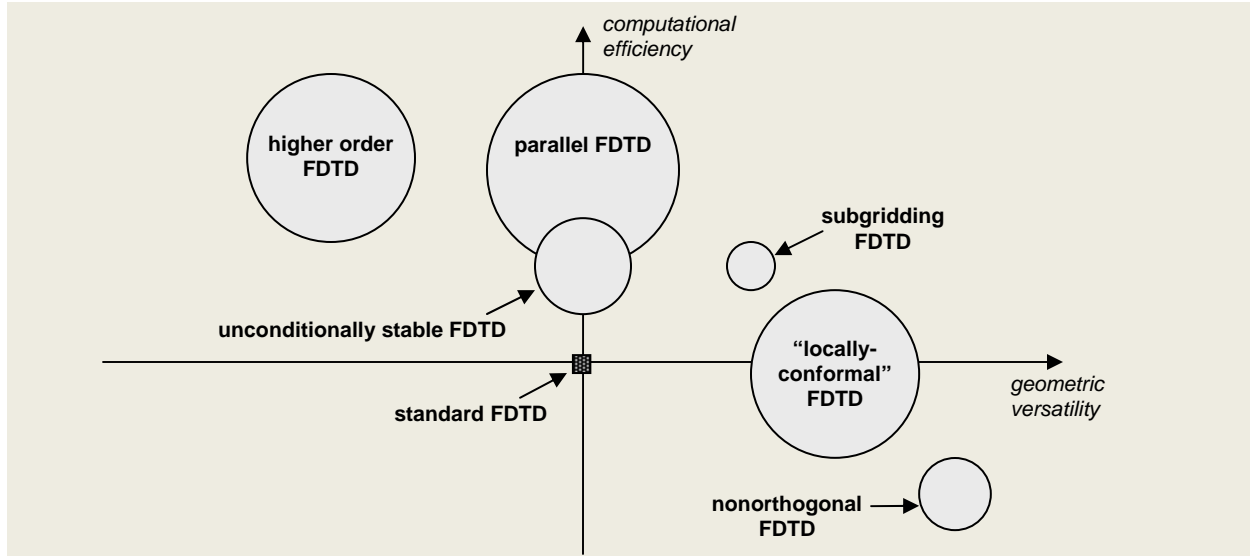


Fig. 2. Diagram illustrating various (non-inclusive) extensions of the “FDTD family” of methods developed towards improving geometrical versatility and/or computational efficiency of the standard FDTD. A negative correlation (trade-off) is apparent between these two objectives. The radii of the circles are approximately proportional to the number of entries for GoogleTM searches of each extension name in conjunction with the “FDTD” acronym. The radii serve as a rough indicator of the relative “historical popularity” of each approach.

error and increase geometrical flexibility, and by lumped equivalent circuit models to model sub-cell features and sources [27]. These techniques later played an important role in improving the suitability of commercial FDTD packages to RF, microwave, and antenna problems.

It was in the early 1990s that FDTD applications to the modeling of realistic circuits, antennas, and radiation problems [28-33] and of optical devices [34-36] began to appear very frequently in the literature. Also around that time, the extension of FDTD to frequency-dispersive media by means of recursive convolution approaches and later by auxiliary differential equation techniques [37, 38] provided further impetus for FDTD applications to complex media problems [7]. Also in the 1990s, new FDTD schemes were introduced for the efficient analysis of periodic structures [39-42].

With the increase of the electric size of the problems being tackled, the challenge of grid (numerical) dispersion error came to the forefront in the late 1980s and early 1990s. As a result, a series of high-order FDTD algorithms were developed to mitigate grid dispersion based on the use of a larger number of terms in the Fourier expansion to approximate the spatial

(and time) derivatives leading to enlarged finite-difference stencils [2]. This effort remains an area of active research interest to this day, with the development of ever more sophisticated higher order FDTD algorithms that include pre-asymptotic higher-order algorithms providing optimized (tailored) numerical dispersion curves in a particular frequency band and/or grid size [43,44]. Of note also is the development of pseudo-spectral time-domain (PSTD) methods with low dispersion error even for discretization scales near the Nyquist limit [45].

The introduction of the perfectly matched layer (PML) by Berenger in the mid 1990s [46-50] provided a major improvement on the dynamical range of open-domain FDTD simulations, which under mild computational costs could then reach 80 dB. It also allowed for the use of better use of FDTD in open domains with dispersive media such as in earth media [51].

The development of unconditionally stable algorithms for FDTD in the late 1990s and early years of the present decade— starting with alternating-direction-implicit (ADI) schemes [52,53] and later with split-step schemes such as the locally-one-dimensional (LOD) scheme [54]— represented another major milestone in the

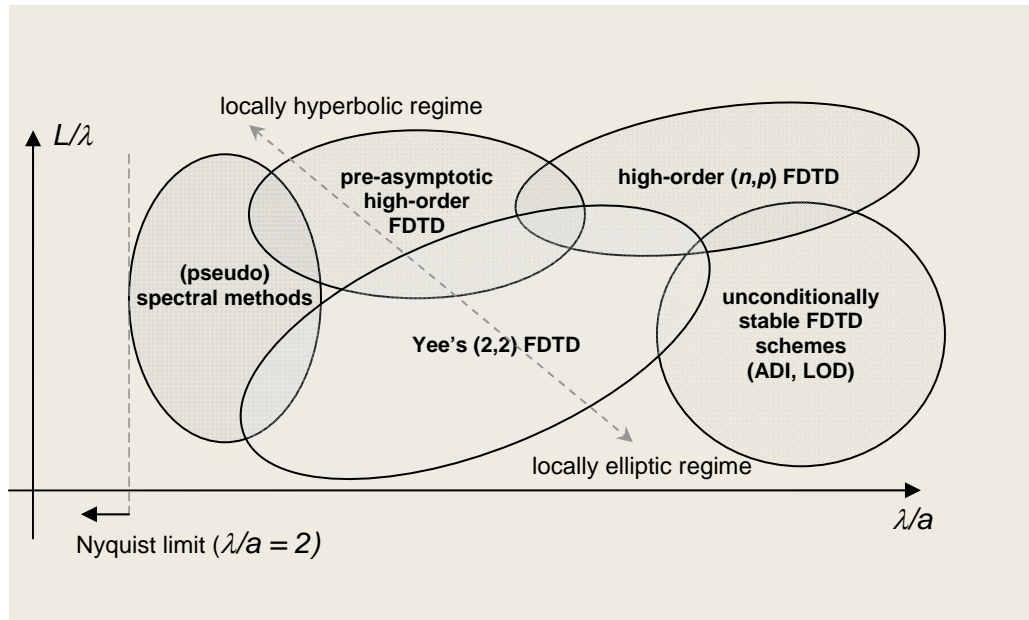


Fig. 3. Diagram illustrating the range of applicability of various FDTD-related algorithms vs. problem size and discretization scale. L denotes the domain size, λ is the central wavelength, and a is the spatial step (cell size). Indicative values are not provided as they would be implementation- and machine-dependent.

progress of FDTD because it lifted the Courant stability limit. Under these FDTD extensions, the time step is not bounded anymore by the stability criterion, but by accuracy considerations only. This has allowed the more efficient use of FDTD in problems that necessitate the use of highly refined grids (say, with an excess of 500 grid points per wavelength). The main challenges for unconditionally stable FDTD schemes are the introduction of new error mechanisms (more prominently, splitting errors) and the ever present numerical dispersion, which has different behavior than conventional FDTD [55].

Since the early days of FDTD applications, it was promptly recognized that one of its main limitations is the staircasing error [2]. In addition to contour-path conformal modeling techniques stated above, so-called “subgridding” techniques—a type of structured h -refinement whereby different grid cell sizes are used in different portions of the FDTD domain and connect through interfaces with hanging nodes—provide one possible approach to mitigate staircasing. Subgridding was first developed in the late 80’s with major impetus occurring in the 90’s [56-61]. Research continues to this day to develop stable subgridding algorithms that can provide low

spurious reflections at the fine-coarse grid interfaces and small aliasing error from the necessary interpolation/decimation operations [62-64]. *Nonorthogonal* FDTD algorithms—relying on the use covariant and contravariant field components in a non-orthogonal coordinate system—are also used introduced to mitigate staircasing. They were first introduced in the early 1980s, but early versions of nonorthogonal FDTD algorithms were prone to numerical instabilities due to subtle inconsistencies in the spatial discretization. Nonorthogonal FDTD algorithms with (conditional) stability were developed only in the late 1990s [65,66]. These developments for the most part still relied upon nonorthogonal, but still *structured* grids. The use of *unstructured* grids for FDTD is not as natural because the traditional derivation of finite-differences becomes somewhat contrived. In this case, FETD becomes a more natural choice for the spatial discretization. Figure 2 illustrated various extensions of the basic FDTD method toward improving its accuracy and/or geometrical flexibility. In general, there is a mild trade-off between these two objectives in FDTD, leading to the “negative correlation” illustrated in this Figure.

It should be pointed out FDTD is also quite suited for solving Maxwell equations in complex media with dispersive, anisotropic and/or nonlinear properties. A discussion on these extensions and applications is beyond the objectives of this paper, but a detailed review can be found in [7].

The late part of the present decade has witnessed a wide popularization of a number of user-friendly, commercial software that feature the FDTD as their main “solver engine”. Commercial PC-based codes have become pervasive in the RF, microwave, antenna, and optical communities and have also influenced the direction of research efforts. Furthermore, it has become apparent that certain research areas—such as device design—have become increasingly less reliant on “in-house” development of analysis (in particular numerical) tools. If this tendency continues, it is expected that this will lead to an increased “niching” of efforts by the CEM community and perhaps closer alignment with the computational physics and applied mathematics community, and perhaps less with the microwave and antenna engineering community at-large.

One important limitation present in commercial codes is related to the optimal choice in the “FDTD family” of depends on the nature and size of the problem, as illustrated in Figure 3. Commercial codes do not (yet) incorporate capabilities that would necessarily lead to the optimal choice of method for a given problem.

III. 25 YEARS OF PROGRESS IN FETD: A BIRD’S EYE VIEW

FETD is a relatively less mature than FDTD. As mentioned before, the main motivation for the development of FETD has been to increase the geometrical flexibility. This is because FETD is naturally based upon irregular (unstructured) grids, and thus capable of better adapting to curved or slanted geometries than a Cartesian FDTD. Compared to FDTD, the two major drawbacks for FETD are (1) the need for a pre-processing mesh generation step and (2) the need for a (sparse) linear solve at each time step.

The early FETD approaches for solving Maxwell equations were developed in the mid 1980s and were based on a point-matched

approach combined with nodal basis functions for each field component [3]. Although successfully for some problems especially in two-dimensions, this “nodal” approach was prone to spurious or ghost modes (also known as “spectral pollution”). This was a problem not restricted to FETD per se, but it is also present in other algorithms based on irregular grids, including the frequency-domain FE. For many years, the problem of spurious modes evaded a fundamental solution. Only *ad hoc* approaches such as inclusion of penalty terms seemed to work in suppressing spurious modes. It was only with the development of edge elements (also known as Whitney or curl-conforming elements) that the problem of spurious modes was finally overcome in FE (and FETD) [67].

Most often, the various extensions developed for the basic FETD algorithm mirror the progress observed in FDTD with a time lag of a few years. The application of PML absorbing boundary condition to FETD was first seen, for example, in the late 1990s and it is currently still under active development. Differently from FDTD, FETD naturally allows for a conformal PML implementation over curved grid boundaries [68-70], which permits a more compact (i.e., with less buffer space) grid, especially for scattering problems. Another approach to truncate the grid boundaries in FE has been to use FE-BI (boundary integral) formulations [4]. Due to difficulties caused by causality requirements and stability issues, FE-BI approaches are relatively less developed in the time-domain than in frequency-domain. Extensions of FETD to complex media were first developed in the 1990s and continue to this day, more recently pushed by technological advances in remote sensing and metamaterials, for example [7]. Similarly to FDTD, FETD is also prone to numerical dispersion error and higher-order versions of FETD do exist to combat this problem. However, the dispersion error in FETD irregular grids manifests itself in a *quasi-isotropic* fashion, as opposed to the *anisotropic* dispersion observed in the conventional (Cartesian) FDTD grid. This is because the irregular grid “averages out” the cumulative dispersion error along the various directions.

As stated, FETD methods provide more accurate geometric representation than FDTD. Moreover, FETD methods are much more amenable to high-order accuracy (*p*-refinement) in

general geometries by means of higher order basis functions, as opposed to enlarged stencils in FDTD. In particular, hierarchical higher order functions are particularly advantageous for p -adaptation because they can be implemented “in succession” and elements of different order can coexist in the same mesh [71,72]. Also, h - p adaptive refinement methods are more suited for FETD methods [73,74].

Since FETD requires sparse linear algebra, an important associated area of research is on efficient linear solvers for large sparse linear systems. FETD requires iterative solvers and good preconditioners for large problems. For smaller problems direct solution methods often suffice (and are typically preferred since they avoid convergence issues). The nature of the matrix

solvers in FETD depend on the particular time-discretization scheme being employed. Broadly speaking, time-discretization schemes utilized in FETD fall into two classes: The first class (I, sometimes referred to “implicit FETD” [4] although in a different sense from FDTD) necessitates the inversion of a system matrix that is a combination of stiffness and mass matrices, whereas the second class (II, sometimes referred to as “explicit FETD” [4] again in different sense from FDTD) necessitates the inversion of the mass matrix only [75]. The mass matrix is (when appropriately constructed) symmetric positive-definite, while the stiffness matrix is singular, hence linear systems resulting from class II are more benign. The ensuing trade-off is that Class II

Table 1: Comparison of some basic FDTD and FETD properties.

	FDTD	FETD
staircasing error	yes	no*
linear algebra	none	real and sparse
numerical dispersion	anisotropic	isotropic**
higher-order	larger stencils	p -refinement
mesh generation (pre-processing) step	absent	present**

(*)—linear facets (**)—for irregular grids

algorithms lead to conditionally stable algorithms, while Class I can produce unconditionally stable algorithms with no stability bound on the time-step.

As mentioned above, FETD algorithms have been traditionally based on the discretization of the second-order wave equation using edges elements for the electric *or* magnetic field, as opposed to using the two first-order Maxwell equations. The solution space of the former is larger compared to the latter, admitting (spurious) gradient fields with linear growth as solutions. Normally, if the initial conditions are properly set (divergence-free), these solutions are not excited. For long-time simulations however, numerical round-off error introduced by the linear solver can lead to the excitation of such modes. More recently, mixed FETD formulations directly based upon the first-order Maxwell curl equations have become increasingly popular [5,74-76]. In this case, two

different sets of basis functions are used (hence the name mixed), most often edge elements for the electric field and face elements for the magnetic field. This choice is informed by using the language of differential forms for Maxwell equations—as opposed to vector fields— where the electric field is a one-form and the magnetic flux density is a two-form [77]. This application of mixed basis functions satisfies a discrete version of the de Rham diagram, and thus it avoids spurious modes (see Section IV). Using a leap-frog scheme for the time-discretization, mixed E - B FETD produces conditionally stable algorithms with no secular growth modes [5]. Furthermore, under proper choice of edge and face basis function in a Cartesian grid and after mass lumping, the mixed E - B FETD recovers Yee’s FDTD (see Section IV). It also suggests a consistent way to extend Yee’s FDTD to slanted/curved interfaces and to construct hybrid FDTD/FETD algorithms.

IV. BRIDGING THE GAP BETWEEN FDTD AND FETD

Both FDTD and FETD are partial-differential-equation (PDE) based algorithms and—as considered here—applied to the same set of equations. Hence, it is only reasonable to expect, at some fundamental level, some major congruence between these two algorithms. Indeed, it can be shown that the FDTD is equivalent to (or it can be viewed as a special case of) FETD under the following choices for the FE discretization:

- i) *Regular* quadrilateral (2-D) or hexahedral (3-D) grid.
- ii) *Mixed basis functions* to expand the electric and magnetic fields (i.e., edge elements for \mathbf{E} and face elements for \mathbf{B}) along with Galerkin testing or construction of Galerkin Hodge operators [70,74-76],
- iii) *Mass lumping* applied to the mass matrix to approximate it as a diagonal matrix, and
- iv) *Leap-frog* update for the time discretization.

A key reference on mass lumping schemes for Maxwell equations is [78]. The geometric underpinning for all these choices in FETD becomes apparent when Maxwell's equations are cast in terms of exterior differential forms [67, 77]. In this representation, the electric field intensity vector \mathbf{E} is the proxy of a one-form E , whereas the magnetic flux density vector \mathbf{B} is the proxy of a two-form, B . More generally, p -forms are objects that can be associated at the discrete level with “ p -cells” of the mesh ($p=0$: nodes, $p=1$: edges, $p=2$: faces, $p=3$: volumes) and admit a natural discrete representation (cochains [79]) in terms of the so-called Whitney p -forms [67]. The latter recover edge elements for $p=1$ and face elements for $p=2$, for example. Moreover, the reason for staggered grids in FDTD is geometrically motivated by the fact that objects on the primal grid possess internal orientation (i.e., are “ordinary” differential forms) such as E and B , whereas objects on the dual grid possess external

orientation (i.e., they are “twisted” differential forms) such as H and D , see illustration in Fig. 4 (left) [77]. These two kinds of discrete differential forms are defined on two grids (cell complexes), each inheriting one type of orientation (primal and dual grid, or ordinary and twisted complex, see Fig. 4).

When using differential forms, all vector differential operators such as div , curl , and grad are unified and become reduced to different incarnations of the *exterior derivative operator* d [77,80]. The exterior derivative d admits a trivial implementation on an arbitrary mesh in terms of its adjoint: the *boundary operator* ∂ [80]. The boundary operator carries the intuitive meaning, i.e., it maps an edge into its (two) boundary nodes; it maps a face into its (three, in the case of a triangular or tetrahedral mesh, or four, in the case of a rectangular or hexahedral mesh) boundary edges; and so on, as illustrated in Fig. 4 (right) [77,80,81]. Note that $\partial^2=0$ is verified for any mesh element (i.e., the boundary of a boundary is zero). This identity is simply a generalization of the vector calculus identities $\text{div curl}=0$ and $\text{curl grad}=0$.

In relation with these identities, it should also be pointed out that any FDTD or FETD implementation should obey a discrete version of the so-called *de Rham diagram* [67,82], which is illustrated in Fig. 5. Essentially, the de Rham diagram implies that (in a simply connected domain) the space of discrete zero-curl fields is isomorphic (i.e., one-to-one) to the space of discrete gradient fields; the space of discrete zero-divergence fields is isomorphic to the space of discrete curl fields; and so on, mirroring the properties of the respective continuum spaces. Conformity to the de Rham diagram is a key property to avoid appearance of spurious modes during the discretization process [67,82]. In the conventional (Yee's) FDTD scheme, the de Rham diagram is trivially verified. However, this is not true for subgridded FDTD, contour-path FDTD, or hybrid FDTD/FETD implementations, for example. In those cases, care should be exercised to make sure the resulting formulation follows the discrete de Rham diagram.

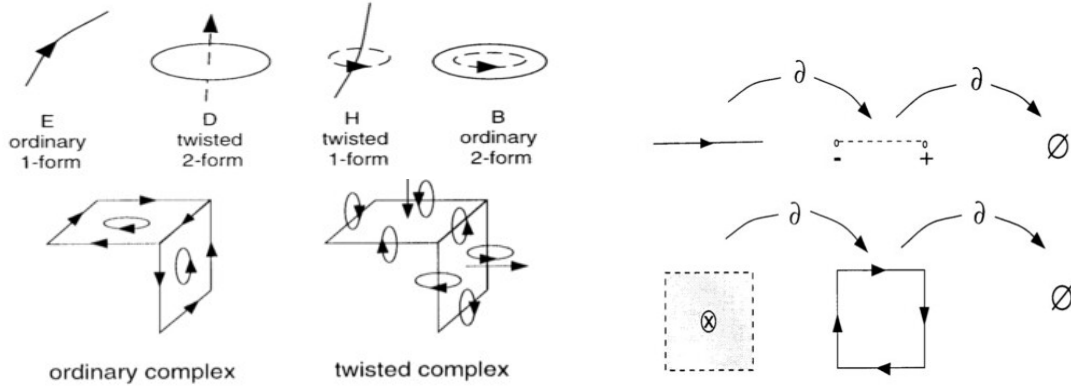


Fig. 4. *Left*—Internal (ordinary forms) and external (twisted forms) orientations for electromagnetic fields. This leads naturally to dual staggered grids (cell complexes). For simplicity, we depict a regular, hexahedral mesh. *Right*—Representation of the boundary operator ∂ acting on mesh elements (edge and cell/face). Note that the boundary of a boundary is always zero: $\partial^2=0$, which generalizes the identities $\text{curl grad}=0$, and $\text{div curl}=0$ distilled from their metric structure (Reprinted with permission from F. L. Teixeira and W. C. Chew, *J. Math. Phys.*, vol. 40, no. 1, pp. 169–187, 1999. © 1999, American Institute of Physics).

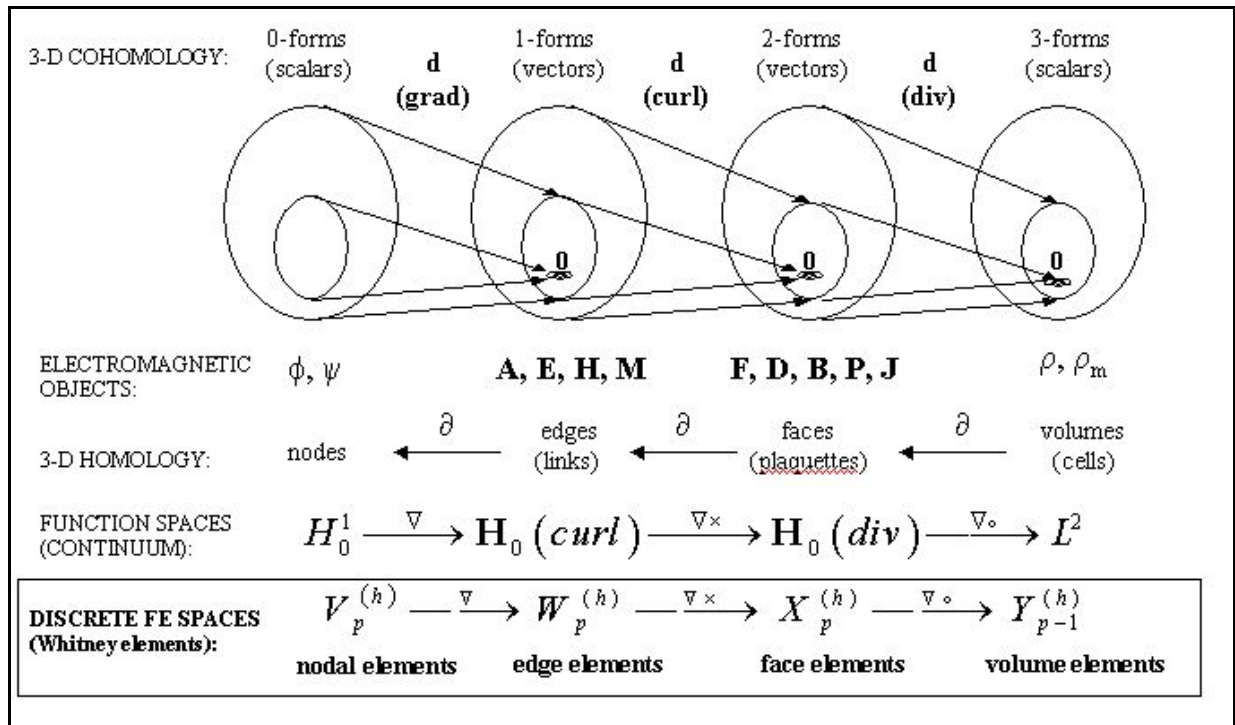


Fig. 5. Schematic illustration of the de Rham diagram (in a simply connected domain) and the relation among the various finite element spaces [67,82], differential forms [67,77], mesh components [80,81], and discrete operator maps [77]. The exterior derivative operator d (upper row) plays the role of the grad, curl, and div operators (fourth row) when acting on 0-, 1-, and 2-forms, respectively [77,81]. Both (consistent) FDTD and FETD algorithms should obey this diagram to avoid spurious modes.

V. FUTURE CHALLENGES

Prediction of future trends is always speculative and prone to miss “black swan” type of events. With this caveat in mind, we list below some of the future challenge areas for FDTD and FETD.

5.1 Parallelization and hardware developments—Since both FDTD and FETD algorithms are highly parallelizable, the full exploitation of parallel architectures and multicore processors with improved throughput and latency remains an important task. For FETD, linear solvers that explicitly exploit parallel architectures are likely to gain more importance. Coupled developments in FPGA and software-configurable microprocessors design are also likely to enhance the overall performance of FDTD and FETD codes. Of major importance also is the exploitation of graphics processing units (GPUs) and their highly parallel structure for acceleration of both FDTD and sparse linear solvers (the latter with obvious impact on FETD) [83].

5.2 Grid dispersion error control—For very large scale problems, minimization of grid-dispersion error is a critical issue. Ideally, this should be done with minimal impact on the underlying sparsity of the methods. In FDTD, pre-asymptotic high-order schemes have come a long way towards this objective, but similar progress remains to be achieved in FETD.

5.3 Adaptation—Further development in *a priori* and *a posteriori* error indicators in time-domain will certainly benefit the development of fully adaptive meshing techniques, either based on structured (for FDTD, such as subgridding techniques) or unstructured meshes for FETD, and using either static or dynamically adaptation [84].

5.4 Multi-domain approaches and domain-decomposition—Development of domain-decomposition (DD) techniques as a “divide-and-conquer” methodology to reduce the CPU requirements and most importantly, memory requirements in FETD, is another future challenge. Much progress has been done in recent years in frequency-domain DD-FE techniques, but application to the time-domain remains a challenge. In FDTD, the (possibly adaptive) use of

Huygens’ boxes to minimize the solution space remains an area for future developments especially for problems with highly disparate geometrical sizes, and for applications such as antenna-platform and antenna-antenna interaction problems [85].

5.5 Hybridization with integral-equation and asymptotic methods—The seamless integration (hybridization) of FETD and FETD with either full-wave TD-IE (integral equation) and/or high-frequency asymptotic approaches employing, for example, Gaussian beams or TD-UTD (uniform theory of diffraction), in dynamically adaptive schemes remains to be achieved.

5.6 Discrete differential forms—Application of differential forms is of particular interest to provide “design principles” of new FDTD and FETD compatible discretization schemes for more arbitrary mesh elements (polyhedral, concave) and in composite/heterogeneous grids [86].

5.7 Asynchronous time-stepping—Time-stepping is a relatively primitive and costly approach to enforce causality in time-domain methods. Possibly, the exploitation of discrete-event simulation approaches whereby dynamical states are updated asynchronously on demand (i.e., only when necessary) [87]—instead of synchronously—will certainly be an important development to extend the applicability of FDTD and FETD to, for example, problems with disparate time-scales (multiscale).

5.8 Hybrid FDTD/FETD—Since FETD provides better geometrical flexibility and FDTD better memory scalability, it is only natural to seek an hybridization of these two methods—using FETD in regions with high geometrical complexity and FDTD elsewhere [88]. Earlier hybrid FDTD/FETD schemes were often plagued by numerical instabilities and spurious modes [89]. Recently, consistent hybrid FDTD/FETD methods based on vector elements and free from instabilities were put forth [90]. These methods obey the consistency rules discussed in Section IV. It is expected that further development of hybrid FDTD/FETD, such as integration of higher order and extension to complex media, will make it a method of choice for many electromagnetic problems [91].

ACKNOWLEDGMENTS

Portions of this work were presented in the Special Session “25 Years of Progress and Future Challenges in Applied Computational Electromagnetics” organized by Prof. Branislav M. Notaros for the 25th International Review of Progress in Applied Computational Electromagnetics, held in Monterey, California in March 8-12, 2009. The author would like to thank Dr. Notaros for the invitation to contribute to this Special Session.

The author would also like to thank the four anonymous reviewers for their suggestions to improve this paper.

REFERENCES

- [1] K. S. Yee, “Numerical solution of initial boundary value problems involving Maxwell’s equations in isotropic media,” *IEEE Trans. Antennas Propag.*, vol. 14, pp. 302-307, 1966.
- [2] A. Taflove and S. Hagness, *Computational Electrodynamics: The Finite-Difference Time-Domain Method*, 3rd ed., Artech House, 2005.
- [3] J. F. Lee, R. Lee, and A. C. Cangellaris, “Time domain finite element methods,” *IEEE Trans. Antennas Propag.*, vol. 45, no. 3, pp. 430-442, 1997.
- [4] J. M. Jin, *The Finite Element Method in Electromagnetics*, 2nd ed., John Wiley, 2003.
- [5] B. Donderici and F. L. Teixeira, “Mixed finite-element time-domain method for transient Maxwell equations in doubly dispersive media,” *IEEE Trans. Microwave Theory Tech.*, vol. 56, no. 1, pp. 113-120, 2008.
- [6] K. L. Shlager and J. B. Schneider, “A selective survey of the finite-difference time-domain literature,” *IEEE Antennas Propag. Mag.*, vol. 37, no. 4, pp. 39-56, 1995.
- [7] F. L. Teixeira, “Time-domain finite-difference and finite-element methods for Maxwell equations in complex media,” *IEEE Trans. Antennas Propag.*, vol. 56, no. 8, pp. 2150-2166, 2008.
- [8] A. Taflove and M. E. Brodwin, “Numerical solution of steady-state electromagnetic scattering problems using the time-dependent Maxwell’s equations,” *IEEE Trans. Microwave Theory Tech.*, vol. 23, pp. 623-630, 1975.
- [9] R. Holland, “Threde: A free-field EMP coupling and scattering code,” *IEEE Trans. Nuclear Sci.*, vol. 24, pp. 2416-2421, 1977.
- [10] K. S. Kunz and K. M. Lee, “A three-dimensional finite-difference solution of the external response of an aircraft to a complex transient EM environment,” *IEEE Trans. Electromagn. Compat.*, vol. 20, pp. 328-341, 1978.
- [11] A. Taflove, “Application of the finite-difference time-domain method to sinusoidal steady state electromagnetic penetration problems,” *IEEE Trans. on Electromagn. Compat.*, vol. 22, pp. 191-202, 1980.
- [12] T. Weiland, “A discretization method for the solution of Maxwell’s equations for six-component fields,” *Electronics and Communications AEU*, vol. 31, no.3, pp. 116-120, 1977.
- [13] G. Mur, “Absorbing boundary conditions for the finite-difference approximation of the time-domain electromagnetic field equations,” *IEEE Trans. Electromagn. Compat.*, vol. 23, pp. 377-382., 1981.
- [14] Z. P. Liao, H. L. Wong, B. P. Yang, and Y. F. Yuan, “A transmitting boundary for transient wave analysis,” *Scientia Sinica A* vol. 27, pp. 1063-1076, 1984.
- [15] G. A. Kriegsmann, A. Taflove, and K. R. Umashankar, “A new formulation of electromagnetic wave scattering using an on-surface radiation boundary condition approach,” *IEEE Trans. Antennas Propag.*, vol. 35, pp. 153-161, 1987.
- [16] T. G. Moore, J. G. Blaschak, A. Taflove, and G. A. Kriegsmann, “Theory and application of radiation boundary operators,” *IEEE Trans. Antennas Propag.*, vol. 36, pp. 1797-1812, 1988.
- [17] K. R. Umashankar and A. Taflove, “A novel method to analyze electromagnetic scattering of complex objects,” *IEEE Trans. Electromagn. Compat.*, vol. 24, pp. 397-405, 1982.

- [18] A. Taflove and K. R. Umashankar, "Radar cross section of general three-dimensional scatterers," *IEEE Trans. Electromagn. Compat.*, vol. 25, pp. 433–440, 1983.
- [19] D. H. Choi and W. J. Hoefer, "The finite-difference time-domain method and its application to eigenvalue problems," *IEEE Trans. Microwave Theory Tech.*, vol. 34, pp. 1464–1470, 1986.
- [20] X. Zhang, J. Fang, K. K. Mei, and Y. Liu, "Calculation of the dispersive characteristics of microstrips by the time-domain finite-difference method," *IEEE Trans. Microwave Theory Tech.*, vol. 36, pp. 263–267, 1988.
- [21] D. M. Sullivan, O. P. Gandhi, and A. Taflove, "Use of the finite-difference time-domain method in calculating EM absorption in man models," *IEEE Trans. Biomed. Eng.*, vol. 35, pp. 179–186, 1988.
- [22] K. R. Umashankar, A. Taflove, and B. Beker, "Calculation and experimental validation of induced currents on coupled wires in an arbitrary shaped cavity," *IEEE Trans. Antennas Propag.*, vol. 35, pp. 1248–1257, 1987.
- [23] A. Taflove, K. R. Umashankar, B. Beker, F. A. Harfoush, and K. S. Yee, "Detailed FDTD analysis of electromagnetic fields penetrating narrow slots and lapped joints in thick conducting screens," *IEEE Trans. Antennas Propag.*, vol. 36, pp. 247–257, 1988.
- [24] C. J. Railton, I. J. Craddock, and J. B. Schneider, "An improved locally distorted CPFDTD algorithm with provable stability," *Electron. Lett.*, vol. 31, no. 18, pp. 1585–1586, 1995.
- [25] S. Dey and R. Mittra, "A locally conformal finite-difference time-domain (FDTD) algorithm for modeling three-dimensional perfectly conducting objects," *IEEE Microwave Guided Wave Lett.*, vol. 7, pp. 273–275, 1997.
- [26] C. J. Railton and J. B. Schneider, "An analytical and numerical analysis of several locally-conformal FDTD Schemes," *IEEE Trans. Microwave Theory Tech.*, vol. 47, no. 1, pp. 56–66, 1999.
- [27] W. Gwarek, "Analysis of an arbitrarily shaped planar circuit — A time-domain approach," *IEEE Trans. Microwave Theory Tech.*, vol. 33, pp. 1067–1072, 1985.
- [28] G. Maloney, G. S. Smith, and W. R. Scott, Jr., "Accurate computation of the radiation from simple antennas using the finite-difference time-domain method," *IEEE Trans. Antennas Propag.*, vol. 38, pp. 1059–1065, 1990.
- [29] D. S. Katz, A. Taflove, M. J. Piket-May, and K. R. Umashankar, "FDTD analysis of electromagnetic wave radiation from systems containing horn antennas," *IEEE Trans. Antennas Propag.*, vol. 39, pp. 1203–1212, 1991.
- [30] K. Li, C. F. Lee, S. Y. Poh, R. T. Shin, and J. A. Kong, "Application of FDTD method to analysis of electromagnetic radiation from VLSI heatsink configurations," *IEEE Trans. Electromagn. Compat.*, vol. 35, no. 2, pp. 204–214, 1993.
- [31] R. Lee and T.T. Chia, "Analysis of electromagnetic scattering from a cavity with a complex termination by means of a hybrid ray-FDTD method," *IEEE Trans. Antennas Propag.*, vol. 41, pp. 1560–1569, 1993.
- [32] V. A. Thomas, M. E. Jones, M. J. Piket-May, A. Taflove, and E. Harrigan, "The use of SPICE lumped circuits as sub-grid models for FDTD high-speed electronic circuit design," *IEEE Microwave Guided Wave Lett.*, vol. 4, pp. 141–143, 1994.
- [33] A. Bataineh, R. Lee, and F. Ozguner, "Electrical characterization of high-speed interconnects with a parallel three-dimensional finite difference time-domain algorithm," *Simulation*, vol. 64, pp. 289–295, 1995.
- [34] E. Sano and T. Shibata, "Full-wave analysis of picosecond photoconductive switches," *IEEE J. Quantum Electron.*, vol. 26, pp. 372–377, 1990.
- [35] P. M. Gortjian and A. Taflove, "Direct time integration of Maxwell's equations in nonlinear dispersive media for propagation and scattering of femtosecond electromagnetic solitons," *Opt. Lett.*, vol. 17, pp. 180–182, 1992.
- [36] R. W. Ziolkowski and J. B. Judkins, "Full-wave vector Maxwell's equations modeling

- of self-focusing of ultra-short optical pulses in a nonlinear Kerr medium exhibiting a finite response time," *J. Opt. Soc. Am. B*, vol. 10, pp. 186–198, 1983.
- [37] R. Luebbers, F. Hunsberger, K. Kunz, R. Standler, and M. Schneider, "A frequency-dependent finite-difference time-domain formulation for dispersive materials," *IEEE Trans. Electromagn. Compat.*, vol. 32, pp. 222–227, 1990.
- [38] R. M. Joseph, S. C. Hagness, and A. Taflove, "Direct time integration of Maxwell's equations in linear dispersive media with absorption for scattering and propagation of femtosecond electromagnetic pulses," *Opt. Lett.*, vol. 16, pp. 1412–1414, 1991.
- [39] A. C. Cangellaris, M. Gribbons, and G. Sohos, "A hybrid spectral/FDTD method for the electromagnetic analysis of guided waves in periodic structures," *IEEE Microwave Guided Wave Lett.*, vol. 3, no. 10, pp. 375–377, 1993.
- [40] P. Harms, R. Mittra, and W. Ko, "Implementation of the periodic boundary condition in the finite-difference time-domain algorithm for FSS structures," *IEEE Trans. Antennas Propag.*, vol. 42, no. 9, pp. 1317–1324, 1994.
- [41] A. Taflove and S. Hagness, "Analysis of Periodic Structures," in *Computational Electrodynamics: The Finite Difference Time Domain Method*. Boston, MA: Artech House, 1995, ch. 13.
- [42] M. Celuch-Marcysiak and W. K. Gwarek, "Spatially looped algorithms for time-domain analysis of periodic structures," *IEEE Trans. Microwave Theory Tech.*, vol. 43, no. 4, pp. 860–865, 1995.
- [43] S. Wang and F. L. Teixeira, "Dispersion-relation-preserving FDTD schemes of large-scale three-dimensional problems," *IEEE Trans. Antennas Propag.*, vol. 51, no. 8, pp. 1818–1828, 2003.
- [44] B. Finkelstein and R. Kastner, "A comprehensive new methodology for formulating FDTD schemes with controlled order of accuracy and dispersion," *IEEE Trans. Antennas Propag.*, vol. 56, no. 11, pp. 3516–3525, 2008.
- [45] Q.H. Liu, "The PSTD algorithm: A time-domain method requiring only two cells per wavelength," *Microwave Opt. Technol. Lett.*, vol. 15, no. 3, pp. 357–361, 1997.
- [46] J. Berenger, "A perfectly matched layer for the absorption of electromagnetic waves," *J. Comput. Phys.*, vol. 114, pp. 185–200, 1994.
- [47] D. S. Katz, E. T. Thiele, and A. Taflove, "Validation and extension to three dimensions of the Berenger PML absorbing boundary condition for FDTD meshes," *IEEE Microwave Guided Wave Lett.*, vol. 4, pp. 268–270, 1994.
- [48] Z. S. Sacks, D. M. Kingsland, R. Lee, and J. F. Lee, "A perfectly matched anisotropic absorber for use as an absorbing boundary condition," *IEEE Trans. Antennas Propag.*, vol. 43, pp. 1460–1463, 1995.
- [49] F. L. Teixeira and W. C. Chew, "Complex space approach to perfectly matched layers: A review and some new developments," *Int. J. Num. Model.*, vol. 13, no. 5, pp. 441–455, 2000.
- [50] F. L. Teixeira, K. P. Hwang, W. C. Chew, and J. M. Jin, "Conformal PML-FDTD schemes for electromagnetic field simulations: A dynamic stability study," *IEEE Trans. Antennas Propag.*, vol. 49, no. 6, pp. 902–907, 2001.
- [51] C. D. Moss, F. L. Teixeira, Y.E. Yang, and J. A. Kong, "Finite-difference time-domain simulation of scattering from objects in continuous random media," *IEEE Trans. Geosci. Remote Sens.*, vol. 40, no. 1, pp. 178–186, 2002.
- [52] T. Namiki, "A new FDTD algorithm based on alternating-direction implicit method," *IEEE Trans. Microwave Theory Tech.*, vol. 47, no. 10, pp. 2003–2007, Oct. 1999.
- [53] F. Zheng, Z. Chen, and J. Zhang, "Toward the development of a three-dimensional unconditionally stable finite-difference time-domain method," *IEEE Trans. Microw. Theory Tech.*, vol. 48, no. 9, pp. 1550–1558, Sep. 2000.
- [54] V. E. do Nascimento, B.-H. V. Borges, and F. L. Teixeira, "Split-field PML implementations for the unconditionally stable LOD-FDTD method," *IEEE*

- Microwave Wireless Components Lett.*, vol. 16, no. 7, pp. 398-400, 2006.
- [55] K.-Y. Jung and F. L. Teixeira, "An iterative unconditionally stable LOD-FDTD method," *IEEE Microwave Wireless Components Lett.*, vol. 18, no. 2, pp. 76-78, 2008.
- [56] S. S. Zivanovic, K. S. Yee, and K. K. Mei, "A subgridding method for the time-domain finite-difference method to solve Maxwell's equations," *IEEE Trans. Microwave Theory Tech.*, vol. 39, no. 3, pp. 471-479, 1991.
- [57] S. Kapoor, "Sub-cellular technique for finite-difference time-domain method," *IEEE Trans. Microwave Theory Tech.*, vol. 45, no. 5, pp. 673-677, 1997.
- [58] M. Okoniewski, E. Okoniewska, and M. A. Stuchly, "Three-dimensional subgridding algorithm for FDTD," *IEEE Trans. Antennas Propag.*, vol. 45, no. 3, pp. 422-429, 1997.
- [59] K. M. Krishnaiah and C. J. Railton, "Passive equivalent circuit of FDTD: an application to subgridding," *Electron. Lett.*, vol. 33, pp. 1277-1278, 1997.
- [60] P. Thoma and T. Weiland, "A consistent subgridding scheme for the finite difference time domain method," *Int. J. Num. Model.* **9**, 359-374, 1996.
- [61] K. M. Krishnaiah and C. J. Railton, "A stable subgridding algorithm and its application to eigenvalue problems," *IEEE Trans. Microwave Theory Tech.*, vol. 47, pp. 620-628, 1999.
- [62] S. Wang, F. L. Teixeira, R. Lee, and J.-F. Lee, 'Optimization of subgridding schemes for FDTD,' *IEEE Microwave Wireless Components Lett.*, vol. 12, no. 6, pp. 223-225, 2002.
- [63] B. Donderici and F. L. Teixeira, "Improved FDTD subgridding algorithms via digital filtering and domain overriding," *IEEE Trans. Antennas Propag.*, vol. 53, no. 9, pp. 2938-2951, 2005.
- [64] J. P. Berenger, "A Huygens subgridding for the FDTD method," *IEEE Trans. Antennas Propag.*, vol. 54, no. 12, pp. 3797 - 3804, 2006.
- [65] R. Schuhmann and T. Weiland, "A stable interpolation technique for FDTD on non-orthogonal grids," *Int. J. Num. Model.*, vol. 11, no. 6, pp. 299 - 306, 1999.
- [66] S. D. Gedney and J. A. Roden, "Numerical stability of nonorthogonal FDTD methods," *IEEE Trans. Antennas Propag.*, vol. 48, issue 2, pp. 231-239, 2000.
- [67] A. Bossavit, "Whitney forms: A new class of finite elements for three-dimensional computations in electromagnetics," *IEE Proc. A*, vol. 135, pp. 493-500, 1988.
- [68] F. L. Teixeira and W. C. Chew, "Analytical derivation of a conformal perfectly matched absorber for electromagnetic waves," *Microwave and Optical Technology Letters*, vol. 17, no. 4, pp. 231-236, 1998.
- [69] T. Rylander and J.-M. Jin, "Conformal perfectly matched layers for the time domain finite element method," in *IEEE AP-S Int. Symp. Digest*, vol. 1, pp. 698-701, 2003.
- [70] B. Donderici and F. L. Teixeira, "Conformal perfectly matched layer for the mixed finite-element time-domain method," *IEEE Trans. Antennas Propag.*, vol. 56, no. 4, pp. 1017-1026, 2008.
- [71] M. M. Ilic and B. M. Notaros, "Higher order hierarchical curved hexahedral vector finite elements for electromagnetic modeling," *IEEE Trans. Microwave Theory Tech.*, vol. 51, no. 3, pp. 1026-103, 2003.
- [72] R. N. Rieben, G. H. Rodrigue, and D. A. White, "A high order mixed vector finite element method for solving the time dependent Maxwell equations on unstructured grids," *J. Comp. Phys.*, vol. 204, no. 2, pp. 490-519, 2005.
- [73] G. Cohen, *Higher Order Numerical Methods for Transient Wave Equations*, Springer-Verlag, 2001.
- [74] N. Marais and D. B. Davidson, "Numerical evaluation of high-order finite element time domain formulations in electromagnetics," *IEEE Trans. Antennas Propag.*, vol. 56, no. 12, pp. 3743-3751, 2008.
- [75] B. He and F. L. Teixeira, "A sparse and explicit FETD via approximate inverse Hodge (mass) matrix," *IEEE Microwave Wireless Components Lett.*, vol. 16, no. 6, pp. 348-350, 2006.
- [76] M. Wong, O. Picon, and V. F. Hanna, "A finite element method based on Whitney

- forms to solve Maxwell equations in the time domain,” *IEEE Trans. Magn.*, vol. 31, no. 3, pp. 1618–1621, 1995.
- [77] F. L. Teixeira and W. C. Chew, “Lattice electromagnetic theory from a topological viewpoint,” *J. Math. Phys.*, vol. 40, no. 1, pp. 169–187, 1999.
- [78] G. Cohen and P. Monk, “Gauss point mass lumping schemes for Maxwell’s equations,” *Numer. Meth. Partial Diff. Eq.*, vol. 14, pp. 63–88, 1998.
- [79] J. R. Munkres, *Elements of Algebraic Topology*, Addison-Wesley, Reading, Mass., 1984.
- [80] F. L. Teixeira (ed.), *Geometrical Methods for Computational Electromagnetics*, Progress In Electromagnetics Research Series 32, EMW Publishing, Cambridge, Mass., 2001.
- [81] B. He and F. L. Teixeira, “On the degrees of freedom of lattice electrodynamics,” *Phys. Lett. A*, vol. 336, pp. 1–7, 2005.
- [82] P. Monk, *Finite Element Methods for Maxwell's Equations*, Oxford Univ. Press, 2003.
- [83] S. Adams, J. Payne, and R. Boppana, “Finite Difference Time Domain (FDTD) Simulations Using Graphics Processors,” *Proc. 2007 DoD High Performance Computing Modernization Program Users Group Conf.*, pp. 334–338, 2007.
- [84] Y. Liu and C.D. Sarris, “Fast Time-Domain Simulation of Optical Waveguide Structures with a Multilevel Dynamically Adaptive Mesh Refinement FDTD Approach,” *J. Lightwave Technol.*, vol. 24, no. 8, pp. 3235–3247, 2006.
- [85] R. A. Abd-Alhameed and P. S. Excell, “Complex computational electromagnetic using hybridization techniques,” in *Advances in Information Technologies for Electromagnetics* (L. Tarricone, A. Esposito, eds.), Springer-Verlag, pp.69–145, 2006.
- [86] B. Donderici and F. L. Teixeira, “Accurate interfacing of heterogeneous structured FDTD grid components,” *IEEE Trans. Antennas Propag.*, vol. 54, no. 6, pp. 1826–1835, 2006.
- [87] A. Lew, A., J.E. Mardsen, M. Ortiz, and M. West, “Asynchronous variational integrators,” *Arch. Rational Mech. Anal.*, vol. 167, p. 85, 2003.
- [88] D. J. Riley and C. D. Turner, “VOLMAX: a solid-model-based, transient volumetric Maxwell solver using hybrid grids,” *IEEE Antennas Propag. Mag.*, vol. 39, no. 1, pp. 20–33, 1997.
- [89] C.-T. Hwang and R.-B. Wu, “Treating late-time instability of hybrid finite-element/finite-difference time-domain method,” *IEEE Trans. Antennas Propag.*, vol. 47, no. 2, pp. 227–232, 1999.
- [90] T. Rylander and A. Bondeson, “Stable FDTD-FEM hybrid method for Maxwell’s equations,” *Comp. Phys. Comm.*, vol. 125, pp. 75–82, 2000.
- [91] J. Jin and D. J. Riley, *Finite Element Analysis of Antennas and Arrays*, Wiley-IEEE Press, 2009.

Integral Equation Methods for Near-Field Far-Field Transformation

Carsten H. Schmidt and Thomas F. Eibert

Lehrstuhl für Hochfrequenztechnik, Technische Universität München,
80290 München, Germany
carstenschmidt@tum.de, eibert@tum.de

Abstract— Antenna measurements are often carried out in the radiating near-field of the antenna under test. Near-field transformation algorithms determine an equivalent sources representation of the antenna in an inverse process and field values in almost arbitrary distances can be computed. In this paper two integral equation methods for the near-field transformation are presented, which are especially suitable for electrically large antennas, irregular sample point distributions, higher order probes, and non-ideal measurement environments.

Index Terms— Integral Equation Methods, Near-Field Far-Field Transformation, Plane Wave Expansion, Equivalent Current Methods.

I. INTRODUCTION

The radiation characteristic of an antenna under test (AUT) can be determined employing one of the various measurement techniques, e.g. far-field, compact range or near-field measurements [1]. For electrically large antennas, which achieve far-field conditions in a distance of several tens or even hundreds of meters, indoor far-field measurements are not applicable due to the limited size of the measurement facility. In open field test ranges the environmental conditions are difficult to control for precise measurements. In near-field measurement techniques the radiated field distribution of the AUT is measured in the radiating near-field and afterwards processed into the far-field or even other observation locations, typically outside the AUT minimum sphere as illustrated in Fig. 1. With the computational resources available nowadays, near-field transformation algorithms allow to compute the far-field pattern of the AUT with

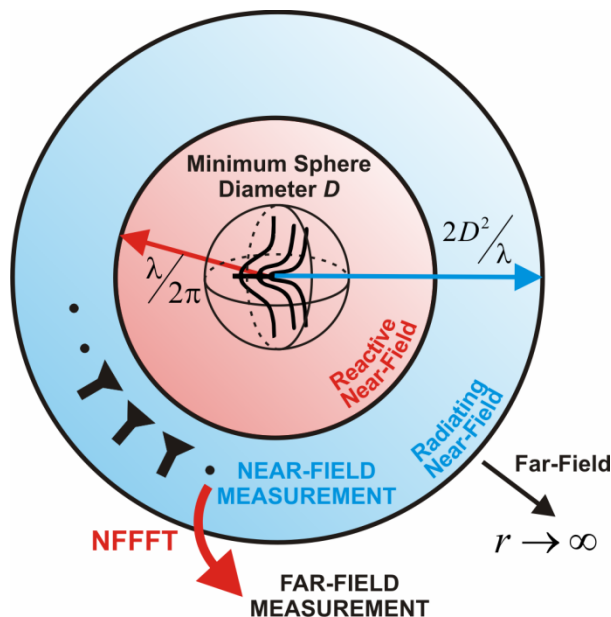


Fig. 1. Antenna field regions and measurement setup.

accuracies comparable to a direct far-field measurement.

In the transformation algorithm, the radiated field distribution of the AUT is represented by equivalent sources and their unknown amplitudes are determined in an inverse process from the measured near-field values.

In practice a near-field probe with finite geometrical extent and a corresponding receiving characteristic is used to probe the AUT field distribution. For a measurement of the electric field strength at a discrete sampling point, the probe kind of integrates the field over its volume resulting in an output signal proportional to the weighted field distribution around the sampling location (see Fig. 2). To compensate this effect, a probe correction is

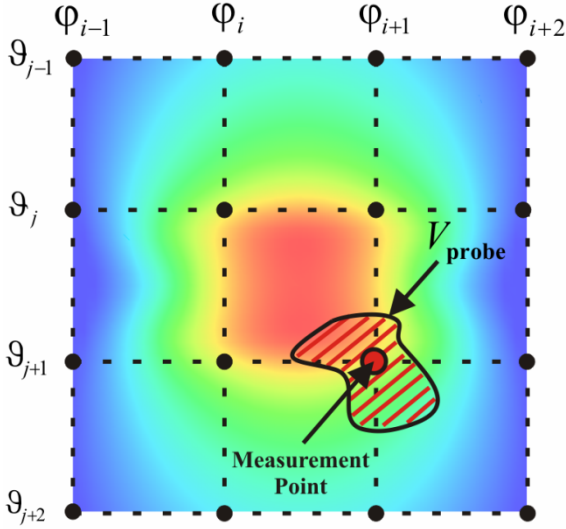


Fig. 2. Probe weighting effect in electric near-field measurement.

employed in most of the transformation algorithms [2].

Depending on the kind of measurement, various near-field transformation algorithms exist, all with their own benefits and drawbacks.

One of the major categories are algorithms working with eigenmode expansions of the AUT fields [3], for example spherical, cylindrical, and plane waves for spherical [4], cylindrical, and planar measurement surfaces [5], respectively.

To relate the amplitudes of the waves to the measured near-field values in an efficient manner, the orthogonality of the eigenmodes is utilized. This requires an often regular measurement grid

on the corresponding coordinate surfaces, even though some techniques have been proposed for spherical [6] and planar [7] near-field measurements with non-ideal probe locations.

The computational complexity of the probe correction strongly depends on the measurement geometry. While general probes can be corrected efficiently for planar near-field measurements [5], a full correction of higher order probes for spherical near-field measurements becomes time consuming since either the measurement or the transformation time [8] is increased. Nevertheless efficient formulas for so-called first order probes with an azimuthal mode spectrum restricted to the $\mu=\pm 1$ modes are well-known [4].

A second category of near-field transformation algorithms works with integral equation evaluations. Equivalent current methods (ECM) [9-12] assume equivalent Huygens currents either on a fictitious surface (green sphere in Fig. 3 left) or the radiating structure itself (red arrows on horn antenna surface mesh Fig. 3 left). The currents are related to the field values employing a field integral equation. For an efficient solution, this equation can be evaluated using fast solver techniques like the multilevel fast multipole method (MLFMM) [13-14]. As such, a plane wave expansion is employed to convert the equivalent Huygens currents into propagating plane waves (Fig. 3 middle), which can be translated to the field probe position efficiently.

A full probe correction is achieved by weighting the incident plane waves with the probe's far-field pattern prior to superposition (Fig. 3 right)

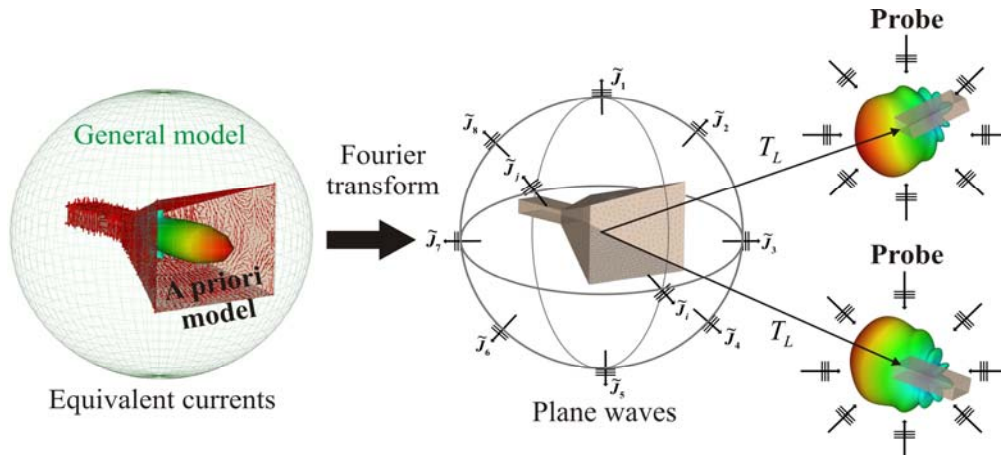


Fig. 3. Equivalent current and plane wave representation of AUT.

without increasing the algorithms complexity. A second approach, referred to as plane wave based near-field far-field transformation (PWNFFFT), utilizes the plane waves as equivalent sources directly [15]. Due to the integral equation formulation, both approaches are well suited for irregular measurement surfaces. The fast solver techniques with a low complexity also allow the transformation of electrically large antennas.

In the following sections, the ECM and PWNFFFT approaches are discussed and some results are shown. Further, some remarks on electrically large antennas and non-ideal measurement environments are given.

II. EQUIVALENT CURRENT METHOD

According to Huygens' principal, the electric field strength

$$\mathbf{E}(\mathbf{r}_M) = \iint_A \left[\bar{\mathbf{G}}_J^E(\mathbf{r}_M, \mathbf{r}') \cdot \mathbf{J}_A(\mathbf{r}') + \bar{\mathbf{G}}_M^E(\mathbf{r}_M, \mathbf{r}') \cdot \mathbf{M}_A(\mathbf{r}') \right] dA' + \mathbf{E}^{\text{inc}}(\mathbf{r}_M) \quad (1)$$

due to a radiating or scattering object at a measurement point \mathbf{r}_M can be computed from the electric and magnetic Huygens currents $\mathbf{J}_A(\mathbf{r}')$ and $\mathbf{M}_A(\mathbf{r}')$ assumed on the surface A , either a fictitious surface or the radiating/scattering structure itself. $\bar{\mathbf{G}}_J^E(\mathbf{r}_M, \mathbf{r}')$ and $\bar{\mathbf{G}}_M^E(\mathbf{r}_M, \mathbf{r}')$ are the dyadic Green's functions of free space and $\mathbf{E}^{\text{inc}}(\mathbf{r}_M)$ is the incident field used as excitation for scattering investigations. In the following, the paper focuses on antenna measurements, where no incident electric field $\mathbf{E}^{\text{inc}}(\mathbf{r}_M)$ is present. The ECM relating the equivalent Huygens currents to the measured probe signals is developed in the following. The formulation starts with the output signal

$$\mathbf{U}(\mathbf{r}_M) = \iiint_{V_{\text{probe}}} \mathbf{w}_{\text{probe}}(\mathbf{r}) \cdot \mathbf{E}(\mathbf{r}) dV \quad (2)$$

of the field probe measuring the radiated near-field distribution. It is obtained by weighting the electric field over the probe volume according to the spatial probe characteristic $\mathbf{w}_{\text{probe}}(\mathbf{r})$ as seen in Fig. 2.

The electric and magnetic surface currents characterizing the AUT are discretized on a triangular surface mesh [12] utilizing Rao-Wilton-

Glisson (RWG) basis functions $\boldsymbol{\beta}(\mathbf{r})$ [16] resulting in

$$\mathbf{U}(\mathbf{r}_M) = \iiint_{V_{\text{probe}}} \mathbf{w}_{\text{probe}}(\mathbf{r}) \cdot \left[\sum_p J_p \iint_A \bar{\mathbf{G}}_J^E(\mathbf{r}_M, \mathbf{r}') \cdot \boldsymbol{\beta}_p(\mathbf{r}') dA' + \sum_q M_q \iint_A \bar{\mathbf{G}}_M^E(\mathbf{r}_M, \mathbf{r}') \cdot \boldsymbol{\beta}_q(\mathbf{r}') dA' \right] dV. \quad (3)$$

J_p and M_q are the unknown current expansion coefficients. Applying Gegenbauer's addition theorem together with a plane wave expansion, the spatial integral for the probe signal can be cast in a spectral integral

$$\mathbf{U}(\mathbf{r}_M) = -j \frac{\omega \mu}{4\pi} \left[\sum_p J_p \oint T_L(\hat{k}, \hat{r}_M) \mathbf{P}(\hat{k}, \mathbf{r}_M) \cdot (\bar{\mathbf{I}} - \hat{k}\hat{k}) \cdot \tilde{\boldsymbol{\beta}}_p(\hat{k}) d\hat{k}^2 + \sum_q M_q \iint T_L(\hat{k}, \hat{r}_M) \mathbf{P}(\hat{k}, \mathbf{r}_M) \cdot \frac{1}{Z} (\tilde{\boldsymbol{\beta}}_q(\hat{k}) \times \hat{k}) d\hat{k}^2 \right] \quad (4)$$

over the Ewald sphere analog to the fast multipole method (FMM) [13-14]. The spatial basis functions $\boldsymbol{\beta}(\mathbf{r})$ are Fourier transformed into their spectral counterparts $\tilde{\boldsymbol{\beta}}(\hat{k})$, i.e. the corresponding plane wave representation. The spatial probe weighting function $\mathbf{w}_{\text{probe}}(\mathbf{r})$ is Fourier transformed as well into the spectral probe correction coefficient $\mathbf{P}(\hat{k}, \mathbf{r}_M)$. This is simply the product of the probe's far-field pattern and the antenna factor, relating the electric field to the probe signal. The plane waves are translated from the AUT to the field probe position \mathbf{r}_M by multiplication with the diagonal translation operator $T_L(\hat{k}, \hat{r}_M)$. Then, they are weighted with the probe correction coefficient and superimposed to give the measured probe signal. The diagonal form of the translation operator is a key factor for the realization of a fast integral equation solver. The FMM acceleration is implemented in a multilevel fashion (MLFMM) similar to [17] and further described in section VI.

To determine the unknown current expansion coefficients in an inverse process, the probe output signal is measured at several points. Electrically large AUTs require a huge number of unknowns in

order to model the radiation behavior accurately and a large number of measurement points is also required for the inverse solution. Due to the high complexity of direct solvers, the resulting normal system of equations is solved by the iterative generalized minimum residual method (GMRES) [18].

In addition to far-field computations, ECMs are also suitable for antenna diagnostics, especially if a priori knowledge is given. Therefore, the equivalent currents on the radiating structure can be directly evaluated in order to inspect the antenna's functioning. It is further noted that ECMs are suitable for near-field measurements close to the AUT, when modal expansion methods might no longer be applicable.

Key features of the presented ECM include:

- Antenna diagnostics possible
- Near-field measurements close to AUT possible

III. PLANE WAVE BASED NEAR-FIELD TRANSFORMATION

The second approach (PWNFFFT) utilizes directly plane waves as equivalent sources representing the AUT. The spectral plane wave representation of the AUT is obtained from the electric equivalent Huygens currents by Fourier transform according to

$$\tilde{\mathbf{J}}_A(\hat{k}) = \iiint_{V_{AUT}} \mathbf{J}_A(\mathbf{r}') e^{j\hat{k} \cdot \mathbf{r}'} dV' \quad (5)$$

without any prior discretization. The same is done for the magnetic currents. The output signal of the field probe is thus obtained from Eq. (4) as

$$\mathbf{U}(\mathbf{r}_M) = -j \frac{\omega\mu}{4\pi} \left[\iint T_L(\hat{k}, \hat{r}_M) \mathbf{P}(\hat{k}, \mathbf{r}_M) \cdot (\bar{\mathbf{I}} - \hat{k}\hat{k}) \cdot \tilde{\mathbf{J}}(\hat{k}) d\hat{k}^2 \right] \quad (6)$$

Plane waves representing electric and magnetic currents are combined to the total plane wave spectrum

$$(\bar{\mathbf{I}} - \hat{k}\hat{k}) \cdot \tilde{\mathbf{J}}(\hat{k}) = (\bar{\mathbf{I}} - \hat{k}\hat{k}) \cdot \tilde{\mathbf{J}}_A(\hat{k}) + \frac{1}{Z} (\tilde{\mathbf{M}}_A(\hat{k}) \times \hat{k}) \quad (7)$$

for convenience. The further steps, translation and

probe correction as well as the entire solution process are similar to the ECM. The plane waves used as equivalent sources are proportional to the desired far-field pattern of the AUT. Therefore, an additional far-field computation from the determined sources is no longer required.

Key features of the presented PWNFFFT include:

- Minimum number of unknowns possible
- No separate far-field computation

IV. NEAR-FIELD TRANSFORMATION ALGORITHM

The utilization of the presented methods for near-field measurements is addressed in this section and shown in the flowchart in Fig. 4.

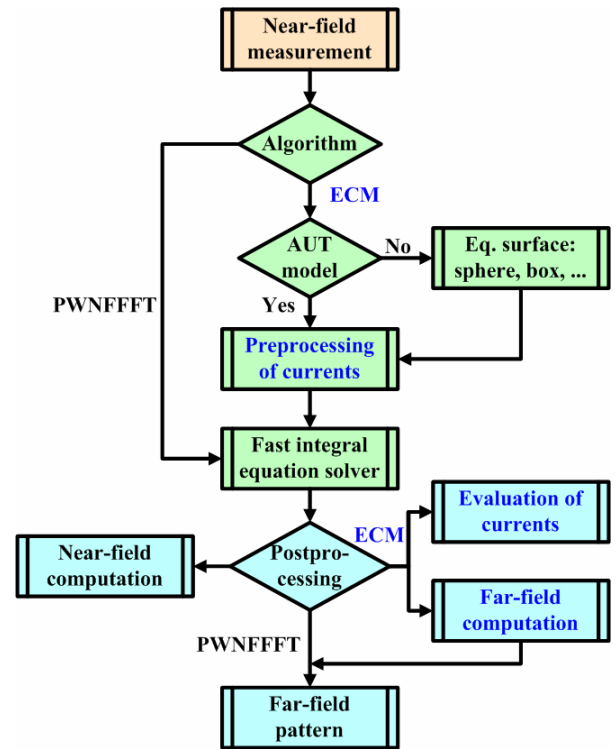


Fig. 4. Flowchart of near-field transformation.

First the near-field of the AUT is sampled in typically two polarizations. For the ECM it is possible to assume the equivalent currents on a model of the AUT. Alternatively they can be assumed on arbitrary surfaces, typically enclosing the AUT. The currents are converted to propagating plane

waves in a preprocessing step. That is where the PWNFFFT starts. The inverse problem is solved employing the FMM fast integral equation solver. Near-field values can be computed from both the equivalent currents as well as the plane waves. For the PWNFFFT no further computations are required to obtain the far-field pattern of the AUT, whereas further computations are required for the ECM. For the ECM, the equivalent currents can be evaluated for diagnostic purposes.

V. RESULTS

Both ECM and PWNFFFT algorithms have been applied to a near-field measurement scenario. A Kathrein base station antenna was measured at 1.92 GHz using a spherical NSI near-field scanner [19] and an open-ended waveguide probe. The antenna has a height of 1.3 m which equals 8.3λ . The parameters of the measurement setup are summarized in Table 1. Fig. 5 shows the equivalent currents determined by the ECM approach on a rectangular box surrounding the AUT. Some clues on the radiating elements inside the radome can be obtained. Nevertheless, a model of the base station antenna would deliver more detailed diagnostic information like the excitation levels of the single radiators.

Table 1. Parameters of measurement setup.

AUT	Kathrein base station antenna 742 445
Measurement type	Spherical
Probe	WR 430 OEWG
Frequency	1.92 GHz
Antenna size	1.3 m \square 8.3λ
Measurement distance	2.715 m

The transformed far-field pattern is shown in Fig. 6 in E- and H-plane cuts and compared to the reference pattern obtained from the commercial NSI2000 software. With respect to the large dynamic range of 60 dB in the E-plane cut, a good agreement with the reference could be achieved.

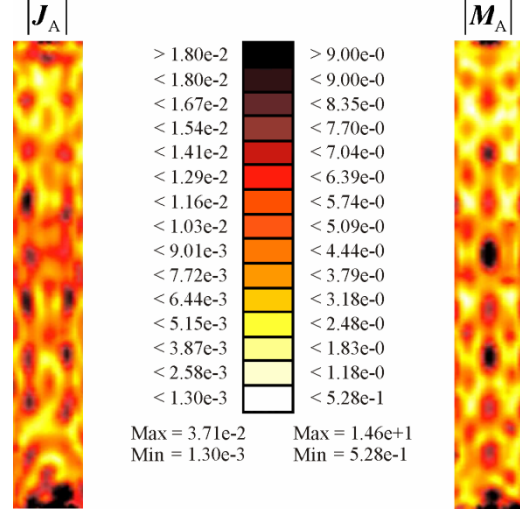


Fig. 5. Equivalent currents on rectangular box surrounding base station antenna.

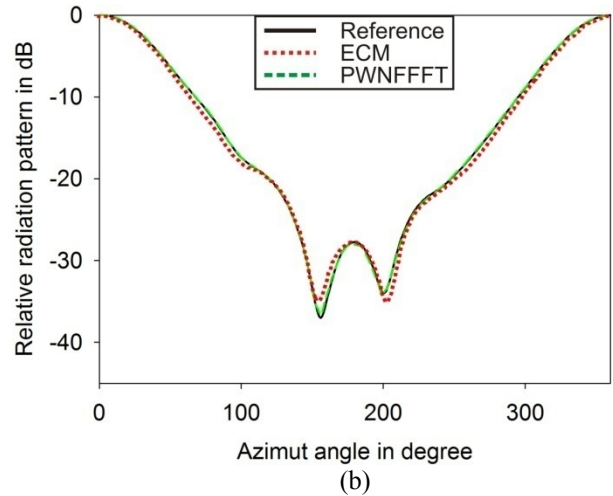
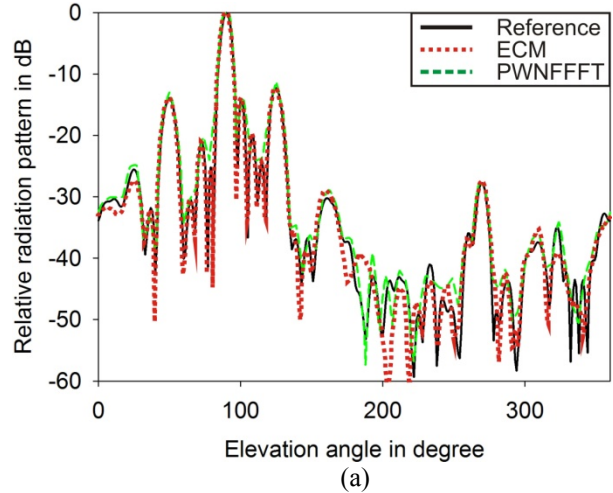


Fig. 6. Reference and transformed far-field patterns of base station antenna. (a) E-plane cut. (b) H-plane cut.

VI. ELECTRICALLY LARGE ANTENNAS AND NON-IDEAL MEASUREMENT ENVIRONMENTS

The low complexity of the algorithms due to the diagonal translation operators can be further enhanced in a multilevel version [12,20] analog to the multilevel fast multipole method (MLFMM) [14]. Therefore the measurement points are grouped in a multilevel box structure and the plane waves are no longer translated to every measurement point explicitly. Instead the plane waves are translated to the box centers on the highest level and are further processed through the different levels towards the measurement points using disaggregation and anteprolation. Disaggregation is a simple phase shift between the box centers on adjacent levels or the lowest level of the box structure and the measurement points respectively. Anteprolation can be seen as counterpart to interpolation and it reduces the sampling rate of the plane wave spectrum according to its spectral content with decreasing box sizes on the various levels. The probe correction is performed on the lowest level of the box structure for a minimum number of plane wave samples. The hierarchical field representation is the principal point for reducing the computational complexity of the algorithm from $O(N^2)$ to $O(M\log N)$, N being the number of measurement points.

For measurement points fulfilling the far-field condition, efficient far-field translations, utilizing a single plane wave in the direction towards the measurement point, can be used. In order to relax the far-field criterion, the AUT can be recursively subdivided into smaller source boxes with a reduced far-field distance. The probe output voltage is obtained as superposition of the individual source boxes. Near- and far-field translations are combined in a hybrid approach in order to optimize the overall complexity [21].

The plane wave characteristic of the equivalent sources allows to utilize reflection and diffraction concepts also in near-field distance to the AUT. Subdividing the AUT in source boxes and utilizing far-field translations, infinite perfectly conducting ground planes and dielectric halfspaces, as approximation for real ground effects, can be considered in the transformation algorithm by superimposing ground reflected waves with the line-of-sight waves [20]. More complex obstacles and

scattering objects can be considered by an MLFMM-UTD hybrid approach [22], if sufficient a priori knowledge is given. Unknown scattering objects and non-ideal measurement environments are modeled as additional sources via scattering centers [23]. The plane waves representing the AUT as well as the additional scattering centers are determined in the inverse solution process. Only some oversampling of the measured fields is required to determine the additional unknowns.

Key features of the algorithms include:

- Low complexity of $O(M\log N)$
- Arbitrary measurement grids possible
- Full probe correction
- Antenna diagnostics
- Integration of scattering contributions possible

VII. CONCLUSION

An equivalent current method as well as a plane wave based near-field transformation have been discussed. Due to the integral equation formulation, these approaches are well suited for irregular measurement grids and a full probe correction is easily integrated without increasing the complexity. Fast solver techniques and a hybrid formulation utilizing combined near- and far-field translations allow an efficient transformation also for electrically large antennas with a low complexity. The plane wave based formulation allows for the compensation of ground reflections and also the effects of non-ideal measurement environments can be countered by introducing a scattering center approach.

ACKNOWLEDGEMENT

The authors are grateful to KATHREIN-Werke KG, Rosenheim, Germany for providing the near-field measurement data as well as the NSI transformed far-field pattern in the results section.

REFERENCES

- [1] C. A. Balanis, *Modern Antenna Handbook*. John Wiley & Sons, Inc., 2008.
- [2] G. Hindman and D. S. Fooshe, "Probe Correction Effects on Planar, Cylindrical and Spherical Near-Field Measurements," *An-*

- tenna Measurement Techniques Association Conference, 1998.*
- [3] A. D. Yaghjian, "An Overview of Near-Field Antenna Measurements," *IEEE Trans. Antennas Propag.*, vol. 34, no. 1, pp. 30-45, Jan. 1986.
- [4] J. Hansen, *Spherical Near-Field Antenna Measurements*. Exeter, U.K.: IEE Electromagnetic Wave Series 26, 1988.
- [5] D. Kerns, "Plane-Wave Scattering-Matrix Theory of Antennas and Antenna-Antenna Interactions," *National Bureau of Standards*, Boulder CO, 1981.
- [6] R. C. Wittmann, B. K. Alpert, and M. H. Francis, "Near-Field Spherical-Scanning Antenna Measurements With Nonideal Probe Locations," *IEEE Trans. Antennas Propag.*, vol. 52, no. 8, pp. 2184-2186, August 2004.
- [7] R. C. Wittmann, B. K. Alpert, and M. H. Francis, "Near-Field Antenna Measurements Using Nonideal Measurement Locations," *IEEE Trans. Antennas Propag.*, vol. 46, pp. 716-722, May 1998.
- [8] M. M Leibfritz and F. M. Landstorfer, "Full Probe Correction for Near-Field Antenna Measurements," *IEEE APS International Symposium*, Albuquerque, USA, 2006.
- [9] T. K. Sarkar and A. Taaghoul, "Near-Field to Near/Far-Field Transformation for Arbitrary Near-Field Geometry Utilizing an Equivalent Electric Current and MoM," *IEEE Trans. Antennas Propag.*, vol. 47, no. 3, pp. 566-573, March 1999.
- [10] K. Persson and M. Gustafsson, "Reconstruction of Equivalent Currents Using a Near-Field Data Transformation - with Radome Application," *Progress In Electromagnetics Research*, PIER 54, pp. 179-198, 2005.
- [11] Y. Alvarez, F. Las-Heras, and M. R. Pino, "Reconstruction of Equivalent Currents Distribution Over Arbitrary Three-Dimensional Surfaces Based on Integral Equation Algorithms," *IEEE Trans. Antennas Propag.*, vol. 55, no. 12, pp. 3460-3468, Dec. 2007.
- [12] T. F. Eibert and C. H. Schmidt, "Multilevel Fast Multipole Accelerated Inverse Equivalent Current Method Employing Rao-Wilton-Glisson Discretization of Electric and Magnetic Surface Currents," *IEEE Trans. Antennas Propag.*, vol. 57, no. 4, pp. 1178-1185, April 2009.
- [13] R. Coifman, V. Rokhlin, and S. Wandzura, "The Fast Multipole Method for the Wave Equation: A Pedestrian Prescription," *IEEE Antennas and Propag. Mag.*, vol. 35, no. 3, pp. 7-12, Jun. 1993.
- [14] W. C. Chew, J. M. Jin, E. Michielssen, and J. M. Song, *Fast and Efficient Algorithms in Computational Electromagnetics*, Artech House, Inc, 2001.
- [15] C. H. Schmidt, M. M. Leibfritz, and T. F. Eibert, "Fully Probe-Corrected Near-Field Far-Field Transformation Employing Plane Wave Expansion and Diagonal Translation Operators," *IEEE Trans. Antennas Propag.*, vol. 56, no. 3, pp. 737-746, March 2008.
- [16] S. M. Rao, D. R. Wilton, and A. W. Glisson, "Electromagnetic Scattering by Surfaces of Arbitrary Shape," *IEEE Trans. Antennas Propag.*, vol. 30, no. 3, pp. 409-418, May 1982.
- [17] A. Tzoulis and T.F. Eibert, "Efficient Electromagnetic Near-Field Computation by the Multilevel Fast Multipole Method Employing Mixed Near-Field/Far-Field Translations," *IEEE Antennas Wireless Propag. Lett.*, vol. 4, pp. 449-452, 2005.
- [18] Y. Saad, *Iterative Methods for Sparse Linear Systems*, Society for Industrial and Applied Mathematics, 2nd edn., 2003.
- [19] Nearfield Systems Inc., <http://www.nearfield.com>.
- [20] C. H. Schmidt and T. F. Eibert, "Multilevel Plane Wave Based Near-Field Far-Field Transformation for Electrically Large Antennas in Free-Space or Above Material Halfspace," *IEEE Trans. Antennas Propag.*, vol. 57, no. 5, pp. 1382-1390, May 2009.
- [21] C. H. Schmidt and T. F. Eibert, "Hybrid Multilevel Plane Wave Based Near-Field Far-Field Transformation Utilizing Combined Near- and Far-Field Translations," *Advances in Radio Science*, vol. 7, pp. 17-22, 2009.
- [22] A. Tzoulis and T. F. Eibert, "A Hybrid FEBI-MLFMM-UTD Method for Numerical Solutions of Electromagnetic Problems Including Arbitrarily Shaped and Electrically Large Objects," *IEEE Trans. Antennas*

Propag., vol. 53, no. 10, pp. 3358-3366, Oct. 2005.

- [23] C. H. Schmidt and T. F. Eibert, "Near-Field Far-Field Transformation in Echoic Measurement Environments Employing Scattering Center Representations," *3rd European Conference on Antennas and Propagation*, Berlin, Germany, March 2009.



Carsten H. Schmidt was born in Stuttgart, Germany, in 1982. He received the Dipl.-Ing. degree in electrical engineering from the Universität Stuttgart, Stuttgart, Germany, in 2007.

From 2007 to 2009, he was with the Institute of Radio Frequency Technology, Universität Stuttgart and was working towards the Dr.-Ing. degree. From November 2008 to April 2009, he was a Visiting Ph.D. Scholar at the Antenna Research, Analysis and Measurement Laboratory, University of California, Los Angeles, under the supervision of Prof. Yahya Rahmat-Samii. Since October 2009, he has been a research group leader at the Lehrstuhl für Hochfrequenztechnik, Technische Universität München, Munich, Germany. His main research interests are antenna measurement techniques as well as computational electromagnetics.



Thomas F. Eibert received the Dipl.-Ing.(FH) degree from Fachhochschule Nürnberg, Nürnberg, Germany, the Dipl.-Ing. degree from Ruhr-Universität Bochum, Bochum, Germany, and the Dr.-Ing. degree from Bergische Universität Wuppertal, Wuppertal, Germany, in 1989, 1992, and 1997, all in electrical engineer-

ing. From 1997 to 1998, he was with the Radiation Laboratory, EECS Department of the University of Michigan, Ann Arbor, from 1998 to 2002, he was with Deutsche Telekom, Darmstadt, Germany, and from 2002 to 2005, he was with the Institute for High-frequency Physics and Radar Techniques of FGAN e.V., Wachtberg, Germany, where he was head of the Antennas and Scattering Department. From 2005 to 2008 he was a Professor for radio frequency technology at Universität Stuttgart, Stuttgart, Germany. Since October 2008, he has been a Professor for high-frequency engineering at the Technische Universität München, Munich, Germany.

His major areas of interest are numerical electromagnetics, wave propagation, measurement techniques for antennas and scattering as well as all kinds of antenna and microwave circuit technologies for sensors and communications.

FPGA Accelerated Phased Array Design Using the Ant Colony Optimization

Ozlem Kilic

Department of Electrical Engineering and Computer Science
The Catholic University of America, Washington, DC, USA
kilic@cua.edu

Abstract – The objective of this paper is to investigate the utilization of field programmable gate arrays (FPGA) in the field of electromagnetics by applying the ant colony optimization (ACO) method in the design of phased array antennas for multiple beam satellite communication systems. The amplitudes of the array elements are optimized to reduce the co-channel interference in a multiple beam satellite communication system. The potential gains in the speed of the calculations are investigated in comparison to conventional simulation techniques of the same application on a regular PC. Two different FPGA platforms and implementation approaches are compared for performance to two software developments implemented using Matlab and C languages. It has been shown that significantly accelerated performance can be achieved for the particular application. This kind of speed improvement can enable handling more complex requirements and constraints for the same application in a very reasonable amount of time, which would otherwise be impossible with conventional computational platforms and techniques. This magnitude of speed improvement is due to the configurable nature of the FPGAs. Unlike central processing units (CPU) in a conventional computer, which have to deal with a preset set of instructions to properly function; FPGAs are completely programmable to carry out a set of functions in the most efficient manner for the particular algorithm at hand. In this study, the FPGA has been configured to function as an efficient “ACO machine.” Both parallelization and pipelining have been utilized to achieve this performance. The details of the implementation on the FPGA platform and the achieved acceleration are discussed in the paper.

Index Terms - FPGA, parallel computing, reconfigurable programming, HPC, ant colony optimization, phased arrays, satellite communications, interference.

I. INTRODUCTION

The need for faster computations in the electromagnetics community has been a bottleneck for some of the modern applications such as smart antennas, advanced rf materials, etc. These devices utilize complex structures and demand ambitious performance within their operational environment. It is often necessary to simulate the performance of components and platforms as a single system in the design stage. As a result, accurate and fast modeling of large scale structures with fine features often becomes a challenge. Conventional full wave simulation techniques typically are not capable of solving such problems due to limitations in computational resources. Often, researchers resort to asymptotic or hybrid techniques in order to obtain a “reasonably accurate” solution.

The challenge becomes even bigger when the performance of these complex designs needs to be optimized over a set of constraints and parameters. Often the classical optimization techniques are not suitable because they typically require an initial estimate reasonably close to the final result in order to avoid stagnation at a local optimum point. They also tend to require analytical calculations such as derivatives that take computational time. Recently nature based heuristic optimization methods have gained attention in the electromagnetics community due to their robust random search mechanisms which have long been utilized for survival by different species.

Furthermore, these algorithms are inherently parallel in nature, which allows for accelerated computing.

The supercomputing systems, which can potentially handle numerically intensive problems, are not commonly available because of their cost. Hardware accelerated computing has been gaining momentum over the last decade due its applicability to parallel computing while using a fraction of the power requirements of the conventional microprocessors and requiring much less cost in comparison to supercomputers.

The objective of this paper is two folds: (i) investigate the use of field programmable gate arrays (FPGAs) in numerically intensive electromagnetic simulations, (ii) utilize the parallel nature of the ant colony optimization to accelerate the optimization of complex electromagnetic problems. Since FPGAs can be instantly reconfigured to carry out different tasks simultaneously, they offer a natural choice for this application.

II. RECONFIGURABLE COMPUTING WITH FPGAs

An FPGA is a type of programmable chip that can be configured to behave in just about any way the programmer wishes enabling them to be highly efficient platforms. Over the last decade, FPGAs have established themselves as the third programmable platform after microprocessors and digital signal processor (DSP) chips, [1]. While in the past the use of DSPs was ubiquitous, the utilization of FPGAs is growing rapidly due to the need for processing millions of instructions per second (MIPS). The primary reason FPGAs are preferred over DSPs is in fact driven by the application's MIPS requirement, [2]. Three factors have driven the interest on these devices: performance, cost and their reconfigurable nature. Their high performance relies on the parallel implementation that they naturally offer. This feature allows packing massive amounts of processing performance in a single package, eliminating the need to utilize different hardware components for different applications. Furthermore, the algorithms can be optimized over the reconfigurable hardware to avoid any overhead

associated with the fixed instruction sets of microprocessors.

FPGAs are reprogrammable silicon chips in a two dimensional array of logic cells. A logic-cell is essentially made up of a small lookup table (LUT), a flip-flop and a 2-to-1 multiplexer, which can be used to bypass the flip-flop if necessary. Each logic-cell can be connected to other logic-cells through interconnect resources; i.e. wires placed around the logic-cells. Complex logic functions can be created by connecting hundreds or thousands of these logic cells together. In addition to these interconnect resources; FPGAs also have fast dedicated lines in between neighboring logic cells allowing the efficient creation of arithmetic functions. A schematic of the FPGAs is demonstrated in Figure 1.

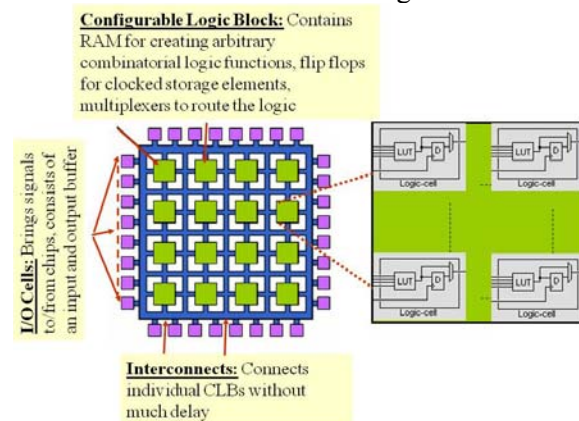


Fig. 1 Schematic diagram of FPGA components and functionality.

FPGAs can offer significant speed improvement compared to CPUs, [3] and have better price per performance ratio. They are still keeping up with Moore's law, roughly doubling their performance every 18 months. Furthermore, they have lower power consumption per computation, which makes them very attractive for very large problems. One of the main advantages of FPGAs is that they can dynamically create processing engines that fit the algorithm problem rather than fitting the algorithm to particular processor architecture. Despite all the advantages, FPGAs are finding their way to scientific computing rather slowly due to two challenges: (i) The programming on the chip requires significant hardware knowledge as well as understanding of the parallel nature of the algorithm to be implemented, (ii) FPGAs are best suited for

integer calculations and floating point calculations are often required in scientific applications. Nevertheless, researchers have been utilizing this platform for electromagnetic applications, [4] [5].

III. THE ANT COLONY OPTIMIZATION (ACO) ALGORITHM

The ACO algorithm mimics the behavior of ants in their search for the shortest path between their nest and the food. Although ants are nearly blind animals, they demonstrate the capability to establish the shortest path between their nest and food. The ethologists have discovered that ants deposit a chemical substance called pheromone on their paths, which is used by other ants in their search process. The most traveled path is marked with the highest level of pheromone. This positive feedback behavior allows more ants to choose the path with the most pheromone amount, [6]. The algorithm for this concept is demonstrated in Fig. 2. The ants serve as agents that search the optimization space for a satisfactory solution. The cost function is a measure of how satisfactory a solution is, with low cost implying a “better” solution. The description of the cost function is application dependent and is one of the most critical parts of the algorithm in terms of efficiency and accuracy. The random search is iteratively applied by the ants until one of the chosen paths satisfies the required convergence criteria.

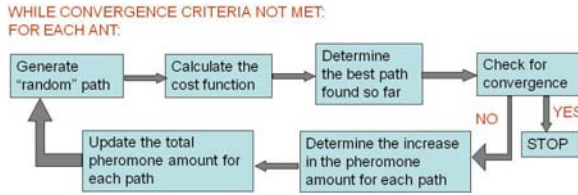


Fig. 2. ACO algorithm.

The ACO algorithm is based on selection of different paths, and therefore inherently applies to a discrete set of choices at each decision point. As a consequence, ACO is suitable for non-continuous optimization domains. However, for electromagnetics and antenna problems, the optimization domain usually consists of a

continuous range of choices. Continuous problems have been solved for by modifications to the ACO algorithm, [7]-[10]. This paper utilizes the Touring ACO by Hiroyasu, [7] where the solution is represented as a string of bits so that the path to decide is the bit values for this binary string, as shown in Fig. 3.

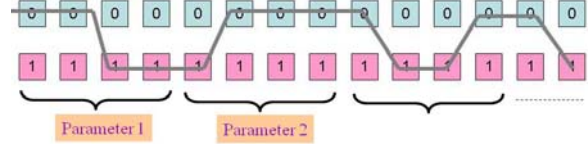


Fig. 3 The binary path for ACO in continuous domain.

The probability of a zero or one for each bit position is calculated from the total pheromone levels for the path for bit value of zero and one at each position as a function of the pheromone levels on the path as follows:

$$\rho_0(t+1) = \frac{\tau_0(t+1)}{\tau_0(t+1) + \tau_1(t+1)} \quad (1)$$

In equation (1), τ_0 denotes the total pheromone amount for bit value of zero at a given stage, and is computed from the sum of all pheromone amounts laid by all ants in the current iteration plus an “evaporated” amount of pheromone laid before in previous iterations, as shown in equation (2). The total pheromone amount for bit value of 1, τ_1 is calculated in a similar fashion. The coefficient ρ represents the evaporation parameter, and $1-\rho$ is the evaporation amount. This simulates nature’s influence on the pheromone amounts that have been laid a while back. The increase in the total pheromone amounts due to each ant is inversely proportional to the cost function, $C_{k_{ant}}$. The incremental pheromone values $\Delta\tau_0^{k_{ant}}$ and $\Delta\tau_1^{k_{ant}}$ correspond to the bit value zero and one, respectively.

$$\tau_0(t+1) = \rho\tau_0(t) + \sum_{k_{ant}} \Delta\tau_0^{k_{ant}}(t, t+1) \quad (2)$$

$$\Delta\tau_0^{k_{ant}}(t, t+1) = \begin{cases} \frac{1}{C_{k_{ant}}} & \text{if } k_{ant} \text{ chooses 0 for the current bit} \\ 0 & \text{else} \end{cases}$$

IV. THE APPLICATION: OPTIMIZATION OF PHASED ARRAYS FOR MULTIPLE BEAM SATELLITE COMMUNICATIONS

In cellular satellite communications systems, a given coverage area is typically filled with a number of contiguous spot beams, which carry concentrated radiation along preferred directions. Since large areas are served in satellite communications, many beams need to be generated by the satellite antenna. Due to limited available bandwidth, the same frequency bands are often reused in cells separated apart from each other to accommodate the traffic. The frequency reuse approach results in co-channel interference due to the energy leaking from beams operating at the same frequency into each other. The concept of frequency reuse for a multiple beam satellite communication system is demonstrated in Fig. 4, where the beams operating at the same frequency are denoted with the same color. A reuse factor of 7 is shown in this figure; i.e. the same frequency is repeated every seven beams in the coverage area. In such a configuration, there is a potential of energy leak into beams operating at the same frequency through the side lobes of the radiation for an intended beam. Such a design often relies on the spatial isolation of these co-channel beams for reduced interference. However, if there are a substantial number of them, the resultant noise can be detrimental to the operation of the system.

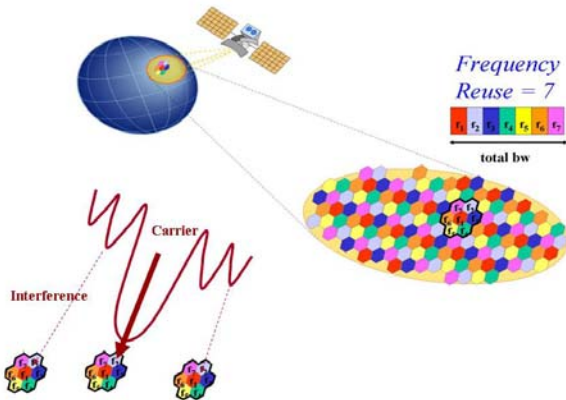


Fig. 4. Co-channel interference concept for multiple beam satellite communications systems.

This paper discusses the optimization of phased array antenna patterns to minimize this co-channel noise for multiple beam satellite systems. The noise the paper is concerned with is due to the interference from other beams in the system. The antenna pattern is manipulated by changing the amplitudes of the array elements so that the radiation along the direction of the co-channel beam centers is reduced below a threshold placing nulls in the antenna pattern along these directions. A linear array will be assumed for ease of computations with the understanding that the algorithm can be easily modified to adapt to a planar array. The only anticipated challenge in modifying the algorithm to planar arrays is the requirement to solve for a larger number of unknowns.

Numerous nature inspired optimization algorithms, including ACO, has been successfully applied to this problem before using conventional programming techniques on CPU, [11]. The optimization problem involves the computation of the array factor for a given array geometry and reducing the radiation levels along the co-channel beam directions. For a linear array with equally spaced elements, the array factor, $f(\theta)$ and the normalized radiation pattern, $U_n(\theta)$ can be calculated as given in [12] as follows:

$$f(\theta) = \left| \sum_{m=0}^{N-1} I_m e^{j\varphi_m} e^{+jmkd \cos \theta} \right| \quad (3)$$

$$U_n(\theta, \varphi) = |f_n(\theta)|^2 |e(\theta, \varphi)|^2 \quad (4)$$

where m is an index over element number, N is the total number of elements, I_m , φ_m are the amplitude and phase of the m^{th} element, d is the center-to-center separation between elements, $\kappa = 2\pi/\lambda$ is the wave number, and θ, φ are the observation angles with respect to the array axis. To further simplify the analysis, the individual elements are assumed to be isotropic sources; i.e. $e(\theta, \varphi) = 1$. With these assumptions, the normalized radiation pattern is the square of the array factor, and the optimization can be based solely on the array factor calculations. A uniform phase distribution is assumed, and the

optimization searches for a suitable set of J_m values to achieve the desired radiation performance.

V. FPGA IMPLEMENTATION OF ACO ALGORITHM FOR PHASED ARRAY OPTIMIZATION

Two target platforms were chosen for running the ACO on an FPGA: (i) Silicon Graphics (SGI) Altix 450 system, (ii) ML510 development board based on Xilinx Virtex-5 FX130T FPGA. The Altix system is configured with two Itanium processor based compute blades and a Reconfigurable Application-Specific Computing (RASC) blade. The RASC blade comprises of two Xilinx Virtex 4 XC4VLX200 FPGAs. The ML510 board is an embedded development platform with a 512 MB Compact Flash card and two 512 MB DDR2 DIMMs. Both platforms have a CPU connected to an FPGA, but using different I/O mechanisms in the hardware (NUMALink and Core Services for SGI, APU for the ML510).

Mapping such an algorithm to an FPGA is different than programming a Van Neumann machine. Rather than a program counter controlling sequencing of instruction execution, data counters are used to control the streaming of data through a pipelined array of processing elements. Functions of the processing elements are fixed and data is passed from one processing element to the next, eliminating the need to move data in and out of memory as a shared processing resource steps through the processing sequence of the algorithm. One must also be aware of the resources available (i.e. internal registers, look-up tables RAM, multipliers and accumulators) when determining the way in which parallelism is achieved in an FPGA.

The ACO algorithm has multiple processing functions that are repeatedly performed as described earlier in the flowchart in Fig. 2. There are three major sections to the algorithm: Path Generation, Cost Calculation and Pheromone Update, which comprise a recursive pipeline. Additional logic monitors the process to determine when the algorithm has converged, and forwards the resulting data to the application running on the compute blade. Researchers have successfully implemented ACO on FPGA platform before,

where in [13] a simplified form of ACO, namely P-ACO, was used to be able to fit the code on the Virtex-II Pro Platform utilizing FPGA XC2VP125. In [14] the authors utilize the FPGA as a coprocessor to the CPU, which carries out the controller evaluation functionalities.

This paper implements the ACO algorithm entirely on a single FPGA by using two different approaches. The first approach uses a highly efficient VHDL code on the SGI Altix platform. The second approach utilizes a software interface to the VHDL, ImpulseC, to implement the code in a C-like environment on the ML510 board. Details on the development for both approaches and a comparison of their performances are provided in the following sections.

V.1 VHDL Implementation on Altix 450

Path Generation updates the binary paths as discussed in Fig. 3. For this simulation, paths are produced using 8 bits for each optimization parameter (i.e. the amplitudes of the array elements), 40 parameters in each ant path (i.e. the number of array elements), 40 ant paths per iteration (i.e. 40 ants carry search for a solution simultaneously in each iteration), and as many iterations as it takes to converge, with an upper limit set by the user. These data are generated at the bit level. For each bit, the probability is maintained as to whether that bit is a one or a zero. The new path is generated based on these probability values. With this implementation, increasing the number of bits per parameter will increase the FPGA resource requirement for this function, but will not increase the processing time.

Streaming data from the Path Generation is fanned-out to parallel Multiply-Accumulators (MAC) in the Cost Calculation, as shown in Fig. 5. Separate MACs provide simultaneous updates to the cost function for each null, processing each parameter in every path. Note that the coefficients that describe the desired null pattern are stored in the FPGAs Block RAM. Four of these Block RAMs are used for each coefficient to provide the required 32-bit data width. After these MACs, the number of computations decreases to just the number of nulls. A multiplexer is employed to funnel data into divider that normalizes the data that has been accumulated. These numbers are accumulated to a single sum and a cost function is applied to generate the total cost for each ant path.

Based on this cost, the pheromone levels along each path and the probability of 0/1 at each bit position in the binary string is updated as shown in Fig. 6.

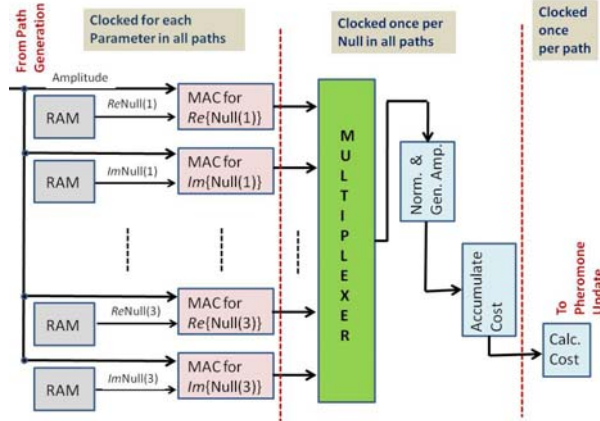


Fig. 5. Cost calculation block diagram.

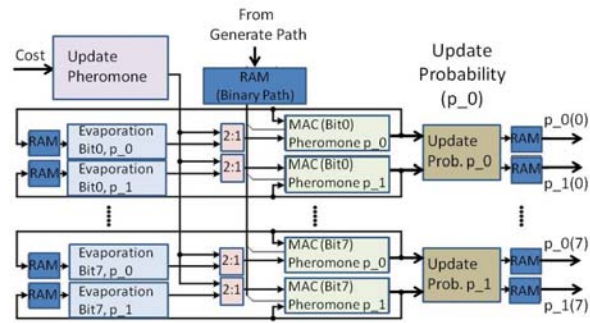


Fig. 6. Pheromone update block diagram.

The time required to process data with this FPGA implementation is shown in the timing diagram in Fig. 7, where Clk is the 100 MHz system clock. The Reset signal starts the first iteration of the algorithm, while the Restart signal starts the subsequent iterations of the algorithm. A timing strobe denoted by pSOF is used to increment the AntCount, which keeps track of the path being processed. GPFirstAntOut and GPLastAntOut are timing strobes that mark the start of the first and last path outputs from Generate Path. The flow of probability data from Pheromone Update to Generate Path is controlled by the data counter pCount, and AmpSOF is a timing strobe that marks the beginning of data flow out of the Path Generation section.

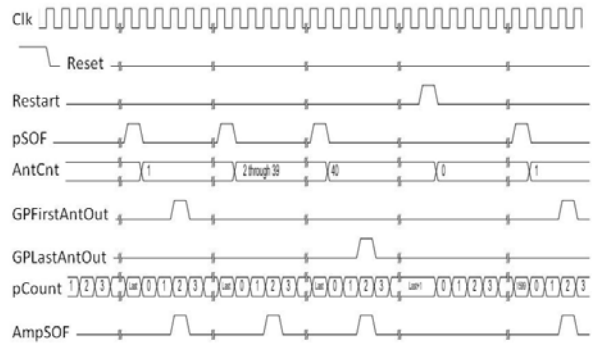


Fig. 7. Timing diagram of ACO.

By running the FPGA at 100 MHz clock rate, the data is processed at a rate of 10 ns per clock. Parameters are processed on each clock cycle, with a one path delay at the beginning, due to amplitude normalization in Path Generation, and a one path delay at the end due to probability update in Pheromone Update. It should be noted that this path delay at the end is not shown in the timing diagram, but is enforced by the Restart, which is issued by Pheromone Update once the last path computations have completed.

For 40 parameters per path and 40 paths per iteration, the best expected run time per iteration is at about 16.8 μ s (= 10 ns/ parameter * 40 parameters/path * 42 paths/iteration). It should be noted that 42 paths were used to account for the one path delay at the beginning, due to amplitude normalization in Path Generation, and a one path delay at the end due to probability update in Pheromone Update. For the planar array case (i.e. 40x40 array), run time is expected to be about 672 ms/iteration (= 10 ns/ parameter * (40*40) parameters/path * 42 paths/iteration).

V.2 Impulse C Implementation on ML510

SGI's Altix 450 platform is a highly efficient structure that integrates CPU with FGAs and utilizes shared memory to reduce any bottlenecks for data access. However, it is a highly sophisticated platform that requires expertise in programming on such platforms. Since expertise on such customized platforms are not common for the researched who is not in the field of FPGA computing, it was deemed of interest to implement the same algorithm on a more readily found FPGA card utilizing a software interface that helps simplify FPGA programming. The block diagram below shows the CPU-FPGA architecture for the

ML510 development board using Impulse C language as an interface. A C-like code is used with interpreted commands that translate into HDL implementation of the code by utilizing parallelism and pipelining. The development of the code utilizes the functions Impulse C provides for pipelining and parallelization, and the user can avoid working with the detailed timing diagrams as in the VHDL implementation. Impulse C generates the necessary timing for the specific FPGA platform it supports. Compiling the Impulse C code to the FPGA device involves two main steps: (i) Generating HDL and exporting from Impulse CoDeveloper, (ii) Synthesizing and mapping to the FPGA board using Xilinx ISE. Since the first step is automated by Impulse C, the user has limited control on the specifics of the HDL code generated in comparison to the first approach where the VHDL code was developed manually. The algorithm was compiled at 100 MHz as in the SGI Altix implementation and a bit file was created successfully. Therefore, the devices are running at the same speed for identical algorithms for a fair comparison of efficiency. The algorithm was run numerous times and an average run time of 0.3 milliseconds per iteration was observed. While the time for implementation of the code can be significantly reduced by using a software interface, a significant price in the run time efficiency is paid for as a result.

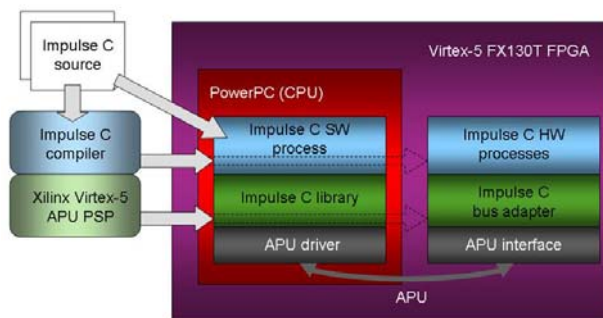


Fig. 8. CPU-FPGA architecture for the ML510 implementation.

VI. SIMULATION RESULTS – COMPARISONS OF FPGA, C AND MATLAB IMPLEMENTATIONS

As in all heuristic optimization methods, the performance of the algorithm depends on how the

convergence criteria and cost function are defined. The cost function is defined such that a 25% drop in the peak gain is allowed while requiring the power levels along the direction of co-channel beams to be at least 40 dB down. For simulation purposes in this investigation, the centers of six co-channel beam locations were considered; at 3.75, 6.34 and 9.00 degrees off the main direction on either side. A linear array of 40 elements, with center-to-center element separation of half a wavelength was considered, and symmetry was employed; i.e. amplitude and phase values of the array elements were assumed symmetric with respect to the center of the array. The optimization space was sampled by 40 ants using eight bits per each optimization parameter. Due to the symmetry assumption, the number of unknowns is 20, half of the number of array elements. Therefore, the binary string generated by each ant is 160 (=20x8) bits long.

When the algorithm was run on a standard PC (CPU: Intel Pentium M, 3 GHz and RAM: 1 GB) using Matlab, the time per a single iteration took about 0.47 seconds. The same algorithm when implemented on C and run on the same platform ran about 53.4 times faster than the Matlab version, roughly at 8.8 milliseconds per iteration. The VHDL implementation on the Altix 450 system performed at 31.3 microseconds for runs after the bit loading was completed, resulting in a factor of 15,160 in speed compared to the Matlab implementation. The same algorithm took 102.1 microseconds per iteration including the bit loading, resulting in a factor of 4,607 in speed compared to the Matlab implementation. It should be noted that the bit loading is only necessary when the algorithm is first run. Later runs do not need this process as the FPGA is already configured. The FPGA implementation using VHDL on Altix 450 system performed 100 times faster than the implementation on ML510 board using Impulse C language. The results of the algorithm are demonstrated for different convergence criteria (0.001, 0.07 and 0.20) in Fig. 9. The most strict case (err = 0.001) took on average 12 minutes to complete. The second case (err = 0.07) converged in about 0.4 minutes. Finally, the least strict case (err = 0.20) took 0.01 minutes to complete. These times are based on average numbers for multiple runs of the same criteria.

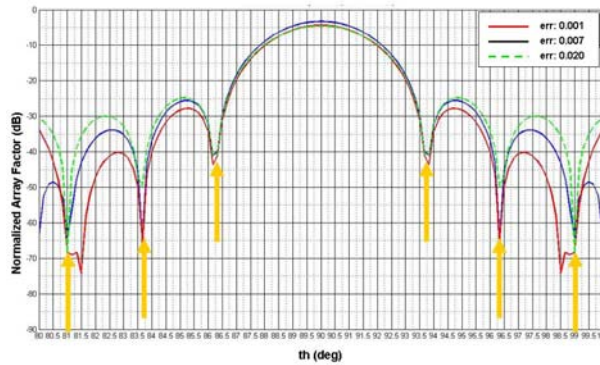


Fig. 9. Optimized antenna pattern for six co-channel beam centers - FPGA implementation on SGI Altix Platform.

VII. THE PROCESS FOR RUNNING THE ALGORITHM ON THE FPGA

There are significant differences between conventional software design flow and a hardware design flow for FPGAs, [15]. A multistage process is completed before a design can be used in an FPGA. These stages include synthesis, verification, translation, mapping, place and route. Synthesis stage is where the hardware description language code (e.g. VHDL, Verilog) is translated into a text description of a schematic. The verification step is to ensure that the specified design of the first step is functional. The translation means the conversion of this text description into a binary format. At this stage all the components and connections are mapped to the configurable logic blocks. The place and route stage is when the design is fitted onto the target FPGA. As a result of these stages a *.bit file, which is a configuration file to program the FPGA resources, is created to load the design onto the FPGA. Once all these stages are completed, the algorithm can be run repeatedly, without having to repeat these steps.

This multi-stage process in addition to the need to efficiently utilize available FPGA resources through pipelining and parallelism requires a steep learning curve for a scientist who is used to the conventional programming techniques. It is this aspect of the FPGAs that hinders the wide use of these platforms in the broader scientific community. Another key

difference between FPGA implementation versus conventional programming is the compilation times. Software compilation is shorter than the hardware implementations and debugging can be done as an iterative approach. However, in the hardware approach the mapping of a defected design can cause significant delays in the place and route stage and should be avoided.

VIII. CONCLUSIONS

The utilization of FPGAs in the field of electromagnetics has been investigated by optimizing the radiation pattern of an array antenna using the ant colony optimization method. The acceleration performance in comparison with conventional programming techniques has been shown to be in the order of 15,000 for the particular application using a clock speed of 100 MHz. This order of magnitude of speed improvement can enable handling more complex requirements and constraints for the same application in a very reasonable amount of time, which would otherwise be impossible with conventional computational platforms and techniques.

This study demonstrates that FPGAs have tremendous potential for scientific computing. However, the problem investigated was small enough to be custom fit on a single FPGA, which enabled the high acceleration achieved. In more challenging electromagnetic problems, improvements at this magnitude may not be feasible. The most likely approach in such cases is utilizing the FPGA as a coprocessor to the CPU, which will reduce the acceleration factor. Furthermore, there are significant challenges to be overcome before the FPGAs can be considered as mainstream platforms for scientific computing. The overall acceleration for an application is highly dependent on the nature of the algorithm, required resources and what is available to the programmer, as well as programming skills. Interdependence and resource requirements of processes determine how the code can be parallelized. To optimally utilize the FPGA, the programmer needs to know the available resources and time required for each process. This is often a highly detailed process without access to mainstream products. The device at hand must

have the required resources for a given code. Successfully creating a bitfile for a given design to run at a given clock rate is not always possible for a given FPGA device. This is a fundamental limitation of FPGA development. Often the remedy is only implementing parts of the algorithm on FPGA, and running the rest on the CPU.

REFERENCES

- [1] P. Lysaght; P. A. Subrahmanyam; "Guest Editors' Introduction: Advances in Configurable Computing," IEEE CS and IEEE CASS, pp. 85-89, March-April 2005 Macdonald, V. H.
- [2] "FPGA versus DSP, Design, Reliability and Maintenance," Altera White Paper 01023, www.altera.com/literature/wp/wp-01023.pdf
- [3] Jahyun J. Koo, David Fernandez, Ashraf Haddad and Warren J. Gross; "Evaluation of a High-Level-Language Methodology for High-Performance Reconfigurable Computers," Proc. IEEE Int. Conf. ASAP, pp. 30-35, July 2007.
- [4] O. Kilic, M. S. Mirotznik, J. P. Durbano, "Application of FPGA Based FDTD Simulators to Rotman Lenses," Proc. 2006 ACES Conference, Miami, FL.
- [5] C. He, W. Zhao, and M. Lu, "Time Domain Numerical Simulation for Transient Waves on Reconfigurable Coprocessor Platform," Proc. of the 13th Annual IEEE Symposium on Field-Programmable Custom Computing Machines (FCCM'05), 2005.
- [6] M. Dorigo, V. Maniezzo and A. Colomi, "The Ant System: Optimization by a Colony of Cooperating Agents," IEEE Trans. Systems, Man, and Cybernetics, Part B, Vol:26, No. 1, 1996, pp. 1-13
- [7] T. Hiroyasu, M. Miki, Y. Ono and Y. Minami, "Ant Colony for Continuous Functions," *The Science and Engineering*, Vol. XX, No. Y, Doshisha University, Japan, 2000.
- [8] D. Corne, M. Dorigo, & F. Glover. 1999. The ant colony optimization meta-heuristic. In *New ideas in optimization*, 11-32. M. Dorigo and G. D. Caro, eds. New York: McGraw-Hill.
- [9] W. Lei, and W. Qudi. 2002. Further example study on ant system algorithm based continuous space optimization. *4th World Congress on Intelligent Control and Automation*, Shanghai, China, pp. 2541-2545.
- [10] K. Socha, 2004 ACO for continuous and mixed-variable optimization. *Proc. of 4th International Workshop on Ant Colony Optimization and Swarm Intelligence (ANTS'2004)*, Brussels, Belgium.
- [11] O. Kilic, "Comparison of Nature Based Optimization Methods for Multi-beam Satellite Antennas," Proc. 2008 ACES Conference, Niagara Falls, Canada
- [12] W. A. Stutzman and G. A. Thiele, "Antenna Theory and Design," Artech House, 1997.
- [13] B. Scheuermann, K. Sob, M. Guntsch, M. Middendorf, O. Diessel, H. ElGindy and H. Schmeck, "FPGA implementation of population-based ant colony optimization", *Applied Soft Computing*, Vol. 4, Issue 3, August 2004, pp 303-322.
- [14] Chia-Feng Juang, Chun-Ming Lu, Chiang Lo, and Chi-Yen Wang, "Ant Colony Optimization Algorithm for Fuzzy Controller Design and Its FPGA Implementation", *IEEE Transaction on Industrial Electronics*, Vol. 55, No. 3, March 2008, pp 1453-1462.
- [15] R. Wain. I. Bush, M. Guest, M. Deegan, I. Kozin, C. Kitchen, "An overview of FPGAs and FPGA programming," http://www.cse.scitech.ac.uk/disco/publications/FPGA_overview.pdf



Ozlem Kilic graduated from The George Washington University (1996) with a D.Sc. in Electrical Engineering. She is presently a professor with the Catholic University of America. Before joining CUA, she worked at the U.S. Army Research Laboratories, Adelphi, MD and COMSAT Laboratories, Clarksburg, MD. Her research areas include computational electromagnetics, hardware accelerated programming for scientific computing, antennas and propagation, and radiation and scattering problems from random media.

A Simplified Model for Normal Mode Helical Antennas

Changyi Su, Haixin Ke, and Todd Hubing

Department of Electrical and Computer Engineering

Clemson University, SC 29634-3001, USA

csu@clemson.edu , hxkeucl@clemson.edu , hubing@clemson.edu

Abstract— Normal mode helical antennas are widely used for RFID and mobile communications applications due to their relatively small size and omni-directional radiation pattern. However, their highly curved geometry can make the design and analysis of helical antennas that are part of larger complex structures quite difficult. A simplified model is proposed that replaces the curved helix with straight wires and lumped elements. The simplified model can be used to reduce the complexity of full-wave models that include a helical antenna. It also can be used to estimate the performance of a helical antenna without full-wave modeling of the helical structure.

Index Terms— Helical Antennas, RFID.

I. INTRODUCTION

The helical antenna was introduced by John D. Kraus in 1946. Based on the far-field radiation pattern, a helical antenna operates in one of two principle modes: the normal mode with the maximum radiation perpendicular to the helix axis; or the axial mode with the maximum radiation in the direction of the axis [1]. The normal mode dominates when the diameter and axial length of the helix are much smaller than a wavelength. The radiation pattern of the normal mode helical antenna is omni-directional and generally similar to the pattern of a short dipole antenna. The self-resonant structure enables normal mode helical antennas to have radiation characteristics comparable to longer, straight-wire resonant dipole antennas [2]. Hence, normal mode helical antennas find many applications where the physical dimensions of the antennas are important, such as handsets [3], cellular phones [4]-[6] and RFID tags [7].

Unlike straight-wire dipole antennas, helical antennas are three-dimensional in structure and there is a lack of reliable formulas for their design

[8]. Most practical designs are the result of physical measurement trial-and-error, which is time-consuming and subject to errors introduced by the measurement facilities [4]. Therefore, numerical techniques are essential to helical antenna design and analysis [9], [10]. Helical antennas are mainly composed of curved surfaces and modeling these antennas using general purpose numerical tools requires mesh elements to be generated to fit the helical wire surfaces. This requires a large density of mesh elements and a great deal of computational resources. When modeling large systems that include a helical antenna, a significant portion of the computational effort may be devoted solely to the analysis of the helix, even when the helix is a small part of the total structure's volume.

In this paper, a simplified model is proposed to speed up the analysis of large structures containing helical antennas. In the simplified model, the helix is approximated by short straight wire segments connected by lumped elements representing the inductance of the helical turns. Theoretical calculations of the equivalent parameters are discussed. Nine different helix configurations are simulated using a general purpose full-wave modeling code to confirm the validity of the proposed model. The resonant frequency and input impedance of each configuration are examined. To further test the simplified model, two practical examples, an RFID antenna and a handset antenna, are also examined.

II. SIMPLIFIED MODEL

Fig. 1(a) shows the geometry of a helical dipole antenna. The helix is uniformly wound with a constant pitch, S . The radius of a helix can be uniform or tapered. In this paper, only uniform helices with constant radius, R , are considered. The helix's conductor is a wire of radius, a , with a

circular cross section. The antenna is fed at the midpoint of the coil winding. In this section, a simplified model of the helix is analyzed and analytical expressions for estimating the model parameters are established.

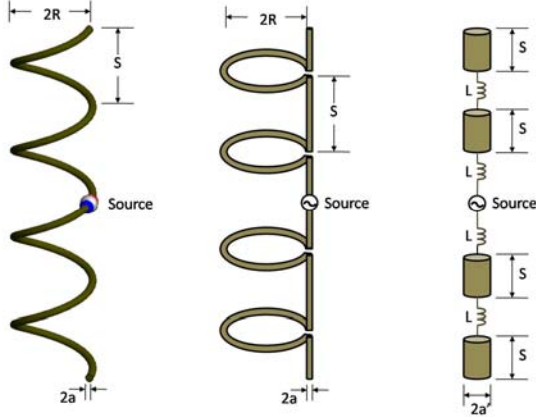


Fig. 1. (a) Helical antenna. (b) Wire-and-loop model. (c) Wire-and-inductor model.

It has been shown [1] that the helix can be approximated as a series of small loops and dipoles when the physical dimensions of the helix are much smaller than a wavelength. The equivalent wire-and-loop model for the helical antenna is shown in Fig. 1(b). The wire-and-loop model suggests that the axial ratio of the normal mode helical antenna can be expressed as

$$AR = \frac{E_\theta}{E_\phi} = \frac{2S\lambda}{(2\pi R)^2} = \frac{2S_\lambda}{C_\lambda^2} \quad (1)$$

where $S_\lambda = S/\lambda$ and $C_\lambda = C/\lambda$. C is the circumference of the loop.

Most practical normal-mode helical antennas have an axial ratio greater than 1. In these antennas, the radiated field from the loops is smaller than the radiated field from the straight wire segments. We can generally neglect the radiation from the loops without incurring significant error. For example, if we require 2 dB of accuracy, we can still neglect the field radiated by the loops as long as,

$$\frac{E_\phi + E_\theta}{E_\theta} < 2 \text{ dB}. \quad (2)$$

Equations (1) and (2) imply that we can neglect the radiation from the loops as long as,

$$AR > 4. \quad (3)$$

From (1), it is clear that different axial ratios can be achieved by proper selection of the helix

dimensions. For example, with $C_\lambda < 0.1$, $AR > 4$ is satisfied when $S_\lambda > 0.02$. The limits of the diameter and the pitch of the helix can be better expressed using the definition of pitch angle, e.g. in this case,

$$\tan(\alpha) = \frac{S}{C} > 0.2 \text{ or } \alpha > 11^\circ. \quad (4)$$

When the radiation from the loops can be neglected, they function like inductors. With this in mind, the wire-and-loop model can be further simplified by substituting inductors for the small loops as shown in Fig. 1(c). The proposed, simplified model consists of one straight wire segment per turn. Each segment is oriented vertically and has a length equal to the pitch of the helix. The segments are connected by lumped, inductive elements. The lumped elements do not increase the size of the mesh and do not significantly add to the computational complexity of the numerical analysis. Therefore, the simplified model requires considerably less computational resources to analyze than the original full-structure analysis.

In the original helix structure, the adjacent turns are coupled together via both mutual inductance and mutual capacitance. Since all the turns are coaxially oriented, some of the magnetic flux generated by one turn will pass through the neighboring turns. This part of flux induces a voltage that has the same polarity as the voltage drop caused by the self-inductance. In addition to the magnetic field coupling, electric field coupling also occurs between turns. The turn-to-turn capacitance provides an alternative current path that bypasses the loop and the straight wire. In the following sections, analytical expressions are derived that compensate for the mutual coupling that is missing in the simplified model.

A. Equivalent loop inductance

The parameters that need to be determined for the wire-and-inductor model in Fig. 1(c) include the equivalent inductance L of a single turn, and the equivalent radius a' of a short wire segment. The equivalent inductance includes the self-inductance L_{self} of one turn and the mutual inductance M coupled from its adjacent turns,

$$L = L_{self} + 2M. \quad (5)$$

The self inductance of a loop placed in free space is given by the double integral Neumann formula [13],

$$L_{self} = \frac{\mu_0}{4\pi} \oint \oint \frac{d\vec{l} \cdot d\vec{l}'}{r}. \quad (6)$$

Where μ_0 is the permeability of free space; and $d\vec{l}$ and $d\vec{l}'$ represent the differential elements separated by a distance, r . For a circular loop of wire, a closed form approximation for Eq. (6) is given by the following expression [13]:

$$L_{loop} = \mu_0 R \left[\ln\left(\frac{8R}{a}\right) - 2 \right] \quad (7)$$

where R is the loop radius and a is the wire radius.

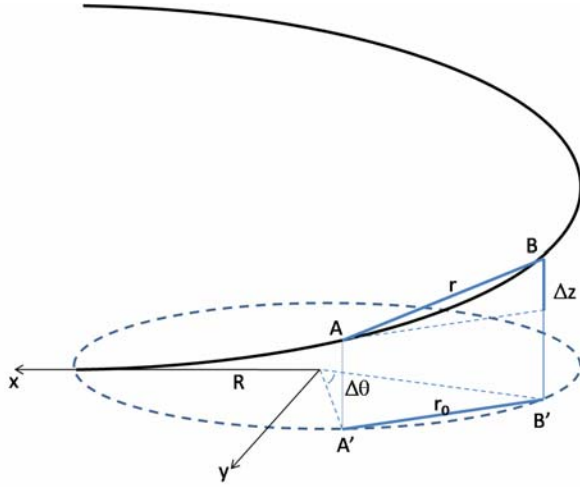


Fig. 2. Helical curve.

As shown in Fig. 2, the actual distance between any two points, A and B , on the helical curve is,

$$r = \sqrt{r_0^2 + \Delta z^2} \quad (8)$$

where r_0 is the distance between A' and B' obtained by projecting point A and B onto the x - y plane. Δz is the distance between points A and B in the z direction. When the pitch is small compared to the coil radius, the distance between A and B is approximately equal to that between A' and B' or $r \approx r_0$. Therefore, for a small pitch angle, Eq. (7) is a good approximation of the self inductance of a helix turn. However, as the pitch angle increases, Δz increases quickly. Consequently, the self inductance of a helix turn with a large pitch angle is much smaller than the inductance calculated by (7). Notice that for any point on the helix curve,

$$\frac{z}{R\theta} = \frac{S}{2\pi R}. \quad (9)$$

Therefore,

$$\Delta z = \frac{S}{2\pi R} R \Delta \theta. \quad (10)$$

Using the approximation,

$$r_0 \approx R \Delta \theta, \quad (11)$$

Eq. (8) becomes

$$r = r_0 \sqrt{\left(\frac{\Delta z}{r_0}\right)^2 + 1} \approx r_0 \sqrt{\left(\frac{S}{2\pi R}\right)^2 + 1}. \quad (12)$$

Substituting (12) into (6), the self inductance of a helix turn is given by,

$$\begin{aligned} L_{self} &= \frac{\mu_0}{4\pi} \oint \oint \frac{d\vec{l} \cdot d\vec{l}'}{r} \\ &\approx \frac{\mu_0}{4\pi} \oint \oint \frac{d\vec{l} \cdot d\vec{l}'}{r_0} \frac{1}{\sqrt{\left(\frac{S}{2\pi R}\right)^2 + 1}} \\ &= L_{loop} \frac{2\pi R}{\sqrt{(2\pi R)^2 + S^2}} \\ &= L_{loop} \cos(\alpha) \end{aligned} \quad (13)$$

The mutual inductance between two adjacent turns can be approximated by the mutual inductance between two coaxially oriented circular loops of radius R , separated by a distance S [13].

$$M = \frac{\pi \mu_0 R^4}{2(R^2 + S^2)^{\frac{3}{2}}}. \quad (14)$$

B. Equivalent wire radius

The capacitance of a wire with length l and radius a placed in free space is given by [14],

$$C_w = \frac{\pi \epsilon_0 l}{2 \ln\left(\frac{l}{a}\right)} \quad (15)$$

where ϵ_0 is the permittivity of free space. In Fig. 1(c), one helix turn is replaced by a short wire segment with a length equal to the helix pitch. The wire length is much shorter than the turn length; therefore, the total wire capacitance is reduced. To maintain the correct capacitance, the radius of the straight wire segments must be increased. The capacitance of the thicker wire should equal the capacitance of a helix turn. Therefore, the equivalent radius, a' , is obtained using the following expression:

$$\frac{S}{\ln\left(\frac{S}{a'}\right)} = \frac{l_{tot}}{\ln\left(\frac{l_{tot}}{a}\right)} \quad (16)$$

where $l_{tot} = \sqrt{(2\pi R)^2 + S^2}$.

The term on the left-hand side of (16) is the capacitance of a wire segment in the simplified model. The term on the right-hand side of (16) is the capacitance of a turn in the original helix. Eq. (16) is based on an assumption that the mutual capacitance between turns is negligible compared to the self capacitance of the wire. This is a reasonable assumption when the pitch angle satisfies the condition in Eq. (4).

III. VALIDATION OF THE SIMPLIFIED MODEL

In order to validate the simplified model described in the previous sections, the input impedances and the radiation patterns of helical antennas and the corresponding simplified models were calculated using a full-wave numerical modeling tool [17]. Since a normal mode helical antenna is generally designed to operate at its

resonant frequency, the performance of the simplified model near resonance is important. The evaluation was done by computing the relative differences in the calculated input resistance and resonant frequency. The error in the input resistance is defined as the ratio of the resistance difference over R_0 , the input resistance of the helical antenna at its resonant frequency f_0 . The error in the resonant frequency of the helical antenna is defined as the difference between the resonant frequency of the simplified antenna, f_1 , and the full helix, f_0 , divided by f_0 . Expressed as a percentage, the equations for these errors are indicated below:

$$Error(Re) = \frac{|R_0 - R|}{R_0} \times 100\% \quad (17)$$

$$Error(f) = \frac{|f_0 - f_1|}{f_0} \times 100\%. \quad (18)$$

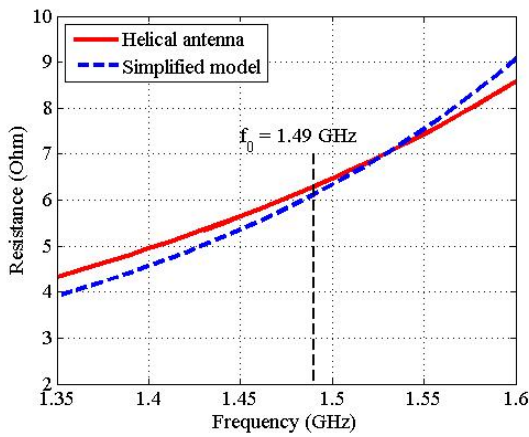
The geometrical parameters of the antennas evaluated are given in Table 1. The antennas are grouped in three sets. Within each set, one parameter was varied.

Table 1: Geometrical Parameters of Helical Antennas.

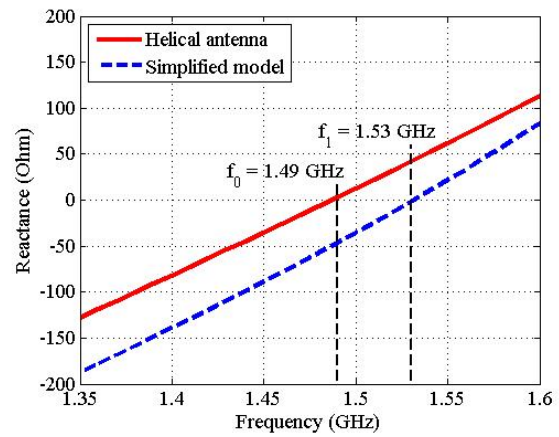
No	Geometry	Resonant frequency
Different wire radius		
1	$N = 10, R = 1 \text{ mm}, S = 1.68 \text{ mm}, \alpha = 15^\circ, a = 0.01 \text{ mm}$	2.89 GHz
2	$N = 10, R = 1 \text{ mm}, S = 1.68 \text{ mm}, \alpha = 15^\circ, a = 0.02 \text{ mm}$	2.97 GHz
3	$N = 10, R = 1 \text{ mm}, S = 1.68 \text{ mm}, \alpha = 15^\circ, a = 0.04 \text{ mm}$	3.08 GHz
Different pitch angle		
4	$N = 10, R = 2 \text{ mm}, S = 2.67 \text{ mm}, \alpha = 12^\circ, a = 0.02 \text{ mm}$	1.47 GHz
5	$N = 10, R = 2 \text{ mm}, S = 4.57 \text{ mm}, \alpha = 20^\circ, a = 0.02 \text{ mm}$	1.38 GHz
6	$N = 10, R = 2 \text{ mm}, S = 10.5 \text{ mm}, \alpha = 40^\circ, a = 0.02 \text{ mm}$	1.00 GHz
Different number of turns		
7	$N = 10, R = 2 \text{ mm}, S = 4.57 \text{ mm}, \alpha = 20^\circ, a = 0.02 \text{ mm}$	1.38 GHz
8	$N = 20, R = 2 \text{ mm}, S = 4.57 \text{ mm}, \alpha = 20^\circ, a = 0.02 \text{ mm}$	741 MHz
9	$N = 40, R = 2 \text{ mm}, S = 4.57 \text{ mm}, \alpha = 20^\circ, a = 0.02 \text{ mm}$	395 MHz

Table 2: Equivalent Parameters of Simplified Models.

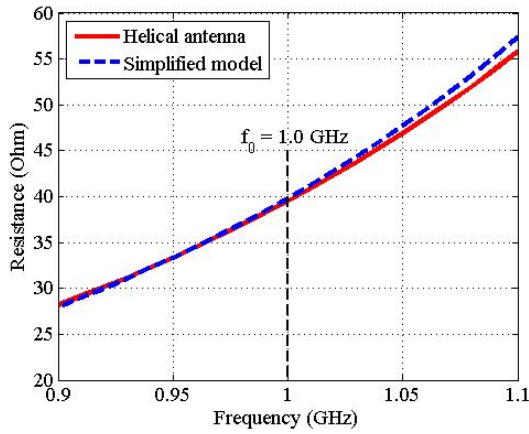
No	Equivalent parameters	Error (Re) (%)	Error (f) (%)
1	$a' = 31.5a, L = 6.21 \text{ nH}$	2.2	1.3
2	$a' = 18.9a, L = 5.35 \text{ nH}$	1.5	1.3
3	$a' = 11.3a, L = 4.51 \text{ nH}$	0.7	1.6
4	$a' = 34.8a, L = 13.2 \text{ nH}$	3.2	2.7
5	$a' = 24.7a, L = 11.5 \text{ nH}$	4.0	0.1
6	$a' = 7.11a, L = 9.07 \text{ nH}$	0.6	1.0
7	$a' = 24.7a, L = 11.5 \text{ nH}$	4.0	0.1
8	$a' = 24.7a, L = 11.5 \text{ nH}$	1.4	1.7
9	$a' = 24.7a, L = 11.5 \text{ nH}$	3.2	2.2



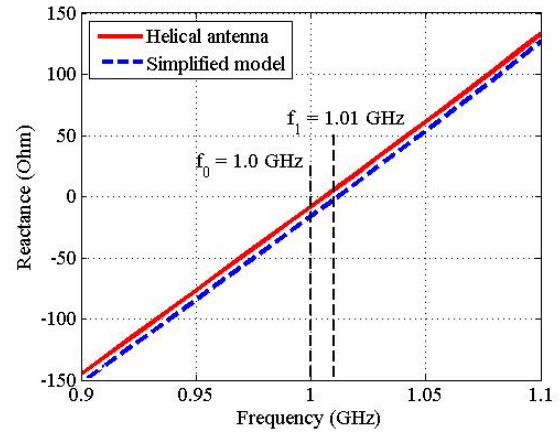
(a) Case 4: Input resistance.



(b) Case 4: Input reactance.



(c) Case 6: Input reactance.



(d) Case 6: Input reactance.

Fig. 3. Input impedance for Cases 4 and 6.

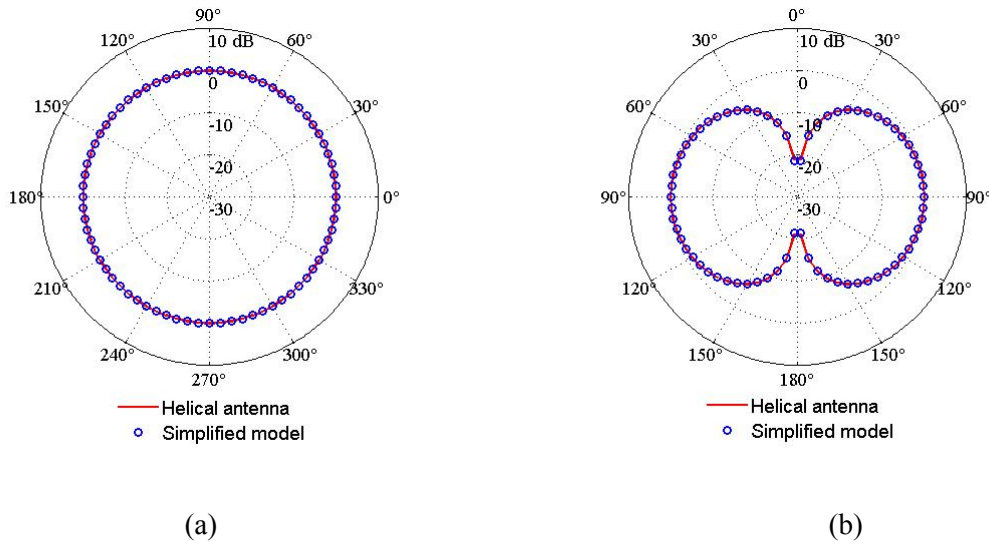


Fig. 4. Radiation patterns for Case 4: (a) Azimuth plane field pattern (b) Elevation plane field pattern.

Table 3: CPU-time and memory usage.

No	CPU-time (Second)		Memory-usage (MByte)	
	Original model	Simplified model	Original model	Simplified model
1	4.28	0.4	14.8	0.54
2	4.23	0.65	14.8	0.75
3	4.95	0.64	16.9	0.96
4	20.8	0.46	65.6	0.72
5	24.9	0.46	74.4	0.82
6	44.3	2.37	115.5	2.8
7	24.9	0.43	74.4	0.82
8	146.4	1.51	311.3	2.67
9	506	5.42	890	9.54

The relative errors in the input resistance and resonant frequency for each case are listed in Table 2. The input resistances at the resonant frequency of the simplified model are in reasonable agreement (within 5%) with values calculated for the full helix in all cases. The good agreement suggests that the analytical formulas (13) - (16) are sufficiently accurate near resonance for the helical antenna geometries evaluated. Table 3 shows the computation time and the amount of memory per frequency required to analyze each original helical antenna and its simplified model. The simplified model significantly reduces both the CPU-time and the memory usage.

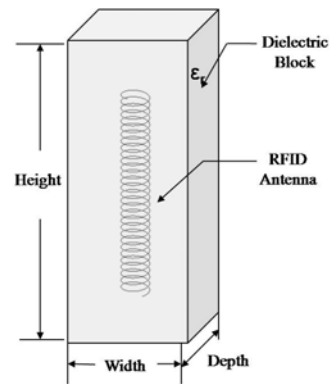


Fig. 5. An RFID antenna embedded in a dielectric block.

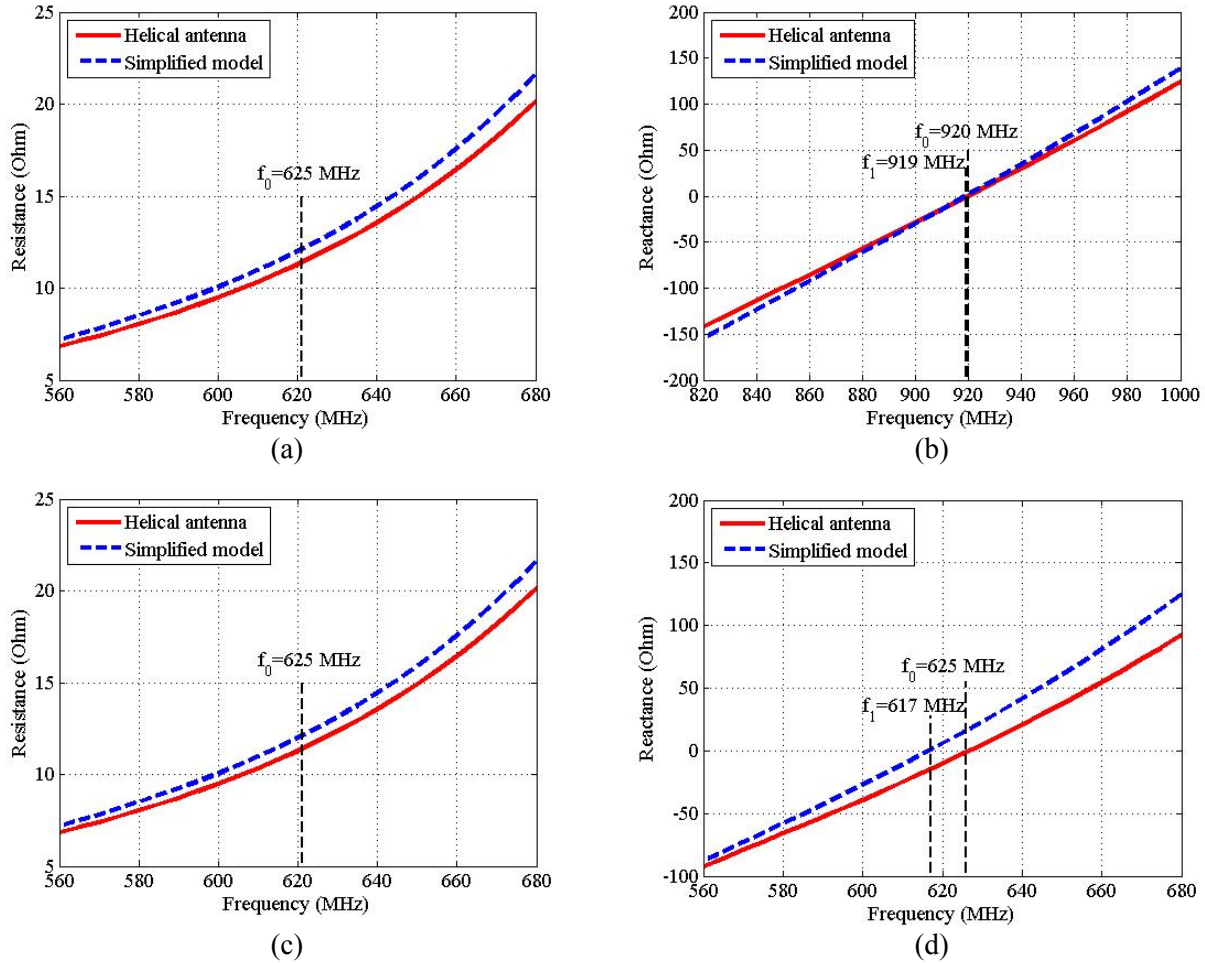


Fig. 6. Input impedance of the RFID antenna and its simplified model: (a) Input resistance in air (b) Input reactance in air (c) Input resistance in dielectric (d) Input reactance in dielectric.

One application of the simplified model is RFID antennas, which are widely used for identification and tracking of objects using radio waves. Recently, tire makers have begun embedding RFID tags in some of their tires to enable them to be tracked electronically. These tags often employ helical antennas embedded in a dielectric material as illustrated in Fig. 5. In this example, the antenna is designed to resonate at around 920 MHz. The parameters of the helix are: $N = 106$ turns, $R = 0.5$ mm, $S = 0.833$ mm, $a = 0.09$ mm. The dimensions of the dielectric block are $97 \times 11 \times 11$ mm. The relative permittivity of the dielectric is 4.0.

The input impedance of both the RFID antenna and the simplified model are calculated for the antenna in air and the antenna in the dielectric block (Fig. 6). The difference between the helix and simplified model calculations of the

input impedance is less than 5% for both the RFID antenna in air and in the dielectric block.

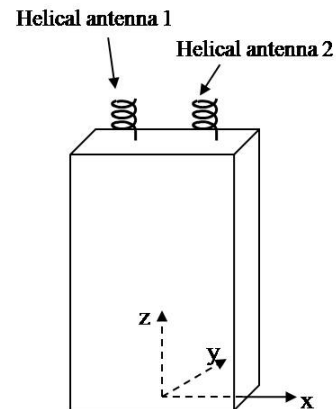


Fig. 7. Mobile handset and coordinate system.

In order to further test the proposed model, a practical helical antenna design [3] for mobile handsets was also simulated. In this design, two helical antennas are mounted on top of a metal box ($10 \times 4.8 \times 1.67$ mm) and separated by 3.125 cm (Fig. 7). Antenna 1 is excited and Antenna 2 is connected to a $50\text{-}\Omega$ load. The helical antenna array is tuned to resonate at about 1.65 GHz. The antenna parameters are: $N = 2.6$ turns, $S = 9.94$ mm, $R = 2.1$ mm, $a = 0.28$ mm. The simplified model requires an integer number of turns. Therefore, the number of turns was set to 3 in this simulation. The simulation results are shown in

Figs. 8 and 9. The input resistance of the simplified model is close to that of the helical antenna near the resonant frequency. The error in the resonant frequency is only 1%. The radiation pattern predicted by the simplified model is identical to that of the helical antenna in both azimuth and elevation planes. The good agreement demonstrates that the proposed model is not only suitable for dipole-helical antennas, but it can be also applied to monopole-helical antennas.

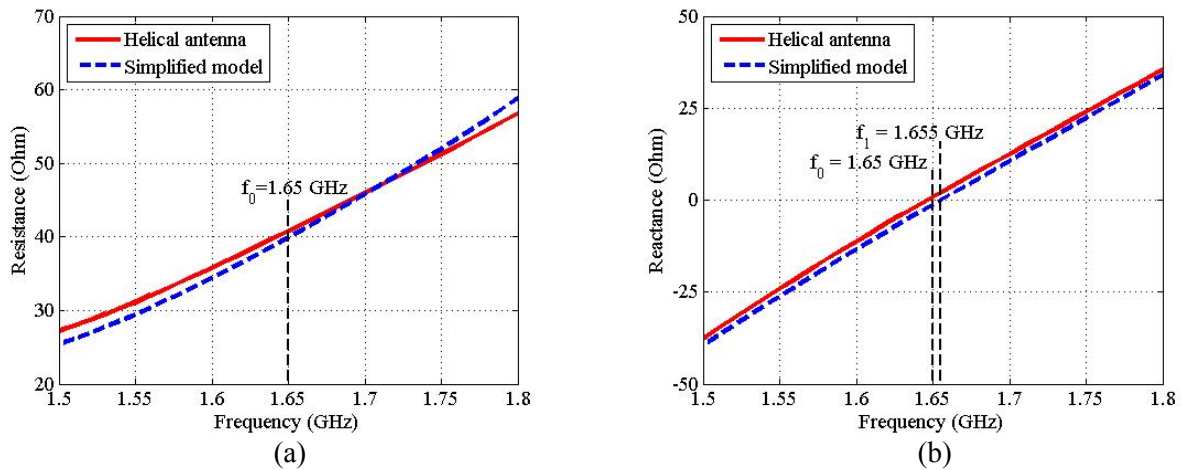


Fig. 8. Input impedance of the helical antenna of the handset: (a) Input resistance (b) Input reactance.

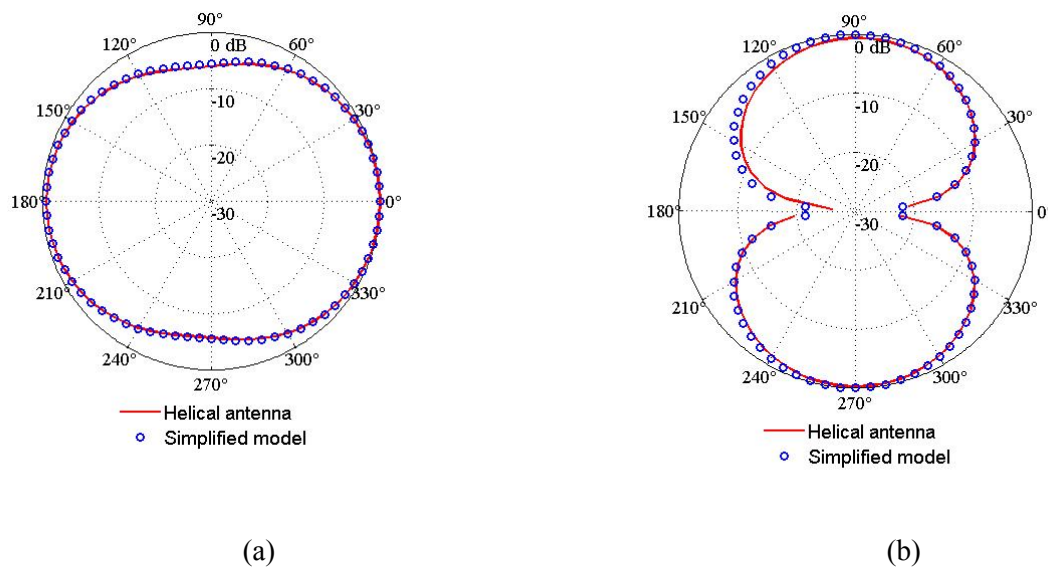


Fig. 9. Radiation patterns for the handset helical antenna in the Azimuth plane: (a) E_θ (b) E_ϕ .

IV. CONCLUSION

A simplified model for helical antennas has been proposed. In the model, the highly curved structure of the helix is replaced with a straight-wire and inductor structure. The number of elements required to model the helix is significantly reduced; and therefore, analysis of the simplified model uses much less computational resources than analysis of the full helix.

REFERENCES

- [1] J. D. Kraus, *Antennas*, 2nd ed., McGraw-Hill, 1988.
- [2] Y. Hiroi, K. Fujimoto, "Practical usefulness of normal mode helical antenna," *IEEE AP-S Int. Symp.*, pp. 238-241, 1976.
- [3] H. T. Hui, "Practical dual-helical antenna array for diversity/MIMO receiving antennas on mobile handsets," *IEE Proceeding, Microwaves, Antennas and Propagation*, vol. 152, no. 5, pp. 367-372 2005.
- [4] M. M. Faiz and P. F. Wahid, "Microstrip line matched normal mode helical antenna for cellular communication," *Southeastcon'98, Proceedings, IEEE*, pp. 182-185.
- [5] H. Morishita, Y. Kim, H. Furuuchi, K. Sugita, Z. Tanaka and K. Fujimoto, "Small balance-fed helical dipole antenna system for handset," *51st Vehicular Technology Conference (VTC) Proceedings*, Tokyo, vol. 2, pp.1377 – 1380, May 15-18, 2000.
- [6] K. Noguchi, S. Betsudan, T. Katagi, and M. Mizusawa, "A compact broad-band helical antenna with two-wire helix," *IEEE Trans. Antennas Propagat.*, vol. 51, no. 9, pp. 2176-2181, 2003.
- [7] Y. Yamada, W. G. Hong, W. H. Jung and N. Michishita, "High gain design of a very small normal mode helical antenna for RFID tags," *IEEE Region 10 Conference*, pp. 1-4, 2007.
- [8] A.R. Djordjevic, A.G. Zajic, M.M. Ilic, and G.L. Stuber, "Optimization of helical antennas," *IEEE Trans. Antennas Propagat.*, vol. 48, pp. 107-105, 2007.
- [9] G. Lazzi, and O. P. Gandhi, "On modeling and personal dosimetry of cellular telephone helical antennas with the FDTD codes," *IEEE Trans. Antennas Propagat.*, vol. 46, pp. 525-530, 1998.
- [10] E. D. Caswell, "Analysis of a helical antenna using a moment method approach with curved basis and testing functions," M. Sc. Thesis, Virginia Polytechnic Institute, 1998.
- [11] C. A. Balanis, *Antenna Theory – Analysis and Design*, 3rd ed., John Wiley & Sons Inc., 2005.

- [12] S. Ramo, J. R. Whinnery and T. V. Duzer, *Fields and Waves in Communication Electronics*, New York, J. Wiley, 1965.
- [13] S. A. Schelkunoff and H. T. Friis, *Antennas: Theory and Practice*, John Wiley & Sons Inc., 1952.
- [14] F. M. Tesche, et al., *EMC Analysis Methods and Computational Models*, Wiley-IEEE, 1997.
- [15] A. J. Palermo, "Distributed capacity of single layer coils," *Proc. IRE*, vol. 22, pp.897-903, 1934.
- [16] G. H. Brown and O. M. Woodward, Jr., "Experimentally determined impedance characteristics of cylindrical antennas," *Proc. IRE*, vol. 33, pp. 257-262, 1945.
- [17] FEKO, <http://www.feko.info>.



Changyi Su received her B.Eng. degree from Xian University of Technology, Xian, China and her M. Eng. degree from Nanyang Technological University, Singapore in 1993 and 2001, respectively. She is working toward the Ph.D. degree at Clemson University, Clemson, SC. Her research interests include electromagnetic modeling, and computational electromagnetics.



Haixin Ke received the B.S. and M.S. degrees from Tsinghua University, Beijing, China, in 1998 and 2001, respectively, and the Ph.D. degree from the University of Missouri, Rolla, in 2006, all in electrical engineering. From 2006 to 2009, he worked as a Postdoctoral Researcher at Clemson University, Clemson, SC. He is currently a Postdoctoral Research Associate at Washington University in St. Louis, MO. His research interests include computational electromagnetics, electromagnetic compatibility, and microwave/optical imaging.



Todd H. Hubing received a B.S. degree from MIT in 1980, an M.S. degree from Purdue in 1982, and a Ph.D. degree from North Carolina State in 1988, all in electrical engineering. From 1982 to 1989, he worked for IBM in Research Triangle Park, NC. In 1989, he joined the faculty at the University of Missouri-Rolla; and in 2006, he moved to Clemson University, where he is currently the Michelin Professor of Vehicle Electronics. Prof. Hubing is a member of the Board of Directors of the IEEE EMC Society and a past-president of that society. He is a Fellow of the IEEE and a Fellow of the Applied Computational Electromagnetics Society.

Antenna Developments for Military Applications

Amir I. Zaghoul^{1,2}, Steven J. Weiss¹, W. Keefe Coburn¹

¹ U.S. Army Research Laboratory, Adelphi, MD 20783, USA
amir.zaghoul@us.army.mil, steven.weiss@us.army.mil, william.coburn@us.army.mil

² Department of Electrical & Computer Engineering
Virginia Polytechnic Institute and State University, VA 22043, USA
amirz@vt.edu

(Invited Paper)

Abstract — A review of current, past and projected activities in antenna development indicates a broad spectrum of requirements, and subsequently a variety of innovations to meet these requirements for military radar and communications systems. Designing the antennas in the operating environment, known as in-situ design, is an important factor in guaranteeing the successful operation of the antenna in the field. This paper presents the basic blocks in antenna development, followed by examples of some antennas developed at the Army Research Laboratory for military systems and applications. These include Rotman lenses as beam formers for electronically scanning arrays; phased arrays using MEMS phase shifters at 30 GHz; a 76-GHz narrow beam, low-sidelobe antenna for collision avoidance radar; and other specialized antennas. Of special interest is an effort on developing and using metamaterials in antenna designs, where practical realizations of such materials have the potential of improving the performance and reducing the size of antennas.

Index Terms — Antenna Modeling, Army, Military, In-Situ.

I. INTRODUCTION

Antenna requirements for military applications include low profile, high efficiency, wide frequency band, highly integrated and conformability to the host platform. The low profile and conformability stem from the desire to blend the antenna into its surroundings to avoid easy visible detection and identification. These applications often require novel antenna solutions.

In general, the more complex the antenna, the more it can be effected by the platform and

operational environment. This is not always addressed by designers, even though it is the in-situ antenna performance that will determine the system performance. The earlier in the acquisition process that the in-situ performance can be verified the more savings can be realized.

Another important parameter in the antenna design is the choice of materials that meet structural, electronic, and electromagnetic requirements. Material issues are paramount in integration, packaging, interference, and performance parameters such as efficiency and bandwidth. Material selection also plays important roles in antenna appearance and identification, as well as its in-situ performance.

In the following sections we go through the elements of the antenna development, discuss the roles of government laboratories, industry and academia in such developments, and present some examples of recent and on-going research.

II. ELEMENTS OF ANTENNA DEVELOPMENT

A successful antenna development is a collaborative effort between the customer, who sets the requirements, in this case Government laboratories, academia or universities, and industry. The sequence of development from concept to fielding is shown in Figure 1, along with the main areas that constitute the development. The requirements for the specific applications, the modeling in the environment, and the field testing of the antenna occur at different stages of the development and are specific to the Army, Navy, or Air Force laboratory that is involved. The last stage of production is specific to the industry.

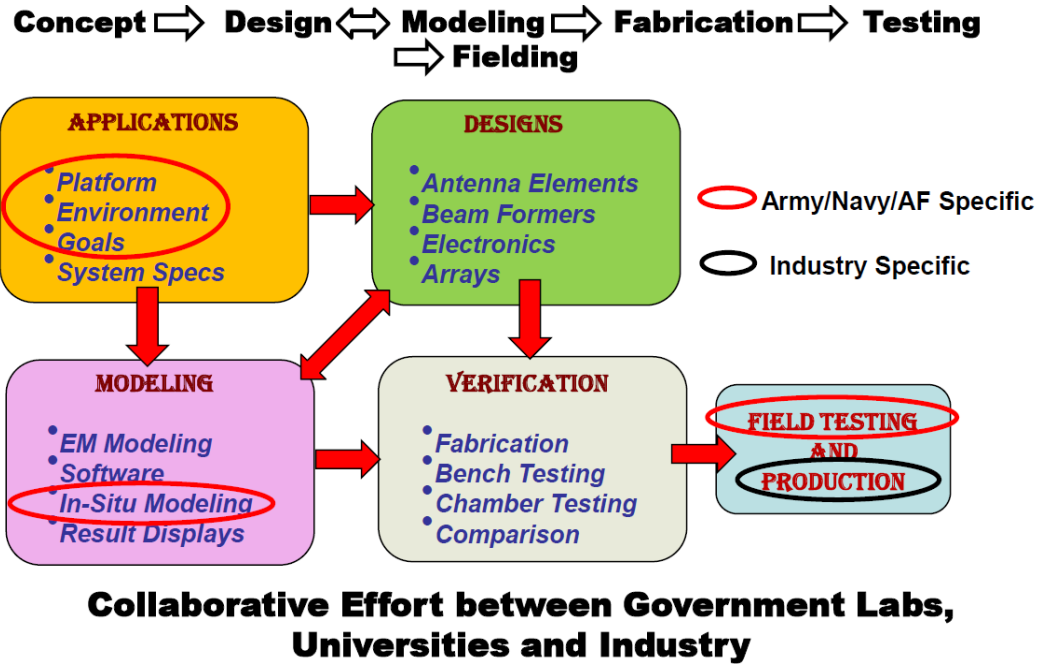


Fig. 1. Components of antenna development for military applications.

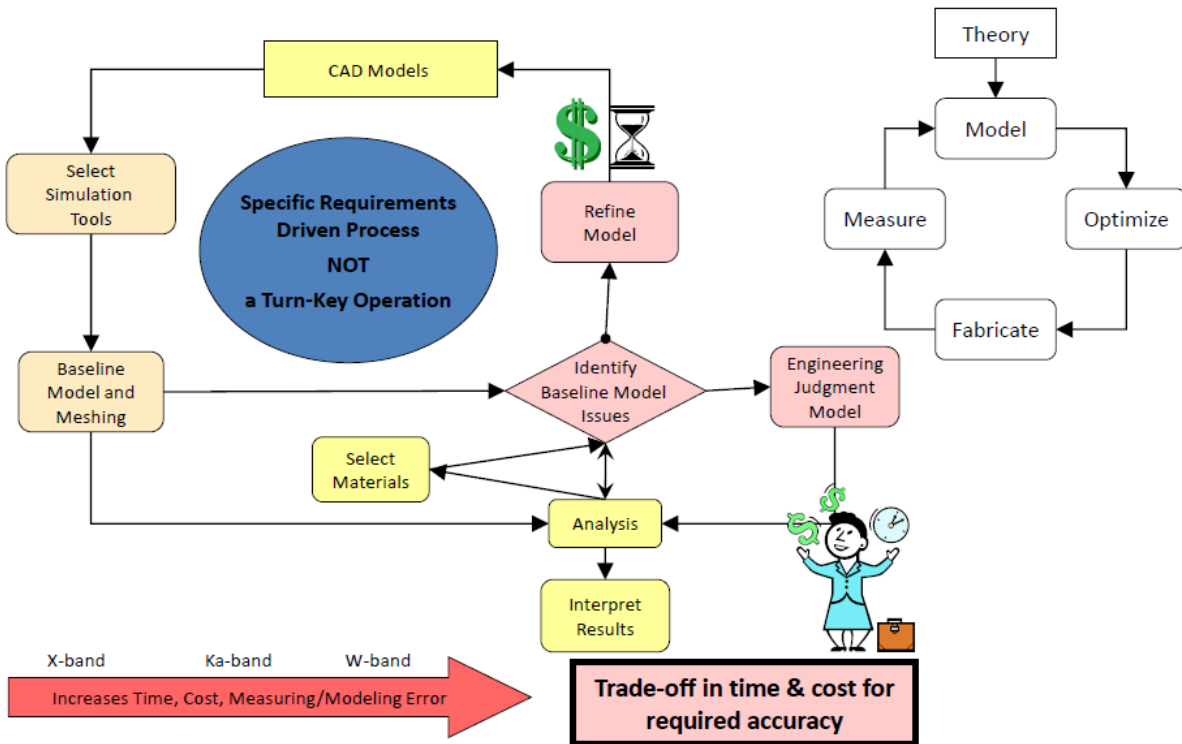


Fig. 2. Modeling flow-chart for electromagnetic simulation.

Modeling has become a central and essential part of the antenna development. Commercial software packages for electromagnetic modeling have seen significant advancements over the last four decades. They continue to be improved as new designs and new materials call for new modeling paradigms. High performance computing (HPC) tools have made it possible to model complex structures over broad frequency bands in ways that were not possible a few decades ago. However, expert users are always required and expected to make full usage of the available modeling and computational tools. Engineering judgment is often required to meet time and cost constraints, as modeling is a trade-off in time and cost for the required accuracy. A modeling flow chart that shows the different steps in the electromagnetic modeling is shown in Figure 2.

III. IN-SITU ANTENNA DESIGN

A major objective for military applications is to develop and evaluate electromagnetic models of in-situ antenna designs in operational environments to support the design and analysis of multifunction radar and communication systems. "Bolt-on" antenna solutions often have reduced performance whereas vehicle integrated designs can dramatically improve performance and avoid costly redesign and increased Test and Evaluation (T&E) costs. The earlier in the acquisition process that the in-situ performance can be verified the more savings can be realized. In-situ antenna modeling refers not just to the sensor platform but also its environment such as urban terrain and the presence of a ground plane. Army applications often require novel antenna solutions but in general the more complex the antenna the more it can be effected by the operational environment. The highly integrated antenna designs will emphasize low cost, lightweight approaches with optimum performance on the next generation RF sensor platforms. This is often not addressed by industry even though it is the in-situ antenna performance that will determine the system capability.

Army Research Laboratory (ARL) has developed a significant measurement and simulation-based infrastructure for modeling antennas and antenna platforms. Antennas are critical elements for all radar and communication

systems. Therefore, it is necessary to fully characterize and understand antenna performance in the presence of the platform to assess system performance. Poorly designed antennas can lead to electromagnetic interference (with other systems on the platform), decreased range and underutilization of bandwidth. In addition, poorly integrated antennas can adversely affect the aerodynamic and structural performance for the case of airborne platforms. This can lead to costly overruns for re-designs. ARL is using simulation-based design techniques (with spot measurements for validation) to model the antenna and platform over the complete design trade space in order to arrive at the optimal solution the first time.

ARL uses a combination of in-house developed and contractor-developed software for modeling antennas. The primary production codes in use at ARL include commercial software for antenna design and analysis such as FEKO (<http://www.feko.info>), Ansoft High Frequency Structure Simulator (<http://www.ansoft.com>), EMPiCASSO (<http://www.emagware.com>), XFDTD (<http://www.remcom.com>) and the General Electromagnetic Model for the Analysis of Complex Systems (GEMACS) (<http://www.gemacs.com>). These are general purpose computational electromagnetic (CEM) codes but are often specialized to certain antenna types such a planar or guided wave structures. ARL has on-going efforts with code developers to incorporate specialized features into such tools. Examples are research contracts with Remcom and Ansoft to apply specialized methods for modeling electrically large devices with application to the design of Rotman Lenses for beam forming networks. Such codes along with in-house developed software allow the design and evaluation of complex antenna arrays for military applications.

In many cases, antenna design and analysis is platform specific where the antenna modeling must be done in-situ to incorporate the influence of the antenna installation on antenna performance. Hybrid techniques such as incorporated in FEKO and GEMACS enable the Department of Defense (DoD) laboratories to design – from first principle electromagnetics – in-situ wideband multi-functional antennas for a wide range of DoD activities including communication, acquisition, target identification, surveillance, and

electronic attack. These codes have a large user base and have been extensively validated for a wide range of radiation and scattering applications. Current DoD requirements for large arrays and apertures are too complex (geometrically and materially) to be handled by traditional analytical methods, such as element-pattern times array-factor. What is required today is sophisticated antenna software that uses exact physics to accurately predict near field quantities like the currents flowing on the antenna and the fields in the antenna's housing. DoD requirements have expanded to include antenna arrays that are very large in terms of free-space wavelengths so that fast methods and parallel implementations are required.

FEKO is an example of a state-of-the-art PC-based code that incorporates fast methods and hybrid techniques to solve electrically large problems in practical times. GEMACS can use a combination of exact and asymptotic methods to solve electrically large problems. This parallel code is available on the DoD Supercomputing Resource Centers (www.hpcmo.hpc.mil) and shows good scalability to a large number of processors. The types of computations needed to obtain antenna performance data lend themselves to a natural parallelism – that is, angles and frequencies of interest can be spread across many processors in a very efficient manner. Thus a combination of PC software and HPC codes are often used to develop antenna designs and efficiently evaluate those designs as installed on air, land or sea-based military platforms. Military sensor platforms on the modern battlefield range from ground/air vehicles to munitions and even the individual Warfighter. Using in-situ modeling early in the acquisition process can ensure that the antenna meets requirements in the operational environment and lead to cost/schedule savings especially during T&E.

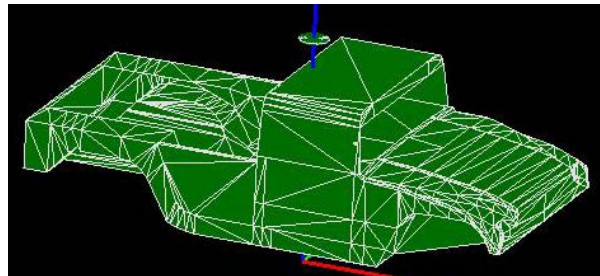
A generic example of in-situ antenna analysis using GEMACS is shown in Figure 3 for a roof mounted spiral antenna on a HMMWV (M998) at 750 MHz. The EM model is shown in Figure 3(a) where the antenna support and radome structure are not included and the ground plane is not shown. GEMACS provides a hybrid solution for these type problems with the antenna modeled using method of moments (MoM) while the vehicle is modeled using the geometrical theory of

diffraction (GTD). The ground plane is modeled as a large GTD plate except that edge and corner diffractions are not included. A typical radiation pattern comparison is shown in Figure 3(b) when including first order reflections only (blue), reflection and edge diffraction (black) and then with the ground plane only (yellow). The radiation pattern at this height over ground (yellow) would be severely distorted if installed as shown on the host vehicle. In many cases the edge diffraction contribution to the pattern perturbations are negligible and can often be neglected to reduce the simulation time. Multipath/blockage effects are good examples of where the in-situ environment includes nearby structures and ground. In this example, scattering from the host vehicle significantly perturbs the radiation pattern with reduced gain and a null in the overhead direction.

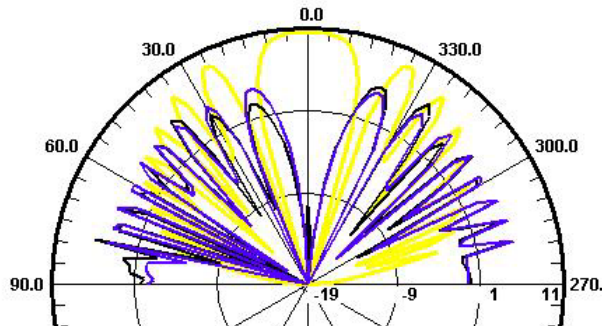
The Army is using more unmanned aerial vehicles (UAVs) as sensor platforms where the ground plane may not be important aspect of the operational environment. Another example of in-situ antenna modeling is direction finding antennas on a generic UAV platform where a reliable in-situ (and platform specific) knowledge of the radiation pattern is required for algorithm calibration. The FEKO model and calculated radiation pattern for monocone antennas at 300 MHz are shown in Figure 4. Compared to a wing only model the UAV platform introduces additional perturbations primarily in the back lobes (aft direction). In this example the two antennas are not exactly symmetrically located on the UAV wing and this small difference can be seen in the pattern asymmetries. As can be seen the in-situ pattern would be required to analyze system performance and an infinite ground plane or wing only model is not sufficient.

Composite construction requires verification of CEM tools and approximations through measurements on the actual airframe materials. An example is the UAV wing with bent monopole antenna shown in Figure 5(a) when covered with metal foil. The difference in radiation pattern for the antenna on metal versus the graphite skin wing is small (<2.5 dB) as can be seen in Figure 5(b) for the elevation plane. The metal model of the UAV used in the *FEKO* simulations should be a reasonable representation of this type composite [1]. With increasing frequency even small platforms will require more computational

resources and/or the use of hybrid or asymptotic methods. But to use these methods accurately, users must have significant experience in their applications and limitations. In many cases engineering judgment is required to meet project objectives.



(a)

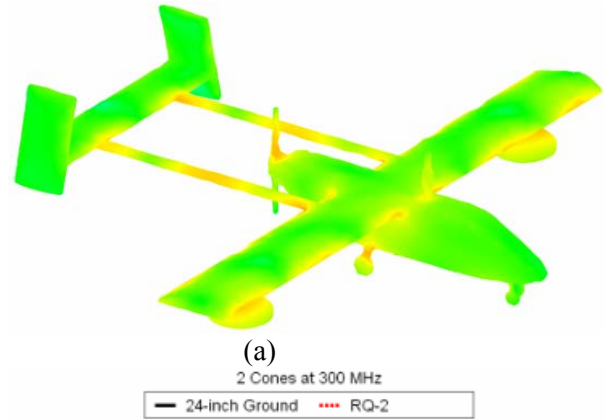


(b)

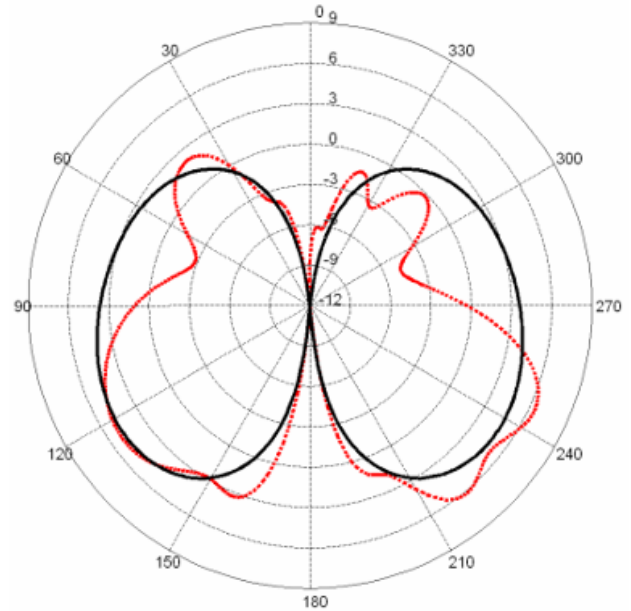
Fig. 3. Spiral antenna (a) on M998 over large ground plane, and (b) radiation pattern with reflections only (blue), reflection and diffraction (black) and without vehicle (yellow).

Antenna solutions for munitions could be another case where the ground is not an important part of the operational environment. Concepts for null steering using an endfire antenna array have been investigated for this application. An example is shown in Figure 6 for a four-element aperture-fed patch array with 1:2:2:1 amplitude weights. The array was designed with a 2.5-D model (EMPiCASSO) but the 3-D model (FEKO) shows the true effect of a finite size ground plane. A simple wedge model is used to approximate a nose cone installation where the radome is not included. Two arrays are combined to produce a boresight null and this model is used to further investigate pattern perturbations. For instance, including a metal backing plate reduces but does not eliminate the back lobes [2]. A full 3-D model of the in-situ

antenna is required to fully evaluate and optimize performance to meet system requirements.



(a)



(b)

Fig. 4. Generic UAV example (a) with monocone antennas and (b) azimuthal pattern perturbation at 300 MHz compared to the wing only result.

The Warfighter can be one of the most challenging platforms for high performance antennas. Operation over realistic ground is a unique Army requirement. Free space designs are typically not appropriate for Army applications and could require redesign leading to cost and schedule impacts. A generic body model is used with parameters of typical skin to demonstrate in-situ effects for a lapel mounted RFID antenna as shown in Figure 7. Ground does not perturb the antenna input impedance but leads to a split main

beam pattern. Close proximity to the body changes the antenna input impedance to the point that redesign would be required. Realized gain is reduced ~ 3 dB and becomes more frequency dependent. Placement further from the body or antenna redesign is required to compensate for these loading effects. Optimum performance requires an in-situ design that accounts for the operational environment which includes operation in different body positions over realistic terrain or in vehicles.

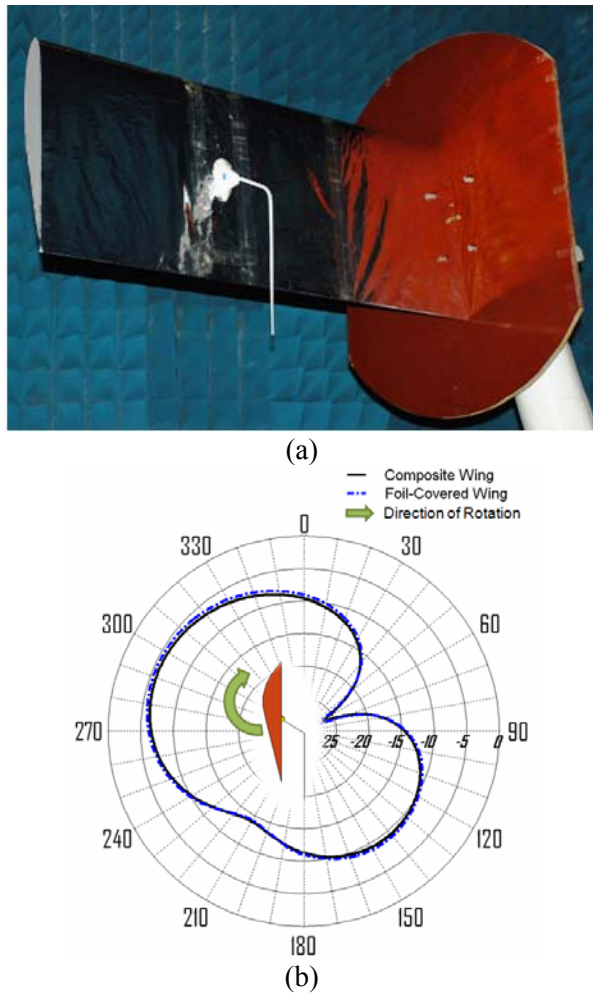


Fig. 5. UAV wing with bent monopole antenna example (a) when covered with metal foil and (b) azimuthal pattern perturbation at 144 MHz compared to composite wing.

To summarize, we showed some generic antenna modeling examples and how performance can be impacted by the operational environment such as the presence of a lossy ground plane. We

highlighted some applications of in-situ antenna design/analysis and how modeling might be used to evaluate and/or optimize the antenna performance in its operational environment. For electrically large problems HPC resources are required and ARL has access to some of the latest HPC platforms and CEM tools. The next generation of CEM software developed by the DoD will be focused on useable, accurate and efficient tools for in-situ antenna design in order to meet the every increasing computational challenges of advanced antenna technologies.

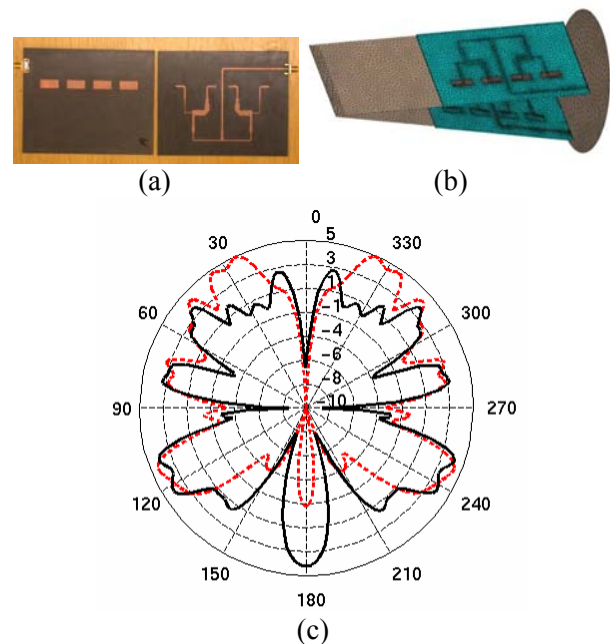


Fig. 6. FEKO example for (a) an endfire array, (b) the in-situ model and (c) the azimuthal pattern perturbation with (red) and without (black) a metal backing plate.

IV. DEVELOPMENT EXAMPLES

Rotman Lens:

Since the inception of the Rotman Lens in 1963 [3], there has been considerable interest in using such beamformers in array applications. The spatial beamforming aspect of such lenses has historically been of interest to the Army as a scanning mechanism for small arrays in a multifunctional environment [4 - 6]. Recently, the Rotman lens has become appealing as a beamformer for terrestrial communication applications [7 - 8]. In this section, we present an

example of such a lens from inception to first prototype.

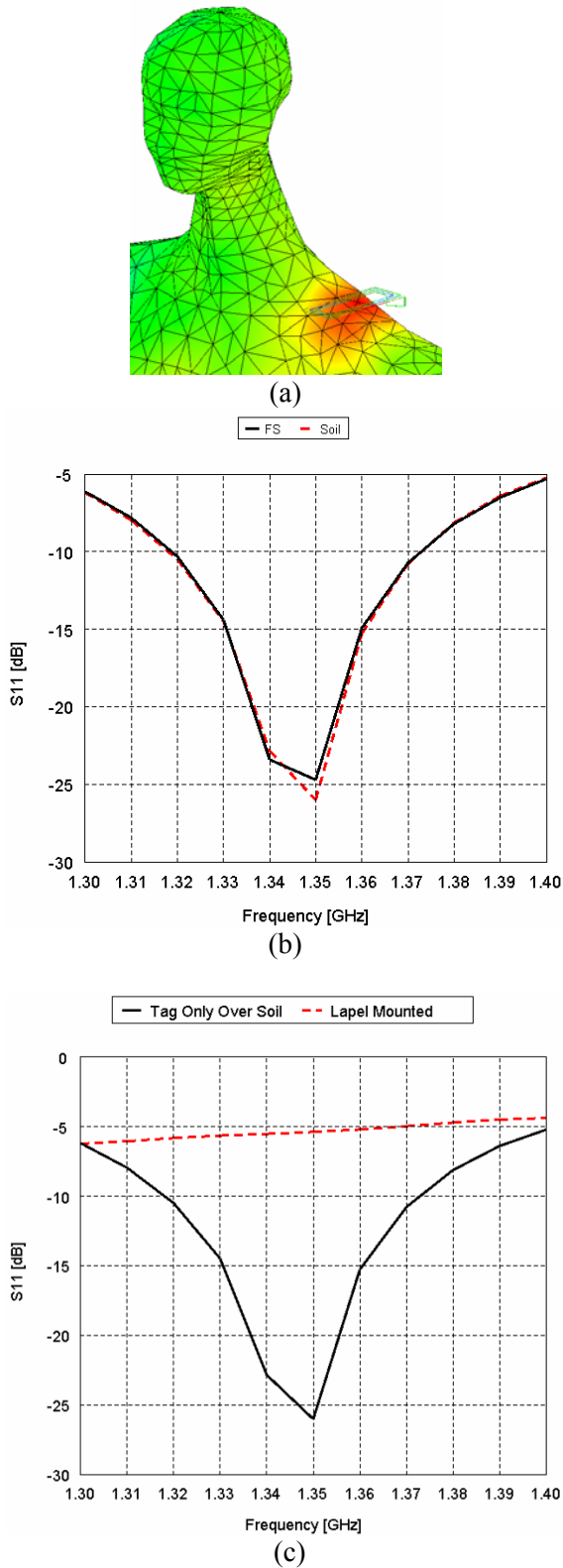


Fig. 7. Body worn antenna (a) in-situ model, (b) S_{11} when in free space (black) compared to soil (red) and (c) over soil with (red) and without (black) the body.

Through an Army sponsored SBIR, REMCOM was contracted to develop software to simulate Rotman Lens structures realized with microstrip and stripline geometries. A software called “Rotman Lens Development” (RLD) was used to realize the lens discussed here. The software itself is based on geometric optics and gives accurate first cut performance results. The lens, connected to a linear array of patch antennas, is shown in Figure 8.

Of particular interest, was the measured progressive phase shift at the output ports, given a particular input port was excited. Because of symmetry, ports designated (1, 8), (2, 7), (3, 6), and (4, 5) exhibit the same behavior with measured phase shifts on the array side exhibiting the desired progressive phase shift behavior. This is readily seen in Figure 9a [7]. Additionally, as the lens is a “time delay” beamformer, it should exhibit a linear change in phase shift over frequency. This was measured and validated [7], Figure 9b.

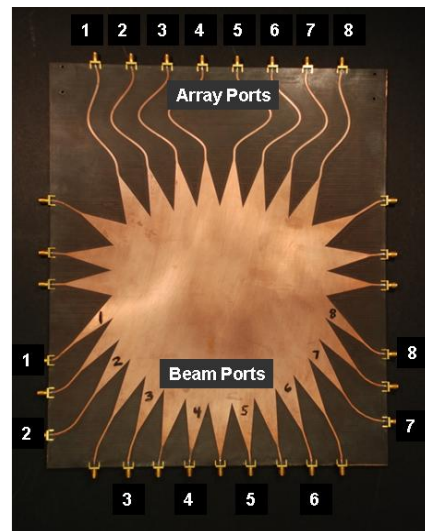


Fig. 8. Microstrip Rotman lens.

With such good measured performance, the lens was felt to be a suitable candidate for a beamformer in the C-band. A photo of the lens connected to an eight element patch antenna array is presented in Figure 10. The lens is made of a

thin (20 mil thick) dielectric (5870 Duroid.) Because of the thin nature of the structure, it is easily bent as seen in Figure 10. This bending did not affect the performance of the lens, so one could use the array in an application where it may need to be gracefully bent. For example, the lens could be located on the roof of a vehicle and the bending could be exploited so that the antenna array itself could be flush to the side of the same vehicle [8, 9].

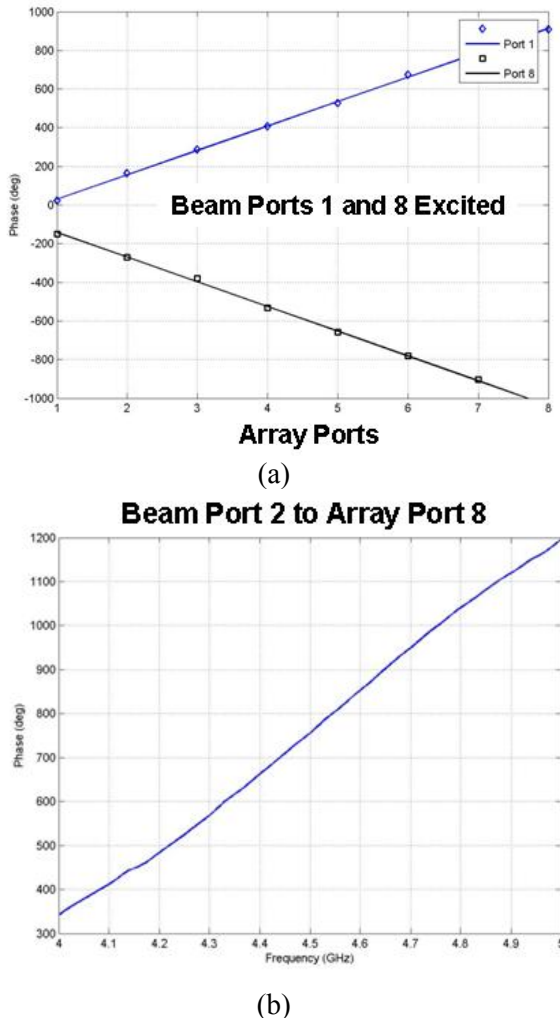


Fig. 9. Measured phase shift of microstrip.

Rotman lens: (a) Measured array aperture phase taper when beam ports 1 and 8 are excited, (b) Measured phase shift from beam port 2 to array port 8 over frequency.

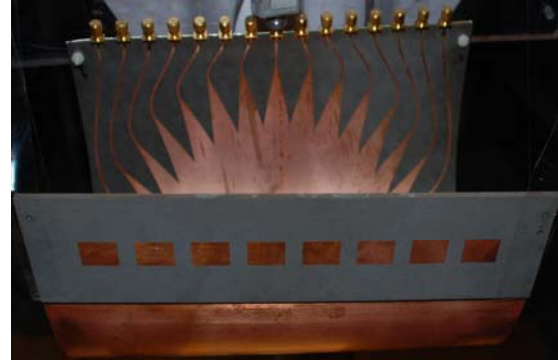


Fig. 10. The Rotman lens portion of the array is flexible and can be shaped to accommodate the geometry of the platform.

The lens discussed is flexible and lends itself to conformal integration onto a platform. Additionally, the manufacturing cost is not high. The biggest drawback is the insertion loss of the Rotman lens and the associated feed lines – measured to be on the order of 9 dB. ARL has addressed the loss issue with a lens made using a cavity and waveguide feeds [4 - 7]. Such a lens is shown in Figure 11. The lens on the left was machined from Aluminum and weighed about 14.65 lbs. Because of the solely metallic realization of the structure, the insertion loss was measured to be on the order of 3 to 4 dB – a significant improvement over the photo-etched Rotman lens design. However the cost and complexity of the design were greatly increased. Shown on the right is a duplicate design made of Ultem 1000 and gold plated. This lens was significantly lighter (6 lbs) and achieved comparable (actually, slightly better) performance. This design remains an item of study because of the possibility of realizing the structure through injection molding, thus reducing the cost significantly.

Integrated Phased Array Designs:

Integrated phased array designs can pose some special design challenges depending on the application of interest. For satellite communications in tactical environments, low-profile electrically scanned antenna arrays are particularly desirable. One possible candidate for this challenging implementation is the wafer level antenna arrays. These arrays tend to be of interest for applications where the wavelength of the operation tends to be small relative to the size of

the wafer. As an example, ARL is investigating a linear 4-element array with integrated MEMS phase shifters (from Raytheon Corp.) for concept validation.

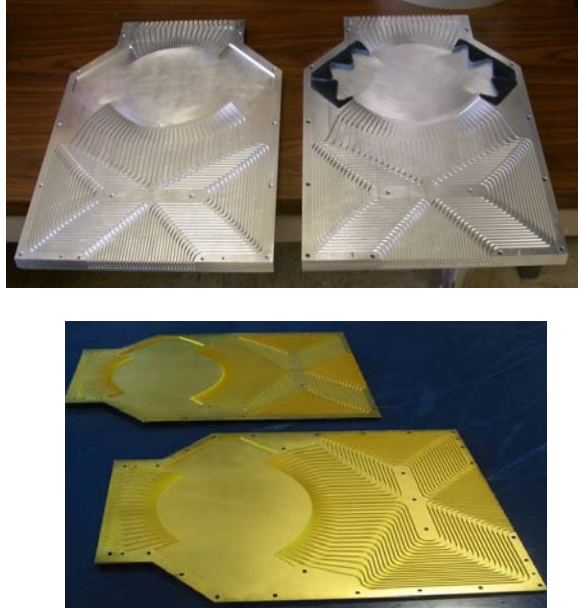


Fig. 11. Ka-band Rotman lens realized with a cavity and waveguide transmission lines.

The individual wafer-level element itself is constrained by the physical parameters of the wafer. For our case study, a high resistivity silicon wafer substrate (relative dielectric ~ 11.7) was used. The thickness of the wafer was $500 \mu\text{m}$. A key challenge became the feeding mechanism for the radiating element (a patch antenna) after the wafer was processed. Figure 12 illustrates ARL's unique feed mechanism that will permit an integrated phased array design. Note that the antenna is fed by a slot (aperture), but the feed line is on the same level as the slot itself. This is a departure from the traditional slot fed patch antenna that requires a separate patch and feed layer to be bonded together. The transmission line is coplanar waveguide (CPW) that facilitates integration to MEMS phase shifters that have CPW RF ports.

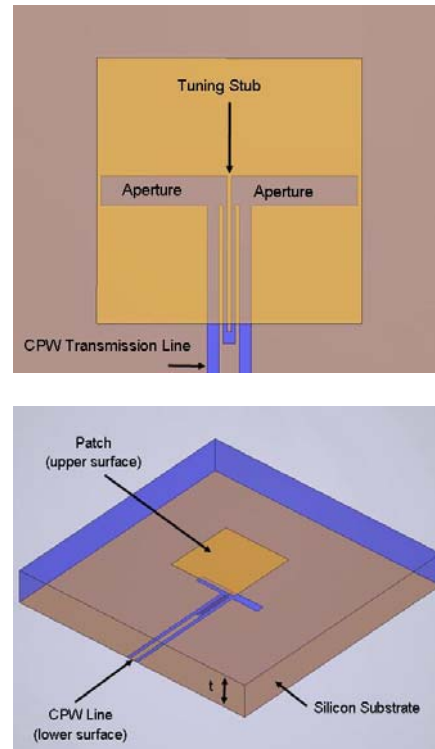


Fig. 12. Geometry of the wafer level patch antenna – top view and a perspective view.

This antenna was fabricated and measured to validate its performance. In Figure 13, one can see the construction of the individual element. Also shown is the back side of the wafer with 4 MEMS phase shifters integrated into the design. Figure 14 presents measured data validating scanning (for a progressive phase shift of ± 45 Degrees.) While the patterns demonstrated the scanning, much work needs to be done on optimization. In particular, the tolerances on the phase of the MEMS devices has been significantly improved on subsequent fabrication runs.

In conclusion, this wafer level phased array design has illustrated the conceptual approach used by ARL when faced with a design that has constraints dictated by the fabrication environment – in this case the wafer itself. We were able to realize a unique feed that facilitated integrated MEMS phase shifters into the architecture of the feed layer. The design was built and tested validating preliminary simulated results.

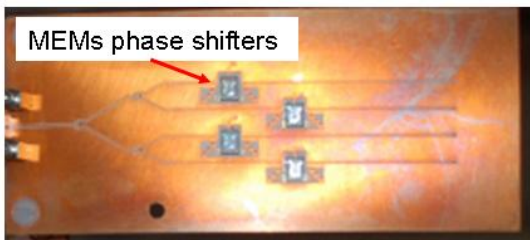
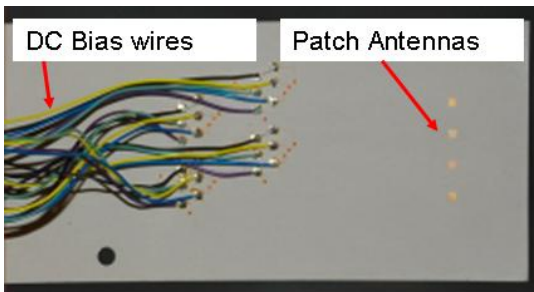
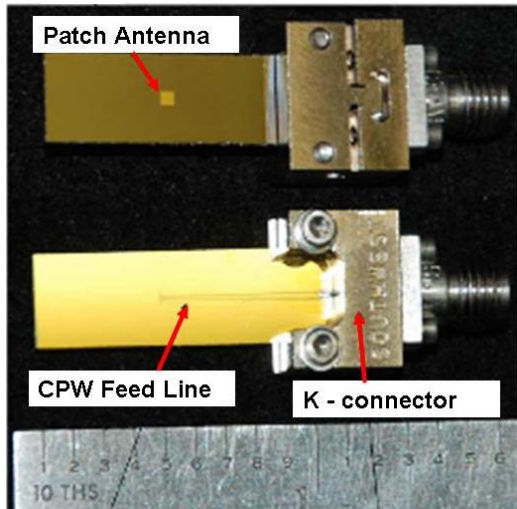


Fig. 13. Prototype wafer patch antenna and an integrated 4-element array on a wafer.

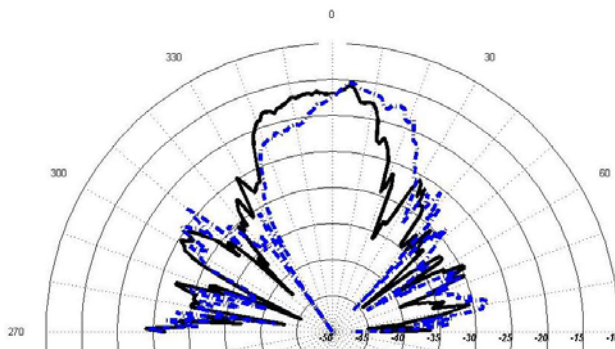


Fig. 14. Radiation pattern of the 4-element array demonstrating scanning.

Collision Avoidance Radar:

An application of basic antenna array with a tapered aperture for side-lobe control is in collision avoidance radar system for Army vehicles [10]. The requirements call for a broad beam (around 35 degrees) in azimuth and elevation (around 35 degrees) for the transmit antenna and a narrow beam that scans in azimuth within certain view angle (around 30 degrees) for the receive antenna. The receive azimuth beam width is around 2 degrees, with side-lobe levels of 40 dB below peak. Elevation beam width is around 35 degrees. No electronic scanning is required in the individual array. However, individual arrays would be stacked and bore-sighted at 2-degree angle intervals in azimuth. The scanning is then achieved by switching the output of the receive array at the required scanning speed in the 2-degree steps. The array configuration is sketched in Figure 15. The pyramidal horn array is fed with a waveguide power divider that is designed to produce the required aperture taper in the horn array [11]. The tapered power distribution as simulated using the FEM-based software package HFSS is shown in Figure 16. One of the challenges in this design is fabrication accuracy needed at the operating frequency of 76 GHz. The horn array and its waveguide feed network are integrated and cut in two blocks as shown in Figure 17. The measured and simulated radiation patterns compare favorably and are shown in Figure 18.

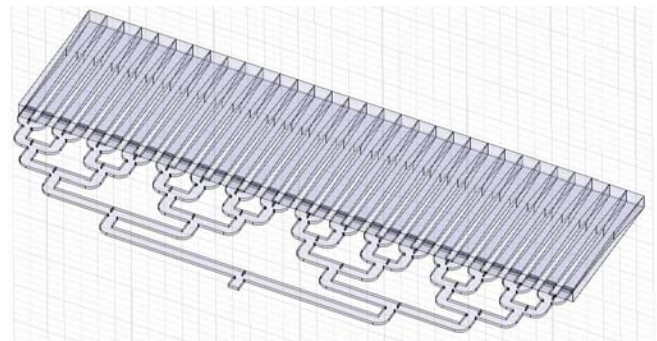


Fig. 15. Horn array configuration with feeding waveguide power dividing network.

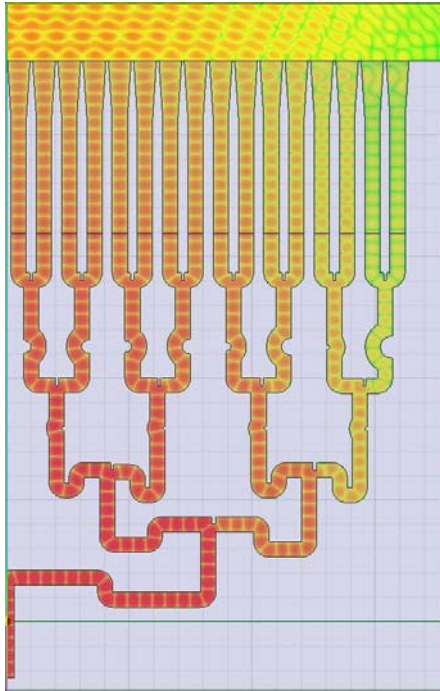


Fig. 16. HFSS model of the tapered aperture as produced by the waveguide power dividing network.

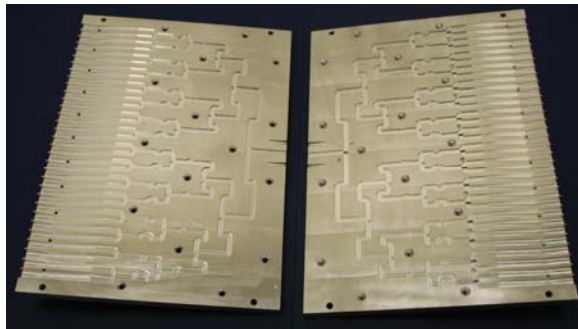


Fig. 17. Fabricated 76-GHz array.

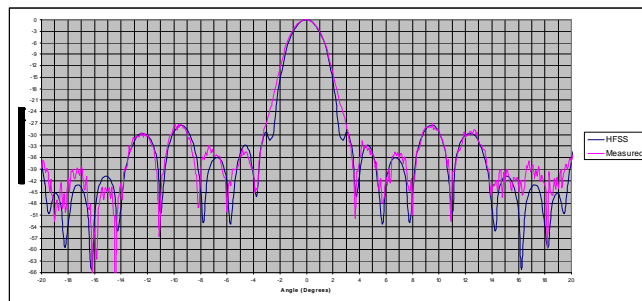


Fig. 18. Modeled and measured radiation patterns of tapered horn array.

Metamaterial Issues:

Metamaterial applications to military antenna systems have picked up considerable interest lately. The primary promise of this technology is the reduction in the antenna size without sacrificing its performance. One of the controversial issues associated with metamaterials is the realization of negative refractive index (NRI) in the medium. This results from dual negative constitutive parameters, which may be realized using a combination of split ring resonators, or capacitively loaded loops, for negative permeability, and conducting poles for negative permittivity. An HFSS simulation and corresponding fabrication of such a medium were the subject of an experiment conducted at the Army Research Lab to show the refractive focusing, or lens, that results from a dual negative medium [12, 13]. Figure 19 shows the parallel-plate configuration where a metamaterial slab is placed between a source (probe # 1) and three receivers at equi-distances from the source. Probe # 2 is centered in the receiving region, while probe # 3 designates any of the other two probes on the side. Without the metamaterial slab, transmission coefficients from probes 1 to 2 and from probes 1 to 3 are very close as shown in the HFSS simulated results in Figure 20(a). The insertion of the metamaterial slab causes negative refractions that result in focusing of the energy in the center probe # 2, with lower levels detected at probe # 3 as shown in Figure 20(b). Simulated results were verified experimentally [13].

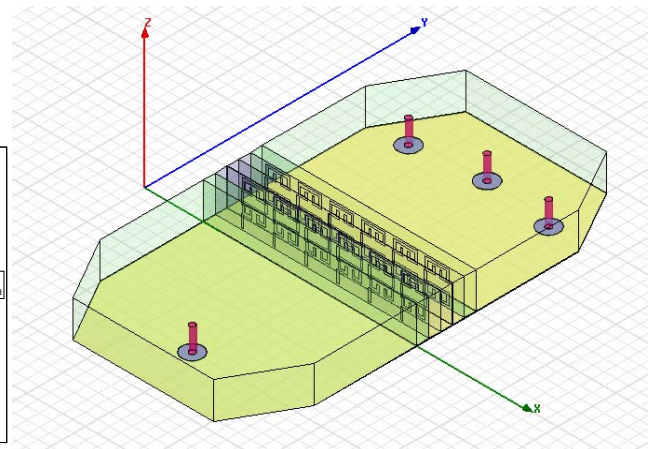


Fig. 19. Negative refractive index (NRI) block in parallel plate waveguide structure.

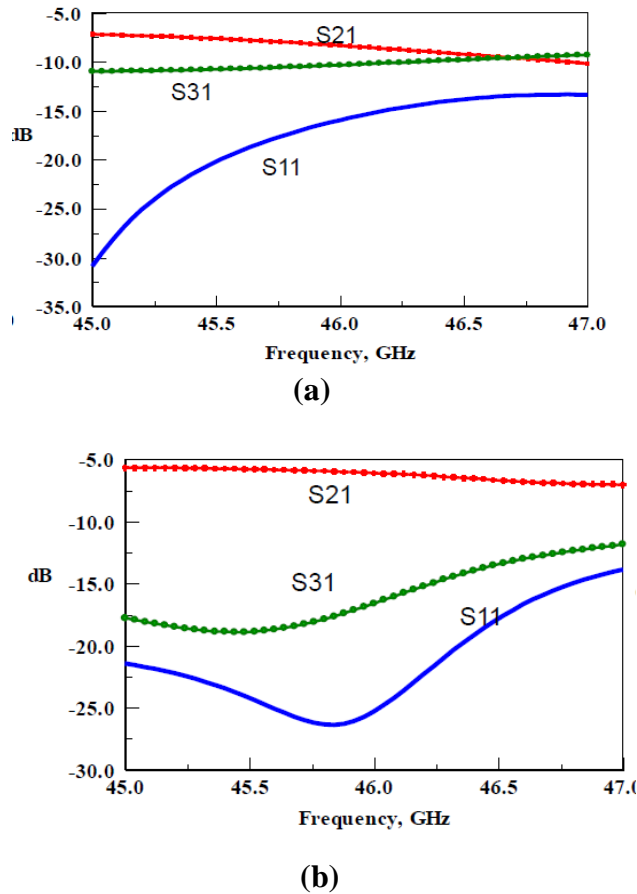


Fig. 20. S-parameters for the parallel plate structure (a) without and (b) with NRI block.

V. CONCLUSIONS

Antenna development for military applications is a collaborative process that involves government laboratories, universities and industry. Antennas have to be designed with the platform and environment in mind. This makes in-situ antenna designs and analyses essential to successful development. Antenna modeling is usually a trade-off between time and cost for a required accuracy. New simulation tools are still needed for new frontiers, such as metamaterials and nano-designs.

Examples of designs that were performed at the US Army Research Laboratory covered different technologies in waveguide and printed circuit media. Fully integrated, adaptive designs have been at the forefront of such antenna research and development. The basic goals of the designs

continue to be wideband, low profile, high efficiency, polarization diversity and low cost.

REFERENCES

- [1] S. D. Keller and W. O. Coburn, "Efficient Simulation of Wideband VHF/UHF Candidate Antennas for a UAV Platform Using FEKO," Proceedings of the 2009 ACES Conference, Monterey, CA, March 2009.
- [2] S. Weiss, W. Coburn and O. Kilic, "FEKO Simulation of a Wedge Mounted Four Element Array Antenna," ACES Journal, August 2009.
- [3] W. Rotman, and R. F. Turner "Wide-Angle Microwave Lens for Line Source Applications," IEEE Trans. on Ant. and Prop. 1963 pp. 623-632.
- [4] S. Weiss, R. Dahlstrom, "Rotman Lens Development at the Army Research Lab," Proceedings of the AESS conference, Big Sky, MT., March 2006.
- [5] O. Kilic, S. Weiss, "Dielectric Rotman Lens Design for Multi-Function RF Antenna Applications," Proc. 2004 IEEE AP-S/URSI Int. Symposium, Monterey, CA.
- [6] R. Dahlstrom, A. Bayba, "A Rotman Lens Implementation for Multifunction RF Applications," Proc. 2002 Antenna Application Symposium, Allerton Park, Monticello, Illinois.
- [7] S. Weiss, S. Keller, and C. Ly, "Development of Simple Affordable Beamformers for Army Platforms," Proceedings of GOMACTech-07 Conference, Lake Buena Vista, FL, March 2006.
- [8] T. K. Anthony "Rotman Lens Development," "Proceedings of 2008 IEEE Ant. & Prop. Conference, San Diego, CA, July 2008.
- [9] T. K. Anthony and S. Weiss, "Development of a Flexible Electrically-Scanned Array Using a Rotman Lens," Proceedings of the 2008 URSI General Assembly Conference, Chicago, IL. August 2008.
- [10] R. Wellman, E. Adler, M. Conn, A. Zaghloul, T. Anthony, and S. Schmidt, "Advanced Perception Radar for Large Robotic Vehicles," MSS Tri-Service Radar Symposium, Boulder, Colorado, June 2009.

- [11]A.I. Zaghoul, T.K. Anthony, and S.J. Weiss, "Characterization of a 76 GHz Antenna for Personnel Avoidance Radar for Robotics Vehicles," IEEE Radar Conference, Pasadena, California, May 2009.
- [12]A.I. Zaghoul and Y. Lee, "Simulation of Refraction Focusing Using Negative-Refractive-Index Metamaterials ," IEEE International Symposium on Antennas and Propagation, San Diego, California, July 2008.
- [13]A.I. Zaghoul, Y. Lee and S. Weiss, "Measurements of Refraction Focusing Using Negative-Refractive-Index Metamaterials ," USNC/URSI National Radio Science Meeting, San Diego, California, July 2008.



Amir I. Zaghoul is with the US Army Research Lab (ARL) on an IPA (Inter-Governmental Personnel Act) agreement with Virginia Polytechnic Institute and State University (Virginia Tech), which he had joined in 2001 as Professor in the Bradley

Department of Electrical and Computer Engineering. Prior to Virginia Tech, he was at COMSAT Laboratories for 24 years performing and directing R&D efforts on satellite communications and antennas. He is a Fellow of the IEEE, an Associate Fellow of The American Institute of Aeronautics and Astronautics (AIAA), a Member of Commissions A, B & C of the International Union of Radio Science (URSI), and a member of the Board of the Applied Computational Electromagnetics Society (ACES).

Dr. Zaghoul received the Ph.D. and M.A.Sc. degrees from the University of Waterloo, Canada

in 1973 and 1970, respectively, and the B.Sc. degree (Honors) from Cairo University, Egypt in 1965, all in electrical engineering.



Steven J. Weiss was born in Utica, NY in 1955. He graduated from The George Washington University in 1995 with a doctoral degree in Electrical Engineering. He is presently with the Army Research Lab working with antenna systems. His research areas include specialized antennas for military applications. He is a senior member of the IEEE Antennas and Propagation Society.

William O'Keefe Coburn received his BS in Physics from Virginia Polytechnic Institute in 1984. He received an MSEE in Electro physics in 1991 and Doctor of Science in Electromagnetic Engineering from the George Washington University (GWU) in 2005.



He has 28 years experience as an electronics engineer at the Army Research Laboratory (formerly the Harry Diamond Laboratories) primarily in the area of CEM for EMP coupling/hardening, HPM and target signatures. He currently is in the RF Electronics Division of the Sensors and Electron Devices Directorate applying CEM tools for antenna design and analysis.

Low-profile, Broadband Polarization Converting Surface Ground Planes for Antenna Polarization Diversity

Brian A. Lail¹ and Kyu Y. Han²

¹ Department of Electrical and Computer Engineering
Florida Institute of Technology, Melbourne, FL 32901, USA
blail@fit.edu

² Wavebender, Inc.
Milpitas, CA 95035
ilrowa@hotmail.com

Abstract— A broadband antenna backed by a polarization converting surface ground plane is presented. The conversion of reflected field polarization provides diversity from a single, linearly polarized antenna, while avoiding broadside nulls in the radiation pattern as a function of frequency. Results for a low-profile dipole planar inverted cone antenna $\sim\lambda/10$ above a polarization converting surface indicate greater than 40% bandwidth. Comparison with solid ground planes and high impedance ground planes are discussed, with polarization diversity and lack of broadside nulls identified as key advantages to the proposed design.

Index Terms— polarization converting surface, ground plane, polarization diversity, broadband antenna

I. INTRODUCTION

Antennas are often placed above a ground plane to enhance the directivity in the topside half-plane. Antennas over a solid conducting ground plane require a $\lambda/4$ standoff in order to produce constructive phase combinations for maximum directivity in the broadside direction. This result is due to radiation which propagates in the backside direction, reflects off the conducting plane with a π phase shift, and combines in-phase with the direct radiation in the broadside direction. By placing periodic conducting structures on a substrate over, but electrically close to, the solid conducting plane the reflection phase shift can be engineered. A high impedance ground plane, sometimes called an artificial magnetic conductor

(AMC), results when the reflection phase is zero, such that a standoff height to the antenna is not required in order to achieve in-phase broadside addition [1], [2]. The ground plane is made up of a solid conducting plane, a standoff layer, and an array of elements forming the periodic structure. When a high impedance ground plane is formed with symmetric elements peak broadside gain is achieved for an antenna placed near this ground plane. For both the symmetric-element AMC and the solid ground plane, the polarization sensitivity of the antenna is preserved in the process of back reflected radiation. In this paper we show that by using asymmetric elements a ground plane can be designed that provides polarization diversity. The asymmetric elements serve as polarization converting surface (PCS) such that a linearly polarized incident field is converted to its orthogonal polarization state upon reflection. Even though the antenna by itself is linearly polarized, the far-field combination of the direct field and the polarization-converted reflected field contains both polarization components. Furthermore, the PCS backed antenna does not suffer from nulls in the broadside radiation pattern as frequency is varied, as would be the case for a solid ground plane or AMC.

II. POLARIZATION CONVERTING SURFACES

Twist reflectors have been used for nearly four decades in Cassegrain antenna systems to reduce aperture blocking [3]-[5]. For sake of discussion we will consider the asymmetric elements comprising the patterned surface as metallic strips.

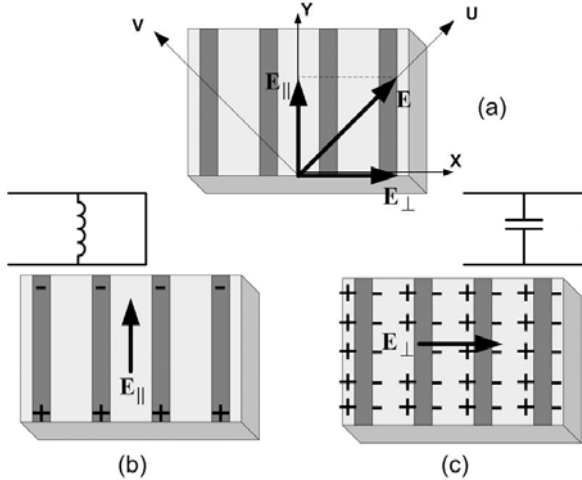


Fig. 1. Twist reflector basic mechanism. (a) The x-polarized E-field is resolved into two components: parallel and perpendicular to the metallic pattern. (b) and (c) charge distribution and their equivalent circuits.

The principle of operation of the twist reflector is understood by considering an incident plane wave with its electric field vector slanted at 45° with respect to the metallic strips. Then this electric field vector can be resolved into two equal components, E_{\parallel} and E_{\perp} as shown in Fig 1(a).

These components are in phase when the wave impinges onto the structure. Fig. 1(b) shows the parallel E-field component reflected through a structure equivalent to a shunt-inductive filter while Fig. 1(c) shows the perpendicular E-field component reflected through a shunt-capacitive filter [5]. As a result, the phase of the parallel component is advanced by the metallic strip while the perpendicular component is delayed. When the relative phase difference between two E-field components becomes 180° , the polarization vector is twisted by 90° upon reflection.

Polarization conversion has a unique signature depending on the observation coordinate system. In the XY configuration, as shown in Fig. 2, the co-polarized reflection phase is measured for the parallel and perpendicular orientation, and polarization conversion corresponds to a π relative phase between these components.

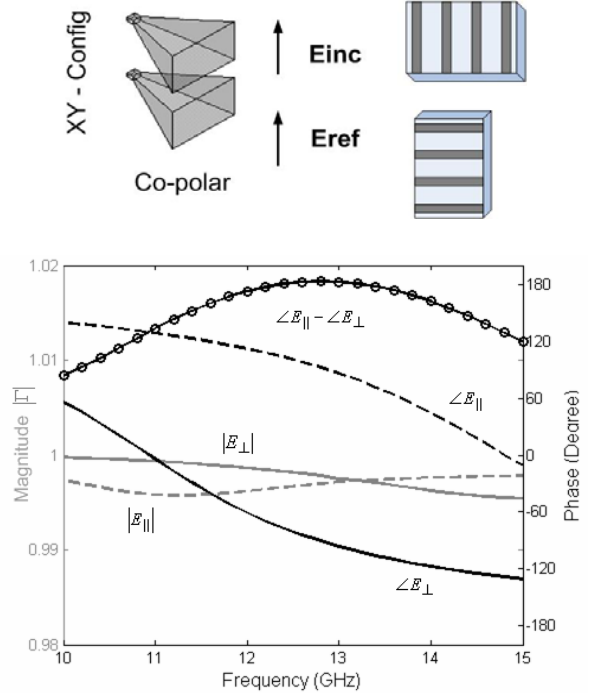


Fig. 2. Polarization conversion in the XY configuration occurs when the relative phase between x- and y-polarized reflected fields is approximately 180° .

In the UV orientation, polarization conversion occurs when the co-polarized reflection field magnitude is reduced while the cross-polarized reflection field magnitude is near unity, as shown in Fig. 3.

PCS have been designed using the genetic algorithm (GA) in order to achieve low-profile, broadband operation [6]. Fig. 4 is a characterization of polarization conversion through polarization loss, or the ratio of power in the converted polarization to the total reflected power.

$$\text{Polarization Loss} = PL = \frac{\text{Desired Reflected Power}}{\text{Total Reflected Power}}$$

A polarization loss greater than -0.1 dB corresponds to 98% power conversion. In Fig. 2 greater than 98% power in the incident linear polarization state is converted to the orthogonal polarization state over frequencies 9.5 – 11.7 GHz.

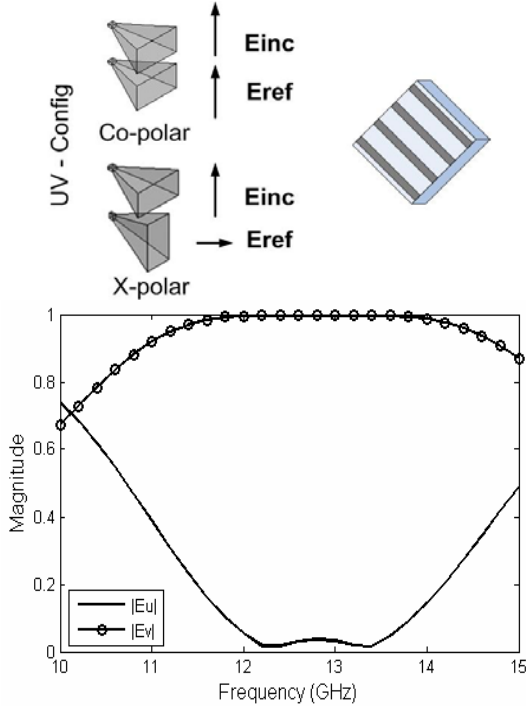


Fig. 3. In the UV coordinate system near unity magnitude of the cross-polarized reflected field represents polarization conversion.

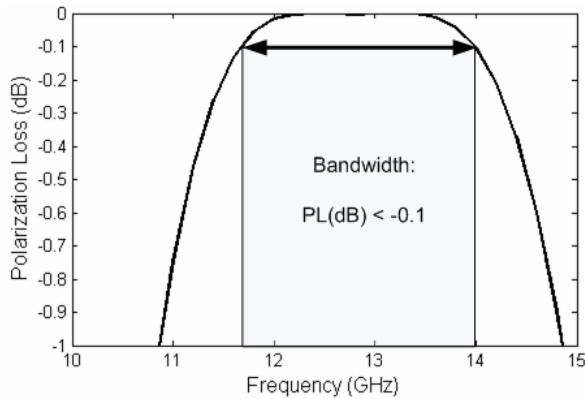


Fig. 4. Polarization Loss for the cases shown in Figures 2 and 3.

III. GENETIC ALGORITHM

Fig. 5 shows an overall GA flow diagram that is employed to design a twist reflector. A chromosome is the binary form of a structure that includes all the parameter information.

Decoded chromosomes using binary-decoding method [7] are evaluated by HFSS. Once fitness values for all the members of a population are assigned, randomly selected members based on fitness values are evolved through reproduction process: crossover and mutation [8].

Among various strategies for selection and crossover, tournament selection and single-point crossover are employed in our implementation, respectively.

The common twist reflector with thickness $0.25\lambda_0$ to $0.358\lambda_0$ shows bandwidth of 10 – 25 % [9]-[12]. Some twist reflector models exhibit bandwidth of more than several octaves [5], [9] but these structures are constructed using multi-layers with thickness bigger than $0.358\lambda_0$. The purpose of this study is to generate a novel unit cell that exhibits a polarization converting property over a wide frequency range while keeping the thickness less than quarter-wavelength.

The goal of the GA in twist reflector design is to produce a relative phase difference of 180° between parallel and perpendicular response, as explained in the previous section. Equivalently, polarization conversion can be directly observed by co-polar and cross-polar magnitude responses. For example, for an x-polarized incident wave propagating in the z-direction, the fitness function can be described as:

$$\text{fitness function} = \max \left(\sum_{\text{freq}=8-14\text{GHz}} (|E_y| - (1 - |E_x|)) \right)$$

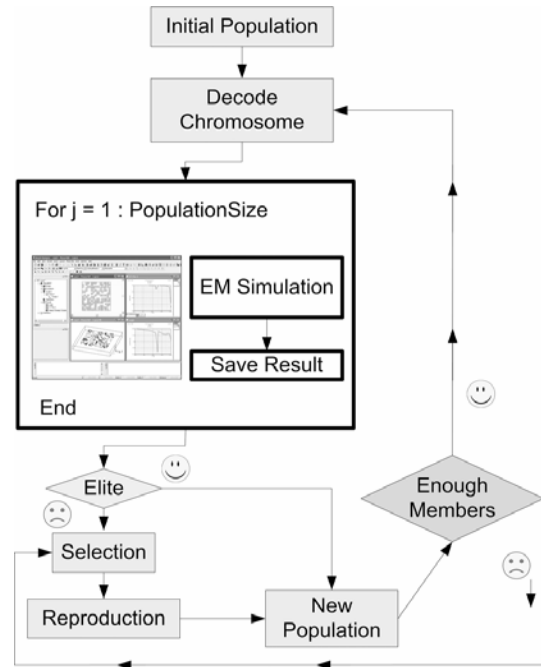


Fig. 5. Overall GA flow diagram.

IV. PCS DESIGNS

For unit cell design, there are a number of ways to parameterize the surface pattern. One popular way in the design of metamaterials is to form a unit cell with binary pixels where pixels with “0”s and “1”s represent empty spaces and conductors, respectively. In this way, GA can explore various surface shapes to generate an optimal solution. As an initial exercise of the GA tool a unit cell consisting of 16x16 binary pixels was the basis of a PCS design with fitness function targeting polarization conversion at 9.5 ± 0.3 GHz. In order to avoid corner point contacts pixels were overlapped by 0.1 mm [14], [15].

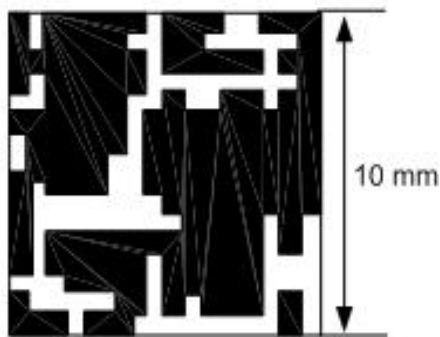


Fig. 6. Unit cell consisting of 16x16 binary pixels.

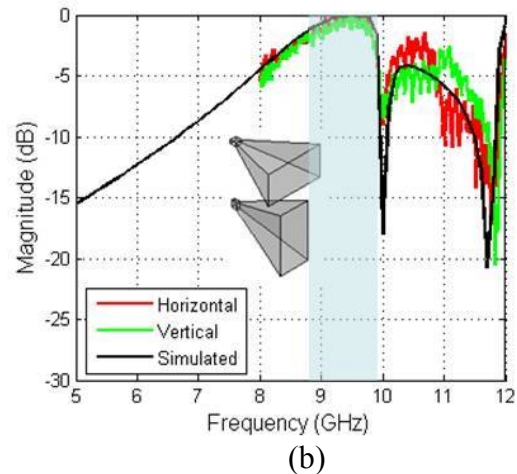
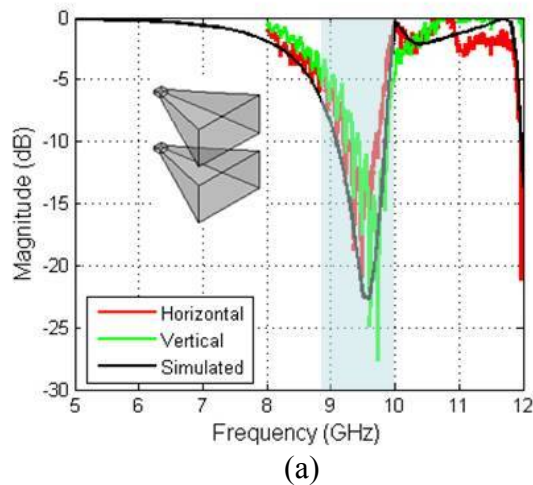
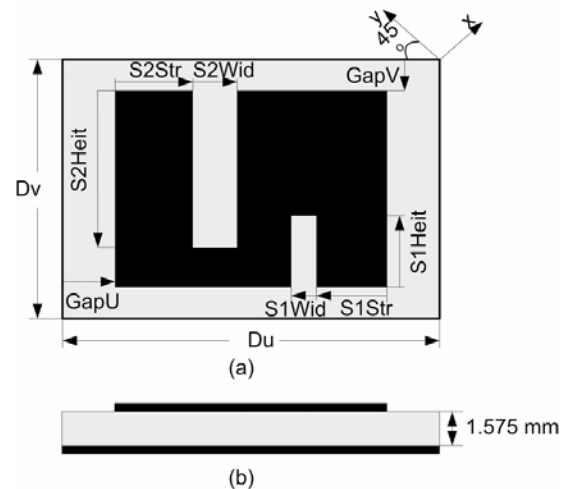


Fig. 7. Co-pol (a) and cross-pol (b) response of the initial GA designed PCS showing polarization conversion for 9.5 ± 0.3 GHz. Simulated data is from Ansoft HFSS models.

A 21 cm x 14 cm PCS with the unit cell shown in Fig. 6 was fabricated on Duroid 5880 of thickness 1.575 mm. Measured and modeled results are shown in Fig. 7. While the pixelated unit cell design meets the fitness requirement for polarization conversion for $f = 9.5 \pm 0.3$ GHz, the performance falls off rapidly outside of this range of frequencies. Recognizing that the unit cell of Fig. 6(a) resembles a meandered structure, the parameter space was further constrained.



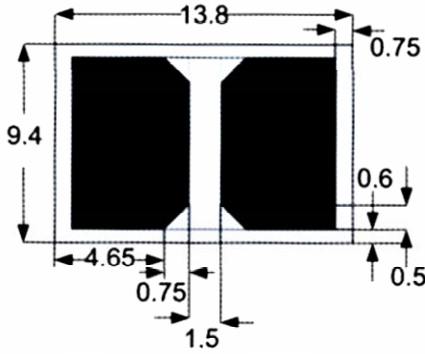


Fig. 8. GA parameter setup: top view (a), side view (b), and the optimized unit cell design (c).

The parameter space used to represent a unit cell in the optimized design is shown in Fig. 8. Based on twist reflector mechanism, the initial structure is rotated by 45° relative to the incident wave. Then, a rectangular conductor is generated inside of the unit cell and subtracted by two independent slots. In this way, GA can explore any size of rectangles, strip lines, and meanderline.

Ten parameters are involved in the GA process are shown in Fig. 8(a): unit cell width (D_u) and height (D_v), vertical ($GapV$) and horizontal ($GapU$) gap between the adjacent unit cells, and starting point ($S1Str$ and $S2Str$), width ($S1Wid$ and $S2Wid$), and height ($S1Heit$ and $S2Heit$) for two slots.

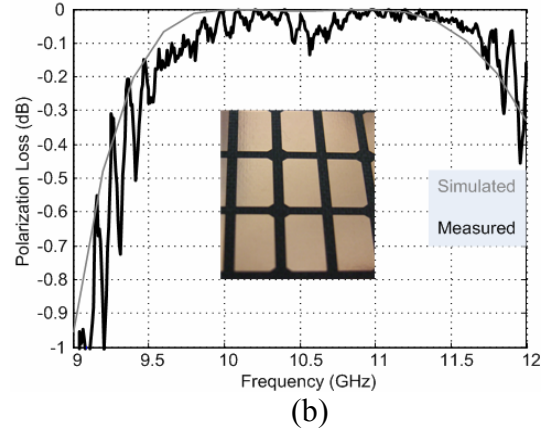
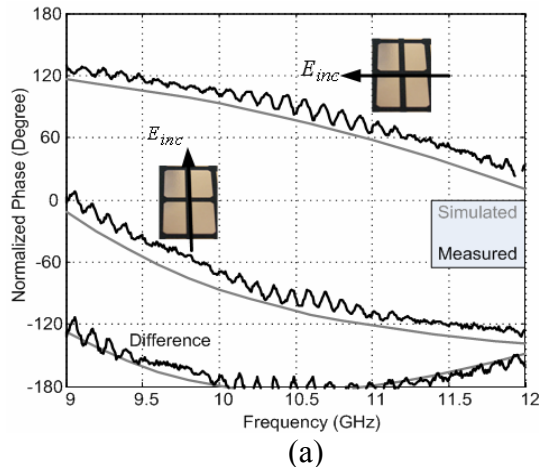


Fig. 9. PCS reflection phase (a) and polarization loss (b). Simulated data is from Ansoft HFSS models.

Fig. 8(c) shows the PCS unit cell geometry, while Fig. 9a shows modeled and measured reflection phase of the x- and y-components and the difference between these phases. Polarization is converted upon reflection when the difference in phase between the x- and y-components is π radians. Fig. 9b is a characterization of polarization conversion through polarization loss, or the ratio of power in the converted polarization to the total reflected power. A polarization loss greater than -0.1 dB corresponds to 98% power conversion. Greater than 98% power in the incident linear polarization state is converted to the orthogonal polarization state over frequencies 9.5 – 11.7 GHz.

V. PCS GROUNDPLANE BACKED ANTENNA

A linearly polarized antenna over a reflective ground plane is considered. For comparison, we include solid perfect conductor (PEC), AMC, and PCS ground planes in this discussion. For this treatment we assume perfect reflection and no losses. Consider a dipole antenna that is aligned with the uv-coordinate axes and the ground plane beneath the antenna contains elements that are periodic in and aligned with the xy-axes.

Using the total far-field expressions, the broadside gain for each case is plotted in Fig. 10. Since the PEC plane provides a π phase shift upon reflection we plot broadside gain as a function of standoff height d . For both AMC and PCS we consider a negligible standoff height and plot gain as a function of reflection phase shift.

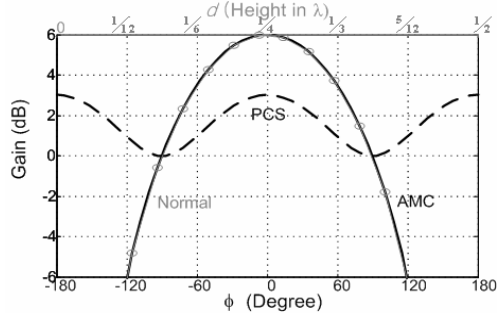


Fig. 10. Broadside power comparisons.

From Fig. 10 we see that while the PCS ground plane does not provide the peak broadside power of the PEC or AMC ground plane, the direct and reflected fields never add destructively so that there is never a broadside null. The PEC or AMC ground planes constrain broadband operation due to the nulls that develop in the total far field as wavelength moves away from the design value. Furthermore, the PCS and AMC fields are linearly polarized according to the alignment of the antenna.

Antenna elements with broadband performance are required to utilize with the proposed broadband PCS. One of the simplest structures that exhibit such a broadband performance is the Low-profile Dipole Planar Inverted Cone Antenna (LPdiPICA) [16], [17]. Fig. 11 shows the geometry and dimensions of the LPdiPICA antenna used in this work.

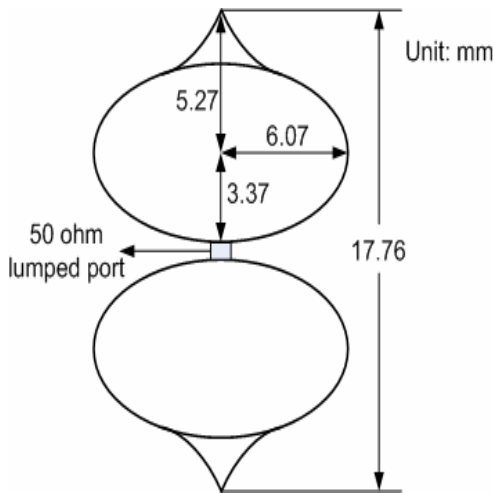


Fig. 11. LPdiPICA antenna.

The broadside gain of the LPdiPICA antenna shown in Fig. 11 is compared for three cases in Fig. 12. The black dashed line is the antenna with no back reflector. The blue curve is gain when the antenna is $\lambda/4$ above a solid ground plane. The red curve is the LPdiPICA 3mm above a PCS ground plane. The solid ground provides maximum broadside gain, but as frequency is varied this gain falls off. LPdiPICA antenna above a PCS structure exhibits 5.7–7.1 dB gain over frequency range of 7–11 GHz, while providing diversity through the conversion of the reflected field polarization, and low-profile with a standoff height $\sim\lambda/10$.

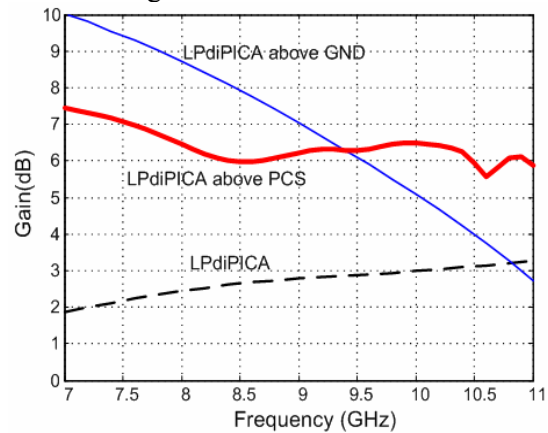


Fig. 12. LPdiPICA broadside gain.

VI. CONCLUSIONS

The benefits of a PCS ground plane have been identified to be polarization diversity from a single, linearly polarized antenna and no nulls in the broadside radiation pattern as frequency is swept. The PCS achieves low profile geometry, much like AMC. However, by converting the reflected field polarization the far field combination of direct and reflected fields never destructively interfere, such that there are never nulls in the broadside radiation pattern. The trade-off is that the PCS ground plane does not have the peak broadside gain of a solid ground plane or AMC. A LPdiPICA antenna backed by a PCS ground plane was presented with greater than 40% bandwidth in the integrated design. When combined with a broadband antenna, the low-profile PCS ground plane provides both broadband operation and polarization diversity.

REFERENCES

- [1] D. Sievenpiper, L. Zhang, R. F. J. Broas, N. G. Alexopolous, and E. Yablonovitch, "High-impedance electromagnetic surfaces with a forbidden frequency band," *IEEE Trans. Microwave Theory Tech.*, vol. 47, pp. 2059-2074, Nov. 1999.
- [2] A. P. Feresidis, G. Goussetis, S. Wang, and J. C. Vardaxoglou, "Artificial Magnetic Conductor Surfaces and Their Application to Low-Profile High-Gain Planar Antennas," *IEEE Trans. Antennas Propagat.*, vol. 53, no. 1, pp. 209–215, Jan. 2005.
- [3] P. W. Hannan, "Microwave Antennas Derived from the Cassegrain Telescope," *IRE Trans. Antennas Propagat.* Vol. 9, pp 140–153, Mar. 1961.
- [4] M. I. Skolnik, *Introduction to Radar Systems*, 3rd ed. New York: McGraw-Hill, 2001, pp. 661–672.
- [5] E. Orleansky, C. Samson, and M. Havkin, "A Broadband Meanderline Twistreflector for the Inverse Cassegrain Antenna." *Microwave J.*, vol. 30 no. 10, pp. 185 – 192, Oct. 1987.
- [6] K. Y. Han and B.A. Lail, "Genetically Engineered Meanderline Twist Reflector," IEEE Antennas and Propagation Society International Symposium, pp. 1-4, 5-11 July 2008.
- [7] J. M. Johnson and Y. Rahmat-Samii, "Genetic Algorithms in Engineering Electromagnetics," *IEEE Antennas Propagat. Mag.*, vol. 39, no. 4, pp. 7–21, Aug. 1997.
- [8] R. L. Haupt, "An Introduction to Genetic Algorithms for Electromagnetics," *IEEE Antennas and Propagation Magazine*, vol. 37, no. 2, pp. 7–15, April 1995.
- [9] H. Jasik, Ed., *Antenna Engineering Handbook* New York: McGraw-Hill, 1961, pp. 25– 6.
- [10] E. L. Holzman, "Transreflector Antenna Design for Millimeter-Wave Wireless Links," *IEEE Antennas and Propagat Mag.*, vol. 47, no. 5, pp. 9–22, Oct. 2005.
- [11] T., K. Wu, R. Palos, and D. L. Helms, "Meanderline Polarization Twister," U.S. Patent 4 786 914,, Nov. 22, 1988.
- [12] W. H. Shi, W. X. Zhang, and M. G. Zhao, "Novel Frequency-Selective Twist Polariser," *Electronics Lett.* 7th vol. 27, no. 23, pp. 2110–2111, Nov. 1991.
- [13] E. K. English and E. C. Saladin, "Electromagnetic-Field Polarization Twister," U.S. Patent 0 227 417, Dec. 11, 2003.
- [14] M. Ohira, H. Deguchi, M. Tsuji, and H. Shigesawa, "Multiband Single-Layer Frequency Selective Surface Designed by Combination of Genetic Algorithm and Geometry-Refinement Technique," *IEEE Trans. Antennas Propagat.*, vol. 52, no. 11, pp. 2925-2931, Nov. 2004.
- [15] M. John and M. J. Ammann, "Wideband Printed Monopole Design using a Genetic Algorithm," *IEEE Antennas Wireless Propagat. Lett.*, vol. 6, pp. 447–449, 2007.
- [16] S. Y. Suh, W. L. Stutzman, W. Davis, A. Waltho, and J. Schiffer, "A Novel Broadband Antenna, the Low-Profile Dipole Planar Inverted Cone Antenna (LPdiPICA)," IEEE Antennas and Propagation Society International Symposium, vol. 1, pp. 20–25, June 2004.
- [17] S. Y. Suh, A. E. Waltho, V. K. Nair, W. L. Stutzman, and W. A. Davis, "Evolution of Broadband Antennas from Monopole Disc to Dual-polarized Antenna," IEEE Antennas and Propagation. Society International Symposium, pp. 1631–1634, July 2006.

A Numerical Study of Coaxial Helical Antennas

William Coburn

U.S. Army Research Laboratory
Adelphi, MD 20783
wcoburn@arl.army.mil

Abstract– A FEKO model was constructed to investigate two helical antennas integrated coaxially on a shaped ground plane. One antenna was designed to have a reasonable gain and axial ratio (AR) from 0.5 – 0.9 GHz and the other from 1.0 – 1.6 GHz. In principle, the antennas could be connected in parallel to provide a near 50 Ω input impedance and act as a wideband antenna. However, this connection is problematic and can make fabrication more complex while changing the input impedance in unpredictable ways. An alternative is to use a microstrip impedance transformer to provide a 50 Ω input to each antenna. Then a broadband splitter can be used for a single feed wideband antenna. Otherwise, these two ports with switched input allow dual-band operation. The FEKO model is described and simulation results are presented for both cases. These results encourage further virtual prototyping and prototype fabrication for model validation.

Index Terms– Helical antenna, circular polarization, dual-band, fiberglass, Method of Moments, FEKO

I. INTRODUCTION

An axial mode helical antenna is often a good candidate when circular polarization (CP) is required over a moderate bandwidth (BW). The classical design is well established with design equations and measured data readily available [1]. The FEKO (www.FEKO.info) model, design procedure and fabricated prototypes are described in a companion paper for the low frequency helix (LFH) [2]. That paper describes a helical conductor embedded in thin fiberglass and mounted to a shaped ground plane with the antenna having a hollow core. It may be possible to take advantage of this empty space by

incorporating a high frequency helical (HFH) antenna, shown in Fig. 1.

To this end a FEKO model was constructed to investigate two helical antennas integrated coaxially on a shaped ground plane. The LFH was designed to have reasonable gain and axial ratio (AR) over a 0.5 – 0.9 GHz BW while the high frequency helix (HFH) was designed for a 1 – 1.6 GHz BW. In these frequency bands the propagation mode on each antenna is the fundamental axial mode with coupled modes similar to the bifilar helix [3]. The antennas could be connected in parallel to provide near 50 Ω input impedance and act as a potential wideband antenna allowing for perturbed radiation patterns. However, this connection can make fabrication more complex and changes the input impedance unpredictably. An alternative is to use a microstrip impedance transformer to provide a 50 Ω input to each antenna. Then a broadband splitter can be used for a single feed wideband antenna. Otherwise, these two ports with switched input allow dual-band operation.

In this paper, the FEKO model is described and numerical results are presented for both cases subject to assumptions about the dielectric properties of materials used in the prototype fabrication. The thin dielectric sheet (TDS) or coated wire approximations are options in FEKO suitably representing the helix embedded in thin fiberglass. The fiberglass thickness is $\sim 1/16$ -inch whereas the embedded conductor is $1/4$ -inch in diameter so it is a difficult antenna structure to model exactly. The results presented are for the coated wire approximation which is more computationally efficient than the TDS while providing similar results. An ideal embodiment, without dielectrics, is considered in addition to the laminated fiberglass fabrication. The results encourage further virtual prototyping to improve performance and fabrication for model validation.

II. FEKO MODEL

The FEKO model and classical design procedure for a 500 – 900 MHz axial mode helix were described in a companion paper and summarized here. This low-frequency helix (LFH) was designed for a center frequency of operation, $f_a = 700$ MHz corresponding to a free space wavelength, $\lambda_a = 16.87$ -inch. The resulting antenna is a 5-turn helix with pitch angle, $\alpha_a = 15.4^\circ$ having diameter $D_a = 5.56$ -inch and an axial length of 2 feet. The shaped ground plan has diameter, $D_g = 0.76\lambda_a = 12.75$ -inch with an edge height $\lambda_a/4 = 4.22$ -inch to which a thin fiberglass outer shell is attached to protect the antenna. The helical element is hollow copper tubing with diameter $\frac{1}{4}$ -inch laminated with 4-layers of fiberglass mat and cured using polyester resin. The FEKO model approximates this construction by a helical conductor wound for right-hand circular polarization (RHCP) with the coated wire approximation in FEKO used as a computationally efficient way to represent the thick conductor embedded in thin fiberglass.

The classical helix design has primarily resistive input impedance near 140Ω and is typically matched to 100Ω [4]. The FEKO model includes a linear tapered microstrip impedance transition (3-inch in length) from 50 to 100Ω so in all cases the simulations correspond to $50\text{-}\Omega$ source impedance. The helical conductor embedded in fiberglass shifts the gain BW to lower frequencies proportional to the fiberglass dielectric properties and thickness. This shift is predicted and can be approximately modeled in the Method of Moments (MoM) by a fiberglass coating on a helical conductor subject to the thin-wire approximation. The antennas considered here are modeled without dielectrics or using the electrically thin coating approximation in FEKO. The cured fiberglass laminate contains about 20% resin and is modeled with relative permittivity, $\epsilon_r = 4.5$ and loss tangent, $\tan\delta = 0.02$. These parameters are estimates based on measurements which indicate that typical cured resin systems have large loss at microwave frequencies on the order $\tan\delta \sim 0.1$ [5]. The resin dominates the dielectric losses so with 20% resin content the effective loss is taken as $\tan\delta = 0.02$.

A higher frequency helix on a shaped ground plane, designed for operation from 1 – 1.6 GHz is shown in Fig. 1. It is supported by a 3-inch thick nylon base. This structure is modeled in FEKO using the Finite Element Method (FEM) with $\epsilon_r = 3.2$ and loss tangent, $\tan\delta = 0.01$. This HFH has diameter $D_b = 2.7$ -inch, so it can fit inside the lower frequency helix (Fig. 1(b)) which is also supported by a 3-inch thick nylon base. The 2-ft axial length is maintained for the HFH with 10 turns leading to $\alpha_b = 15.8^\circ$. The shaped ground plane design was based on the LFH so the edge height is roughly twice the quarter-wave height that would be more optimal for the HFH. The calculated S_{11} for HFH only with and without dielectrics is shown in Fig. 2. The addition of fiberglass lowers the antenna resistance by $\sim 20 \Omega$ without a significant change in the input reactance, so the return loss is reduced ~ 1 dB.

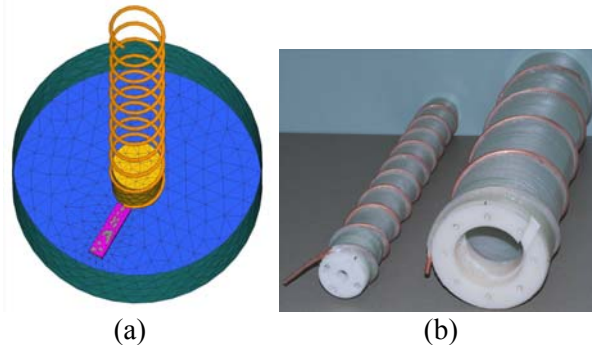


Fig. 1. (a) FEKO HFH model with nylon base on shaped ground plane and (b) the HFH (left) and LFH (right) fabricated prototypes.

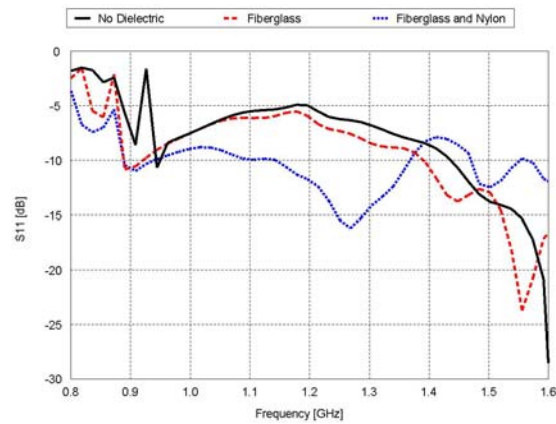


Fig. 2. Calculated S_{11} for the HFH only with and without dielectric loading.

The input impedance variation due to the effect of the nylon base, attached to the ground plane, is more pronounced and cannot be neglected. The impedance transformer substrate (RT Rogers/Duroid 5880) and the nylon base are modeled using the FEM while the fiberglass is included using the coated wire approximation. The RHCP realized gain (in dBic) shown in Fig. 3 is on the helix axis, or boresight, where the reduced gain around 1.2 GHz was roughly independent of the dielectric loading. Selected patterns for the HFH only with all dielectrics included are shown in Fig. 4.

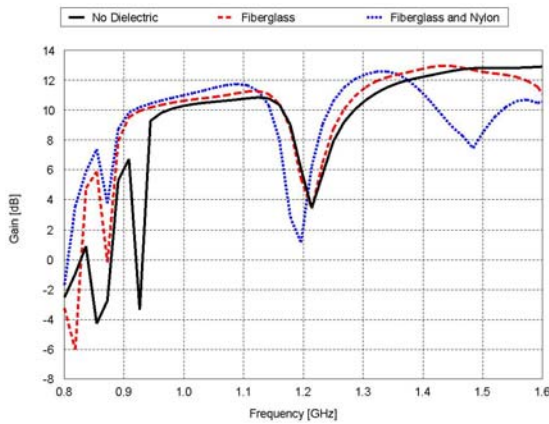


Fig. 3. Calculated RHCP realized gain on boresight for the HFH only with and without dielectric loading.

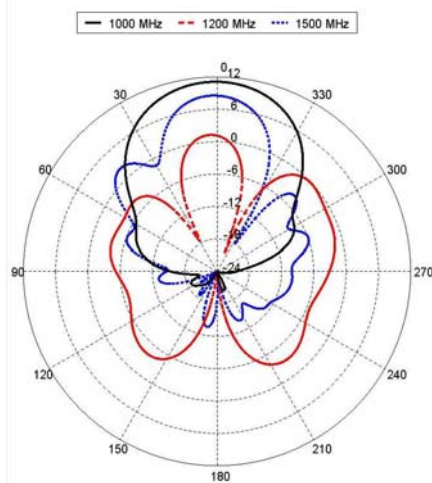


Fig. 4. Calculated RHCP realized gain patterns for the HFH only with dielectric loading.

The reduced gain at 1.2 GHz is associated with the ground plane edge height. This null can be improved and shifted in frequency by reducing

this edge height as shown in Fig. 5. The original model compared to one having half the ground plane height has the same 90% efficiency but has drastically different radiation patterns. This change could introduce pattern perturbations at low frequency and is a parameter to optimize in the future for the dual helix configuration.

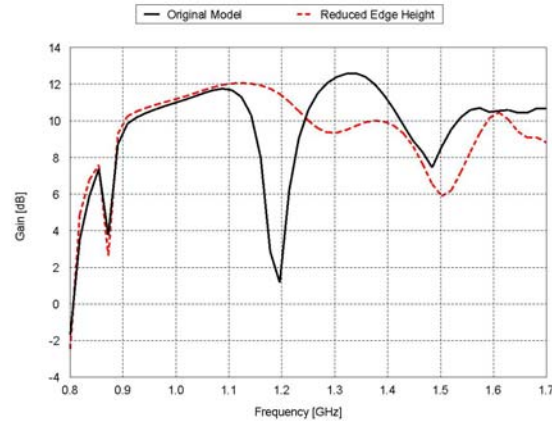


Fig. 5. RHCP realized gain comparison for the HFH only with reduced ground plane edge height.

The LFH and HFH models are combined in a coaxial arrangement as shown in Fig. 6. A gap in the LFH nylon base is provided to attach the microstrip transformer output to the HFH input. The input connectors are attached to the bottom of the ground plane directly below the transformer inputs with pins connected directly to the microstrip. These connections are modeled using a thin wire which in FEKO cannot lie on a dielectric surface and must connect to a part of the microstrip that extends beyond the Duroid substrate. The helix is also connected with a thin wire since the height of the first turn above the ground plane is slightly larger than the 1/4-inch substrate thickness (Fig. 6(b)).

These ports are driven simultaneously or individually to demonstrate different excitation options. Selected FEKO model results for both modes are shown where a passive splitter feed is modeled by exciting both antennas simultaneously with equal amplitude and phase. Wires wound for RHCP are used to model both the helical conductors in the same manner. For the desired segmentation the 1/4-inch conductor does not satisfy the thin wire approximation so a wire radius, $a = 0.1$ -inch rather than the actual, $a = 0.125$ -inch was used in simulations. In addition,

the uncertainty in the dielectric properties also contributes to the physical modeling error.



Fig. 6. Dual helix antenna (a) FEKO model with nylon supports and (b) impedance transformer input model.

III. WIDE-BAND OPERATION

When connected in parallel, the dual helix antenna has input resistance near 70Ω and could be driven with 50Ω source impedance. Such a connection complicates the fabrication and introduces parasitic reactance. To circumvent this problem, the simulation includes an impedance transformer on both inputs which are driven simultaneously. This two-port model then represents feeding both inputs with a splitter and matched cable lengths to be in-phase with equal amplitude. The results for the LFH helix (port 1) and the HFH helix (port 2) are shown in Figs. 7 and 8 respectively. The wideband helix with dielectric loading is reasonably well matched to 50Ω , but the patterns become corrupt at higher frequency having reduced gain on boresight owing to a tilted or split main beam.

The realized gain on boresight (in dBic) versus frequency is shown in Fig. 9. Without dielectric loading, the results indicate only a small dip in the boresight gain near 1.2 GHz. This dip is similar to the HFH only simulation (see Fig. 3). With dielectric loading this boresight null increases and is shifted to near 1.4 GHz. At this frequency the wideband antenna has 79% efficiency with $\sim 12\%$ dielectric losses compared to the no dielectric case with 87% efficiency from mismatch loss. With increasing frequency the boresight gain drops due to a combination of dielectric losses and the onset of the HFH conical mode radiation. The null on boresight near 1.4 GHz is not nearly the pattern perturbation associated with the ground plane edge as in the HFH alone (Fig. 4). This frequency dependence appears to be a combination of mutual

coupling and dielectric loading effects which reduces the antenna efficiency and at some frequencies leads to a split main beam.

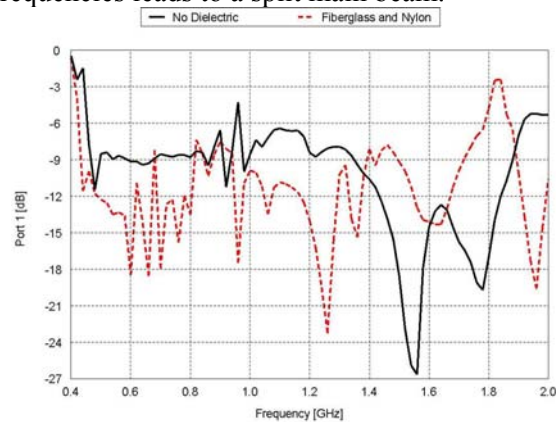


Fig. 7. Calculated S_{11} for the wideband helix antenna with and without dielectric loading.

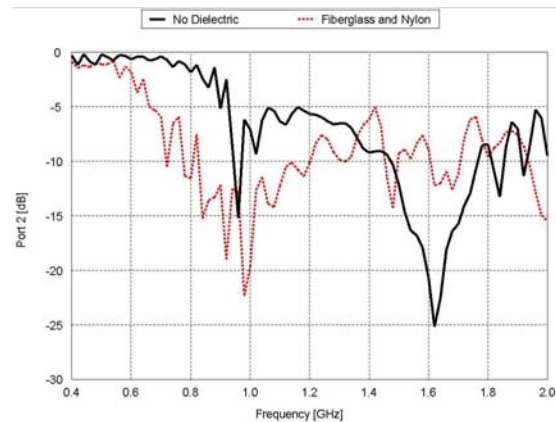


Fig. 8. Calculated S_{22} for the wideband helix antenna with and without dielectric loading.

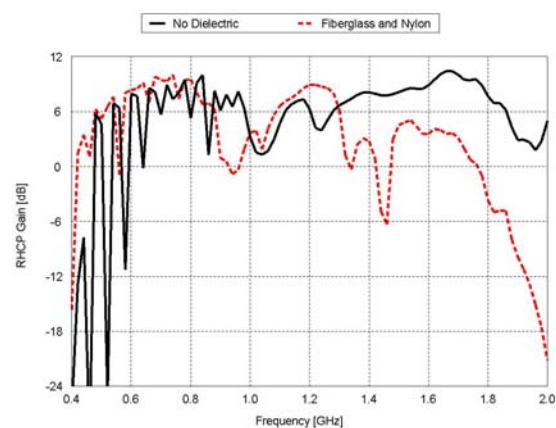


Fig. 9. Calculated RHCP realized gain for the wideband helix antenna on boresight.

The RHCP patterns at selected frequencies are shown in Fig. 10 with dielectrics included showing the off-boresight radiation at some frequencies. The patterns have more side lobes and back lobes than a single helical antenna. For wideband operation a microstrip corporate feed system could be designed to fit in the available space remaining on the ground plane. The opposed arrangement of the feed points, which for the HFH must then protrude through the outer nylon base (see Fig. 6), makes such a design complicated and was not pursued.

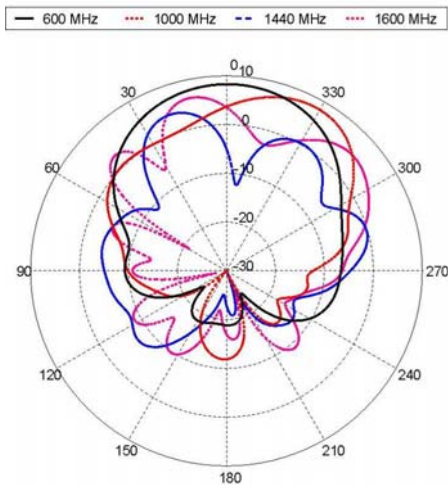


Fig. 10. Calculated RHCP realized gain patterns for the wideband helix antenna.

IV. DUAL-BAND OPERATION

The coaxial helical antenna could also be operated as a dual-band antenna using a microstrip transformer on each helix to provide two 50 Ω input ports. In this configuration, each port is driven separately, with the other port terminated into 50 Ω and the plotted simulation results overlap from 900 – 1100 MHz. The calculated S-parameters are shown in Fig. 11 with the fiberglass coating and nylon support structures. As with the high frequency helix by itself, including dielectrics with the dual helix improves the return loss somewhat. Thus, the antennas could be switched at 900 MHz and maintain reasonable return loss over the entire 500 – 1600 MHz BW. The isolation (S_{12}) between these antennas is not very good over most of the frequency band with the strongest coupling in the low frequency region where only the LFH is excited. Only an opposed

feed arrangement was investigated, so this geometry may not be optimum and is an area for future study.

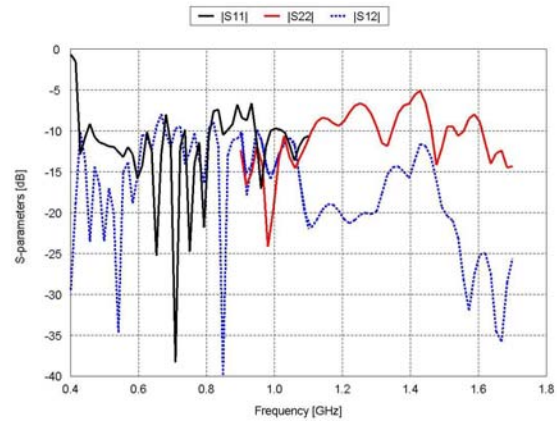


Fig. 11. Calculated S-parameters for the dual-band helix antenna with dielectric loading.

The realized gain versus frequency on boresight is shown in Fig. 12 (with and without the nylon support structures) showing the overlapping performance around 1 GHz. The gain BW has a gap with reduced gain from 900 – 1100 MHz even though the impedance BW indicates better performance. This is because both the LFH and HFH peak gain is reduced and can be off-boresight in the frequency range near the band edges. Similarly, the HFH peak gain is off-boresight at some frequencies with a split main beam near 1450 MHz. Example patterns for the original model with the fiberglass coating and nylon structures included are shown in Fig. 13.

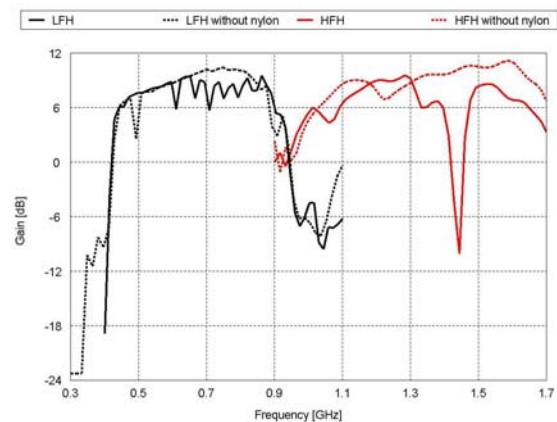


Fig. 12. Calculated RHCP realized gain for the dual-band antenna with and without nylon base.

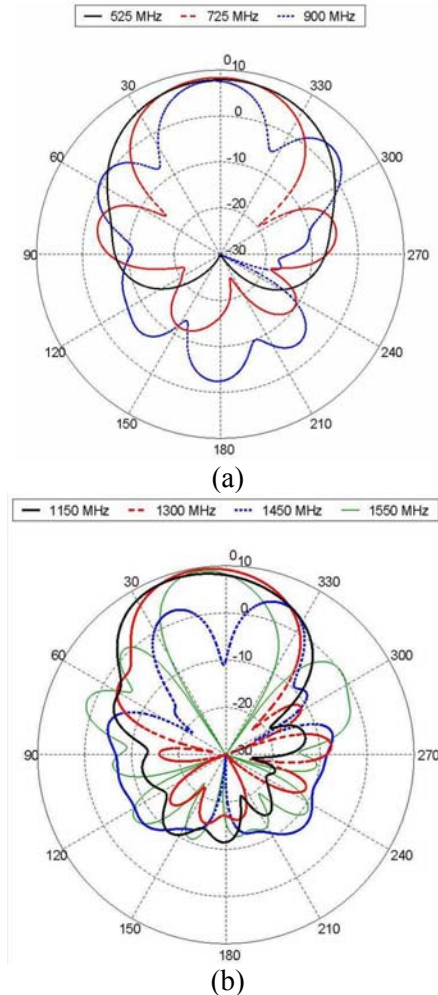


Fig. 13. Calculated RHCP radiation patterns for the dual-band helix antenna with dielectric loading for the (a) LFH driven and the (b) HFH driven.

Several methods of feeding the HFH were evaluated empirically and most techniques were found to introduce unwanted inductance. The best method installed the connector underneath and as close as possible to the transformer in order to avoid any wire connections. With this approach, the antenna input impedance is marginal but the results encourage further optimization. The dielectric support structures, the location of the feed regions and the ground plane edge height are all design features that this study found to impact performance. Future efforts can attempt to optimize such features both individually and in combination to improve the results shown here.

Nylon in the feed region has a large detrimental effect on the HFH performance. To

further investigate this influence, the LFH transformer was removed so this port is open-circuited. This baseline model runs faster while still having the dominant features of the boresight gain versus frequency as in Fig. 12. However, the split beam at some frequencies is not observed for the LFH open-circuit implying that this pattern perturbation is a mutual coupling effect when the non-driven port is terminated. We investigated variations of the simplified model in an attempt to identify design parameters that have the largest impact on performance. Two such variations are summarized here. First, the height of the nylon supports is reduced by a factor of two (1.5-inch). Then the ground plane edge height is also reduced by a factor of two (2.11-inch). The comparison is shown in Fig. 14 for the boresight gain versus frequency indicating that the dielectric loading in the HFH feed region is the primary cause of the reduced gain on boresight near 1460 MHz. The input impedance mismatch dominates the antenna efficiency where the loss in the nylon is larger than that in the coated wires. The baseline model is only 4% less efficient, but the dielectric loading tilts the beam off boresight at some frequencies.

Radiation patterns for the baseline model compared to these two variations are shown in Fig. 15 at 1460 MHz. Notice that the baseline model with the LFH open-circuit has a tilted rather than split beam with >6 dBic main beam gain reduction. This numerical study indicates that a smaller or different dielectric support structure should be considered after which the ground plane design can be optimized for dual-band operation.

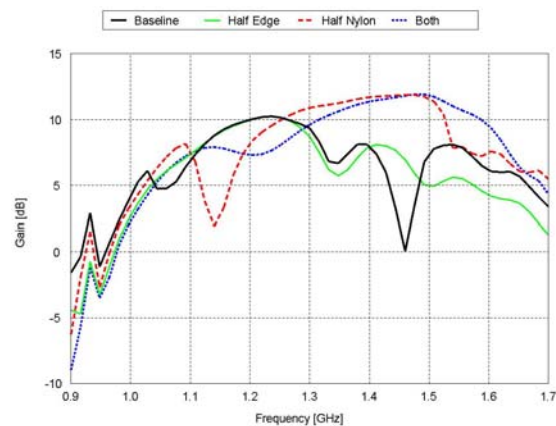


Fig. 14. Calculated RHCP realized gain on boresight with the LFH open-circuit.

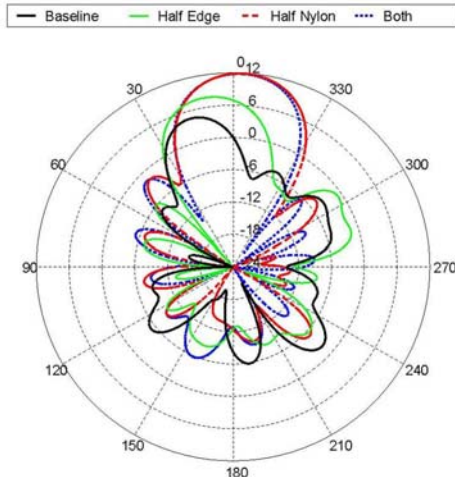


Fig. 15. Calculated RHCP patterns with the LFH open-circuit at 1460 MHz.

As an example of design improvements, the ground plane edge and nylon base heights are both reduced by a factor of two in the dual-band helix model. This simulation confirms that design changes which improved the HFH boresight gain are not detrimental to the LFH performance. The return loss and boresight gain comparisons for the original and revised design are shown in Figs. 16 and 17 respectively. The results indicate that dielectric loading is an important parameter for the antenna input impedance. Less nylon improves the LFH and HFH efficiency over most of their in-band frequencies. At 1428 MHz the efficiency increases by 30% when reducing the nylon and edge height owing in part to 11% less loss in the nylon. Less nylon in the HFH feed region and reduced edge height also improves the input impedance mismatch by 19% with less pattern perturbations compared to the original model.

Pattern comparisons at selected frequencies are shown in Fig. 18. Obviously, these changes improved the design and will be the basis for further optimization. Additional tradeoff studies in the materials selected for the helix supporting structures can be conducted numerically. Further optimization of the feed region details and ground plane design could lead to additional performance improvements.

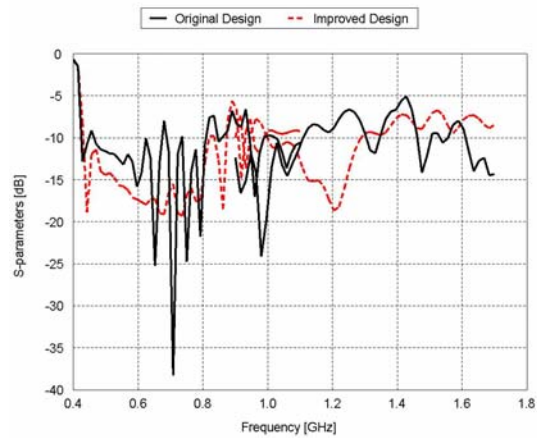


Fig. 16. Calculated S-parameters for the original and revised dual-helix antenna designs.

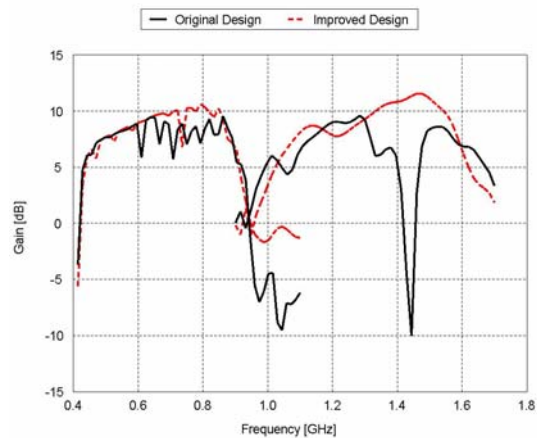


Fig. 17. Calculated RHCP realized gain on boresight for the original and revised design.

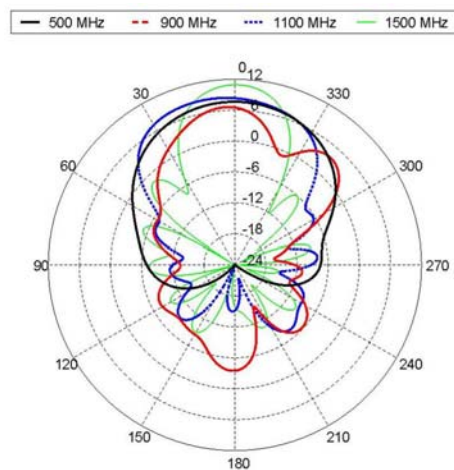


Fig. 18. Calculated RHCP radiation patterns for the improved dual-band helix design.

V. CONCLUSIONS

The results shown for the wideband and dual-band approaches encourage further virtual prototyping and prototype fabrication for model validation. Both approaches have reasonable performance; however, at frequencies near the band edges the peak gain can be $15^\circ - 30^\circ$ degrees off-boresight. A null in the boresight gain near 1200 MHz is observed with the HFH only which depends on the ground plane edge height as can be seen in Fig. 5. The ground plane design was based on an optimum quarter-wave edge height [1] for the LFH but reduced the boresight gain at some frequencies for the HFH alone.

The numerical study progressed from simple models of the HFH only to the LFH/HFH coaxial antenna while including more feed region details and dielectric structures subject to the FEKO approximations and limitations. It was found that even for thin fiberglass the dielectric loading was an important effect tending to shift the antenna impedance and gain BW to lower frequencies with reduced gain at high frequency. The influence of the nylon base supports significantly impacted the antenna performance introducing more frequency dependence, reduced boresight gain, and perturbed radiation patterns. The model could be refined even further by using measured dielectric properties as a function of frequency. However, the helical conductors embedded in thin fiberglass cannot be modeled exactly. Rather, the coated wire approximation is used because it is efficient and approximates measured results.

The dual-band model has two feed regions with transformers in opposed positions with the Duroid and nylon modeled using the FEM. This represents more accuracy but requires more computational resources and takes ~10 minutes per frequency or roughly 6 hours per simulation. The dual-band simulation requires two runs with overlapping frequencies to excite each port separately. Results over the full BW require ~12.5 hours. When driven simultaneously, the simulation time is reduced but the results have limited utility since such an idealized input model is difficult to achieve in practice.

The coaxial helix model was successfully used to investigate design improvements. It showed that by reducing the size of the nylon base plate and the ground plane edge height the antenna

performance can be improved. The model results indicate that fabrication alternatives can dramatically affect performance at high frequency. Even an approximate model is beneficial to evaluate relative differences in material selection and fabrication options compared to constructing and measuring multiple prototype antennas. Once validated to provide more confidence in the results, the FEKO model can be used to further optimize the dual-band antenna performance.

REFERENCES

- [1] H. E. King, J. L. Wong, and E.H. Newman, "Helical Antennas," *Antenna Engineering Handbook*, 4th Ed., J. L. Volakis (ed.), Chap. 12 (New York: McGraw-Hill, 2007).
- [2] W. Coburn, C. Ly, T. Burcham, R. Harris and A. Bamba, "Design and Fabrication of an Axial Mode Helical Antenna," Proceedings of the 2009 ACES Conference (March 2009).
- [3] J. R. Pierce and P. K. Tien, Coupling of Modes in Helices, Proceedings of the IRE, Vol. 42, pp. 1389–1396 (September 1954).
- [4] J. D. Kraus, "The Helical Antenna," *Antennas*, Chap. 7 (New York: McGraw-Hill, 1950).
- [5] R. B. Bossoli, "The Microwave Permittivity of Two Sprayable Resin Systems," U.S. Army Research Laboratory, ARL-TR-3907, September 2006.



William O'Keefe Coburn received his BS in Physics from Virginia Polytechnic Institute in 1984. He received an MSEE in Electro physics in 1991 and Doctor of Science in Electromagnetic Engineering from George Washington University (GWU) in 2005. He has 28 years experience as an electronics engineer at the Army Research Laboratory (formerly the Harry Diamond Laboratories) primarily in the area of CEM for EMP coupling/hardening, HPM and target signatures. He currently is in the RF Electronics Division of the Sensors and Electron Devices Directorate applying CEM tools for antenna design and analysis.

Analysis of Multi-Layer Composite Cavity Using FEKO

James E. Stanley¹, Dawn H. Trout², Susan K. Earles¹, Ivica N. Kostanic¹,
and Parveen F. Wahid²

¹ Department of Electrical and Computer Engineering
Florida Institute of Technology, Melbourne, FL 32901. USA
jes@fit.edu , earles@fit.edu , kostanic@fit.edu

² School of Electrical Engineering and Computer Science
University of Central Florida, Orlando, FL 32816-2450, USA
dawn.h.trout@knights.ucf.edu , wahid@mail.ucf.edu

Abstract— Modeling of a large cavity containing multiple layers inside the structure has been studied using equivalent impedance approximations along with simplified single ray tracing analysis. This modeling effort investigates the effects of radiating with a source enclosed in a large vacant composite structure relative to a short wavelength. The development of the model involves the completion of a two step process. First, the heritage geometric reduction and approximation is investigated. This particular investigation involves an approach that is an application of Poynting's Theorem. This work was performed by Hallett and Reddell at Goddard Space Flight Center in 1998. For this comparison, the Multi-Level Fast Multipole Method (MLFMM) available in the commercial tool FEKO, is used to model a generic multi-layer payload fairing (hollow cone connected to a hollow cylinder) with a radiating source to determine the resonant cavity effects within the fairing as another approximation baseline. The intent is to provide predictions for the electric field levels if a transmitter in the fairing either deliberately or unintentionally is activated. The results show a comparison with the heritage calculation and FEKO software tool. However, FEKO shows the electric field distributions within the composite fairing cavity instead of a single average value.

Index Terms— Inhibits, Resonant Cavity, FEKO, EM Compatibility

I. INTRODUCTION

Monitoring the status of spacecraft through direct transmission while it resides within the payload fairing, or loaded cavity, of a launch vehicle is prohibited through the use of inhibitors, but sometimes radiating within the cavity is a mission requirement. In general, radiating within the cavity has been a desire of many space missions either for spacecraft function monitoring or to prevent the reliability issues that inhibitors cause. For this desire to become a realization, the spacecraft must power on its transmitter while encapsulated within the payload fairing. If power were applied, the electric field levels would expose both the spacecraft and launch vehicle to levels well beyond the avionics qualification levels that are typically tailored from MIL-STD-461 [1] and MIL-STD-1541 [2]. In the past, the fairings were made entirely of aluminum and provided protection for the spacecraft much like a Faraday cage [3]. Unfortunately, along with protecting the spacecraft from unwanted sources external to the fairing, energy from internal transmitters is trapped inside the fairing. With the advent of composite structures and more precisely with the build up of composite fairings, the space industry performed several tests and rough calculations as documented by Hallett and Redell [4] to determine the effects of radiating within the new composite fairing structure. In this work, it is desired to determine the radiation distribution inside the composite fairing structure. A multi-layer payload fairing is modeled using two techniques: an application of Poynting's Theorem that will be referred to as the heritage method and a commercial tool, FEKO. FEKO is a Computational ElectroMagnetic software tool, EM Software

Systems -S.A. FEKO. FEKO allows the use of Physical Optics (PO), Method of Moments (MoM), Multi-Level Fast Multipole Method (MLFMM) and Hybrid MoM/PO techniques. Due to the nature of the composite and FEKO functionality, MLFMM is used. The results of the two techniques are presented and compared. The heritage method was first performed at Goddard Space Flight Center in 1998. This effort is an extension of that heritage work. Only the geometric representation of the fairing is now characterized as a hollow cone connected to a hollow cylinder. In addition, the impedance was altered from the heritage calculations. The rationale for changing the geometry and impedance is due to the proprietary nature of the original fairing designs and materials used. It has been the desire of the space industry that a comprehensive model be developed to provide a better understanding of radiating within the acoustic blanket lined composite fairing, or cavity.

II. PROBLEM DESCRIPTION

The interior walls of the composite fairings were lined with Dupont's Kapton 377[®] "blankets". The blankets consist of a layer of Kapton film overlaid onto melamine foam with another layer of Kapton film as seen in Fig. 1. The original intent was to provide protection as acoustic blankets or shields. In the process, it also reduced the interior volume of the fairing. Some experimental studies were performed to determine the effect of having both the acoustic blankets lining and a new composite fairing structure [4]. The actual levels predicted and measured are a matter of some debate even today. Some of the concerns include testing with antennas that are not utilized during a mission as well as the simplistic analytical methods used to predict the electric fields within the cavity. In order to minimize mission risk, the respective spacecraft are not permitted to radiate within the fairing cavity unless adequate mission specific analysis is performed to show electromagnetic compatibility without transmission inhibits.

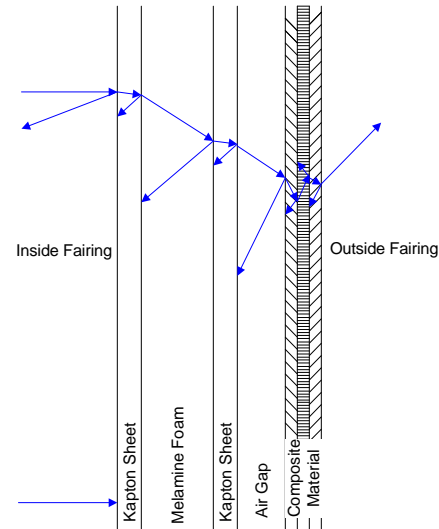


Fig. 1. Multi-layer composite cavity (fairing wall).

The plan for developing and comparing the respective models is broken into two components:

Heritage Geometric Reduction and Approximation

Using a direct application of Poynting's Theorem, the electric field levels using the first analytical technique from Hallett and Redell [4] are calculated. An equivalent impedance is used as illustrated for the 5 - 6 GHz range in Fig 2. However, the geometry is a hollow cylinder connected to a hollow cone as shown in Fig. 4 below. The other parameters found in the open literature will remain the same.

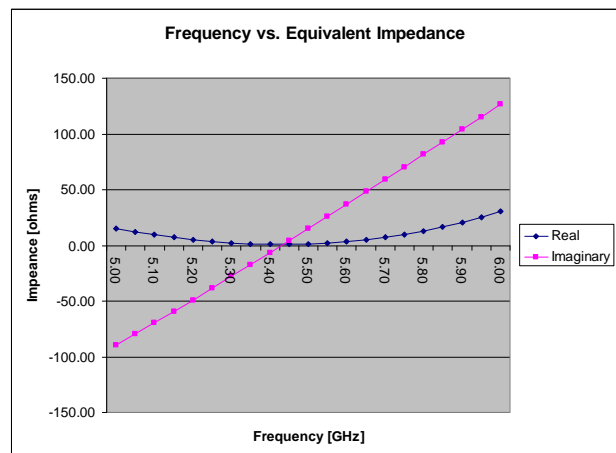


Fig. 2. Equivalent impedance of multi-layer composite cavity (fairing wall).

The values calculated with this method are worst case average approximations of the electric field within the cavity where only one level is obtained at each frequency. This level is used as a baseline value for comparison. This approximation is used as a quick worst case prediction as seen in Fig. 2 below.

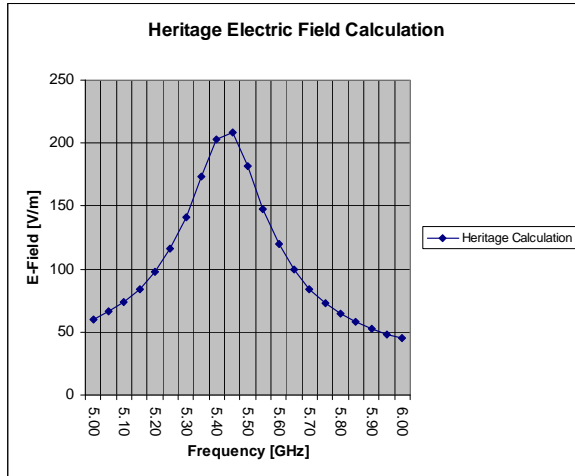


Fig. 2. Heritage electric field calculation.

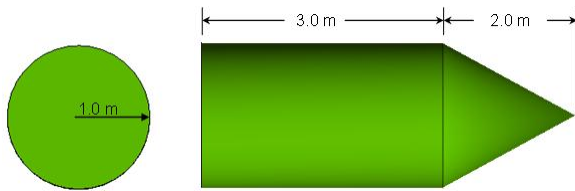


Fig. 3. Cavity geometry.

FEKO Computational Analysis

A model with a hollow cylinder connected to a hollow cone with a horn antenna pattern in FEKO CEM software is implemented (Fig. 3). The prior equivalent impedance approximation is used to account for the losses, and the electric fields within the cavity are determined. The distribution of the electric field is found. The implementation of the model in FEKO requires that the geometry is created with primitive elements of the graphical tool and an equivalent impedance that was previously calculated is placed at the inside surface of the cavity as an infinitely thin sheet for the mesh of the geometry. The sources are implemented as a

point source with a horn antenna pattern. The MLFMM technique is used in FEKO. The model parameters include a transmitter frequency of 5, 5.2, 5.4, 5.6, 5.8, and 6 GHz, input power of 10 Watts, and an antenna pattern for an EMCO 3115 antenna pattern. In this example, observation points were chosen at the locations of two center-line planes along x-z and y-z, respectively.

III. NUMERICAL RESULTS

From Hallett and Reddell [4], the equivalent impedance is calculated using Eq. (1) and the electric field is calculated from the incident power using Eq. (2) as seen below. A description of the pertinent variables follows Eq. (2), respectively.

The electric field found with the heritage calculation method provides a maximum value of 60 V/m at 5 GHz.

Using FEKO, the MLFMM approximation is implemented to create the electric field distribution at 5 GHz shown below in Fig. 4. As shown, the maximum values (330 V/m) are much higher when compared to the maximum value (60 V/m) provided in the heritage calculation. While the heritage calculation only provides the singular estimate relative to the surface area of the cavity, the MLFMM technique shows the distribution of the electric field inside the fairing. The heritage calculation is within the FEKO data range.

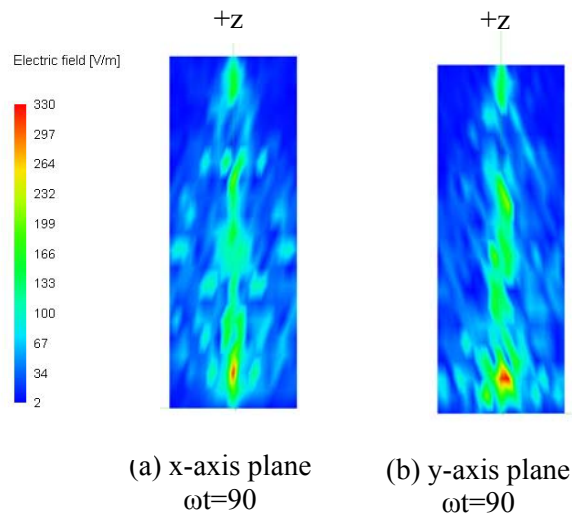


Fig. 4. FEKO calculations at cross-sections along the x- and y- axes.

$$\eta_L(l) = \eta_1 \left\{ \frac{\left[(\eta_2 + \eta_1)e^{\alpha_1 l} + (\eta_2 - \eta_1)e^{-\alpha_1 l} \right] \cos \beta_1 l + j \left[(\eta_2 + \eta_1)e^{\alpha_1 l} - (\eta_2 - \eta_1)e^{-\alpha_1 l} \right] \sin \beta_1 l}{\left[(\eta_2 + \eta_1)e^{\alpha_1 l} - (\eta_2 - \eta_1)e^{-\alpha_1 l} \right] \cos \beta_1 l + j \left[(\eta_2 + \eta_1)e^{\alpha_1 l} + (\eta_2 - \eta_1)e^{-\alpha_1 l} \right] \sin \beta_1 l} \right\} \quad (1)$$

$$\vec{E}_0^{inci} = \sqrt{\frac{P_T^{inci}}{\sum_{i=0}^k \left((2SA_i) \operatorname{real} \left\{ \left| \frac{\eta_i}{\eta_0 + \eta_i} \right|^2 \right\} \right)}} \quad (2)$$

where:

- η is the impedance of the media.
- α is the attenuation constant of the media.
- β is the phase shift constant of the media.
- l is the length (thickness) of the media.

Similarly for the remainder of the frequencies of interest (5.2, 5.4, 5.6, 5.8, 6.0 GHz), the results were similarly distributed for the respective curves. The comparison of the results for these curves is shown in Fig. 5. below. In future calculations, the work of Demir and Elsherbeni [6] will be taken under consideration for the calculation of the layered media relative to the blanket and composites in free space.

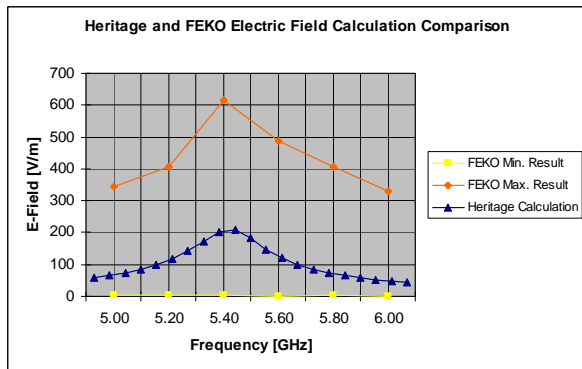


Fig. 5. Heritage and FEKO electrical field calculation comparison.

IV. CONCLUSIONS

The MLFMM technique in FEKO and Heritage Calculation estimated the maximum

electric field 330 V/m and 60 V/m, respectively, within the cavity at 5 GHz. Additionally, values for the other frequencies of interest were compared to heritage calculations. The distribution of the field predicted by FEKO provides added information when compared to the location of critical launch vehicle avionics and spacecraft components. This allows the mission managers to assess risk relative to electromagnetic compatibility, and the analysis provides insight regarding cavity resonances as a “radiated environment” within the cavity. Although this maximum value prediction of the heritage method is shown to be within the range of the FEKO values, it could also drive sensitive spacecraft equipment to test to levels not indicative to the actual RF environment.

REFERENCES

- [1] Department of Defense (U.S.), “Electromagnetic Emission and Susceptibility Requirements for the Control of Electro-magnetic Interference,” MIL-STD-461C, 17 Feb 1996.
- [2] Department of Defense (U.S.), “Electromagnetic Compatibility for Space Systems,” MIL-STD-1541A, 30 Dec 1987.
- [3] C. R. Paul, *Electromagnetics for Engineers With Applications*, John Wiley & Sons, New York, NY, 2004.
- [4] M. Hallett and J. Reddell, “Technique for Predicting the RF Field Strength Inside an Enclosure,” Technical Report NASA/TP-1998-206864, NASA Aeronautics and Space Database, Goddard Space Flight Center, Greenbelt Maryland, 1998.
- [5] D.K. Cheng, *Field and Wave Electromagnetics*, Second Edition, Addison Wesley, Reading, MA, 1989.
- [6] V. Demir and A. Elsherbeni, “A Graphical User Interface for Calculation of the Reflection and Transmission Coefficients of a Layered Medium,” *IEEE Antennas and Propagation Magazine*, Vol. 48, No. 1, February 2006.



James E. Stanley received his B.E.E. from Auburn University in 1988 and his Masters of Science in Engineering (Electrical Engineering) from Mercer University in 1997. He is currently pursuing his Ph.D. in Electrical Engineering at Florida Institute of Technology. He has

worked in DoD on multiple airframes and subsystems. After moving to the commercial sector with General Electric and communication companies, he is contributing to the Qinetiq-North America team as a NASA contractor.

For the last five years James has been the lead in electromagnetic analysis for the Kennedy Space Center Launch Services Program. He has received numerous commendations for bringing the Electromagnetic Compatibility Team from a purely back-of-the-envelope approach to one with intensive numerical analytical analysis capability. His skills are increasingly in demand to evaluate mission integration issues with antennas in cavities. He has done extensive research on layered materials and modeling these layers with impedance sheets. He also has expertise in developing computer systems and writing electromagnetic modeling codes.



Dawn H. Trout received her B.S. degree in Electrical Engineering from Memphis State University in 1989 and her Masters in Electrical Engineering from the University of Alabama in

Huntsville in 1995. She has worked at NASA in the area of Electromagnetic compatibility for twenty years. The majority of this time she has spent leading the electromagnetic teams at Marshall Space Flight Center in Alabama and later at Kennedy Space Center in Florida.

She has served on multiple EMC standards committees and led the development of ISO 14302, Electromagnetic Compatibility, Space Systems Standard for which she received an AIAA award. She is currently pursuing her PhD

in Electrical Engineering at University of Central Florida through the Kennedy Space Center Graduate Fellowship Program. She has initiated multiple electromagnetic related studies in her career and her current research interests include electromagnetic fields in large composite cavities and indirect lightning effects.



Dr Ivica Kostanic was born in 1968 in Belgrade, Yugoslavia. He obtained BSEE, MSEE and PhD from Belgrade University, Florida Institute of Technology and University of Central Florida

respectively. His principal research interests include various topics in radio communication, cellular systems and wireless sensor networks.

Currently, he is a faculty member in Electrical and Computer Engineering of Florida Institute of Technology where he teaches courses related wireless communication, personal communication and microwave circuit design. He is the technical director of Wireless Center of Excellence (WiCE) which is a group at Florida Tech dedicated to promoting research in wireless communication and computing technologies. Dr. Kostanic is a member of IEEE Communication Society.



Dr. Susan Earles is an Associate Professor in Electrical and Computer Engineering at Florida Institute of Technology. She was awarded a PhD degree in 2002 in Electrical Engineering

with a minor in Materials Science from the University of Florida. She has an MS and BS degree in Electrical Engineering from the University of Florida as well. Currently, she teaches courses related to Electronics and Semiconductor Device Theory. Her research involves simulation of lightning phenomena and characterization of changes in electronic materials and devices resulting from external perturbation due to various sources. She is also

the director of the microelectronics fabrication laboratory at FIT.



Dr. Parveen F. Wahid

received her B.S. degree in Mathematics and Physics in 1969, her M.S. degree in Physics from the University of Mysore, India in 1971 and her Ph.D. in Electrical Communication

Engineering from the Indian Institute of Science, India, in 1979. She was a Research Associate at the Electrical Engineering Department, University of Utah from 1980-1982 and at the Electrical Engineering Department, University of Nebraska, Lincoln from 1982-1983. Since 1984 she has been with the University of Central Florida, where she is now a Professor in the department of Electrical Engineering. She teaches electromagnetics, antenna theory and design and microwave engineering courses. Her research interests are in the area of the design of microstrip antennas and arrays and adaptive arrays for wireless applications and she has over 50 technical publications.

In 1989 Dr. Wahid was named the Tau Beta Pi Professor of the Year. She received the College of Engineering Excellence in Teaching Award in 1994 and 1999. In 1991 she received the University of Central Florida Excellence in Advising Award and in 1997 the University of Central Florida Excellence in Professional Service Award. In 2000 she was awarded the IEEE Region 3 Outstanding Engineer Educator Award and the IEEE Florida Council Outstanding Educator Award. She is a recipient of the IEEE Millennium Award.

She was the Technical Program Chair for the 1999 IEEE International AP/URSI symposium and the General Chair for the 1998 IEEE Region 3 Southeastcon conference. She has served many times on the technical program committee for the IEEE AP/URSI conferences. Dr. Wahid is a Senior Member of the IEEE and a member of the Eta Kappa Nu and the Tau Beta Pi Societies.

Calibration and Evaluation of Body Interaction Effects for the Enhancement of a Body-Borne Radio Direction Finding System

Arian Lalezari^{1,2}, Farzin Lalezari² and Dejan S. Filipović¹

¹ Department of Electrical and Computer Engineering,
University of Colorado, Boulder, CO 80309-0425, USA
lalezari@colorado.edu, dejan@colorado.edu

² FIRST RF Corporation, Boulder, CO 80301-2307, USA
alalezari@firstrf.com

Abstract: A method of moments (MoM) based computational study and design of a body-borne direction finding (DF) system is investigated in this paper. A baseline two-sensor DF system is established, and the performance of this system is characterized with measurements and simulation. A cylindrical human body model is then introduced to the system as a passive scatterer. Computer models of the body-borne system are validated using measurements with a prototype human body phantom. A parametric system response study is performed on the most important model variables to identify system stability. A discussion is presented on how these data may be applied to a direction finding function to generate a direction finding solution. This work clearly demonstrates the ability of modern computational electromagnetics tools to accurately and efficiently predict the response of complex physical systems.

Keywords: Direction Finding, Geolocation, Body Interaction, Computational Electromagnetics, FEKO Calibration.

I. INTRODUCTION

Technologies utilizing wireless links are simultaneously growing smaller, more prolific, and operating across larger portions of the radio frequency (RF) spectrum. To identify and locate these devices, there is a corresponding demand from commercial, consumer, and military users for direction finding (DF) and geolocation capabilities that match these trends in size, capability, and bandwidth. To address a further demand for mobility,

there is specific interest in extending these capabilities to individual users in body-borne or body-worn systems.

Direction finding techniques have been used in the radio band for almost as long as communications. Several phase-based, amplitude-based, and complex (phase and amplitude) DF techniques exist, and are well-summarized in [1]. Although maritime direction finding techniques were well established as early as 1925 [2], the application of these technologies increased considerably during World War II [3]. Several radio navigation systems including the VHF omni-directional radio range (VOR), Tactical Air Navigation (Tacan), Instrument Landing System (ILS), and Microwave Landing System (MLS) are direct results of these technologies [4]. In these systems, the signals of interest are beacons with characteristics that are known *a priori*, and are used to identify and locate the signal [5].

In this paper, a two-element antenna system is evaluated for application to broadband (100-750 MHz) body-borne radio direction finding and geolocation of unknown signals. In the past, multiple sensors or unique signal characteristics have been required to obtain unambiguous direction finding solutions. In this paper, a baseline two-sensor system is established, and its performance is simulated with EMSS FEKO [6], and validated with measurements. To understand body-borne performance, a passive scatter, the human body, is introduced to the system. Using a cylindrical human body model, the effects of this scatterer on the sensors of the DF system are characterized and validated with measurements of a prototype body phantom. The impact of the human body on the phase and amplitude of the direction finding system response is characterized as a function of frequency and angle of arrival.

After a thorough characterization of the baseline human body model, a multi-variable system response study is used to evaluate the changes of the phase and amplitude of the detected signal in the body-borne environment. In total, twelve system parameters, arranged into four categories (radiator, body, system, and excitation parameters) are studied. Using these data, practical frequency-independent phase and amplitude perturbation thresholds are established for differentiating between system variability and viable signal detections. Using these thresholds, an auto-correlating direction finding function (DFF) [7] to demonstrate how the phase and amplitude measurements of the system can be used to produce direction finding solutions.

By computationally evaluating the performance of a body-borne direction finding system in this paper, several contributions have been made:

- Full-wave simulation of a body-borne radio direction finding system, including sensor performance.
- Broadband characterization of platform interaction effects on a multi-sensor direction finding system using computational modeling.
- Validation of computer models with measurements from physical prototypes.
- Completion of a computational multi-variable parametric system response study to characterize system performance.
- Demonstration of a technique to use the results of the parametric study to establish amplitude and phase thresholds to differentiate between normal system perturbation and signal detections.
- Adaptation and application of an auto-correlating direction finding function to exploit platform interaction effects to generate direction finding solutions.

The remainder of this paper is arranged as follows. In Section II, the baseline two-sensor direction finding system is established, and free-space and body-borne simulations are validated with measurements. The results of a parametric system response study are provided in Section III. Using these data, frequency-independent thresholds are established to differentiate between normal system dynamics and detectable differences in incoming signals. In Section IV, a direction finding function (DFF) is adapted from the literature to demonstrate how these data can be applied to generate phase and amplitude based direction finding systems. Conclusions and future work are summarized in Section V.

II. MODELING

To model a body-borne direction finding system, a two-antenna sensor array is mounted on a cylindrical human body model, as shown in Figure 1(a). In order

to satisfy a backpack-mounted integration, the height of the antennas, represented as h , is selected to be 20". Likewise, the spacing between the elements along the y-axis is represented as d , and is selected to be 20".

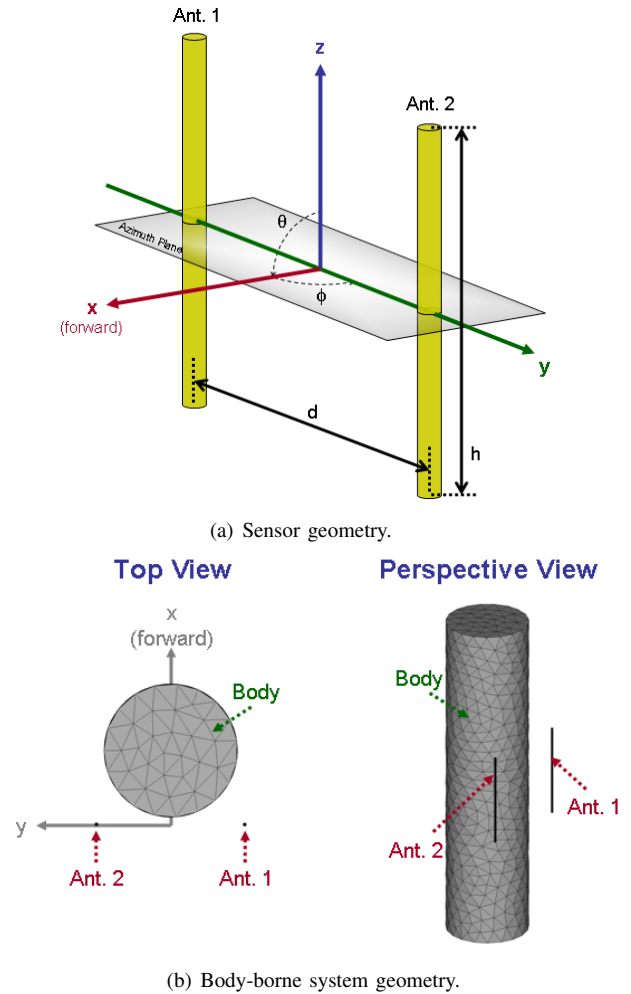


Figure 1. Direction finding system geometry.

A. Human Body Model

As seen in Figure 1(b), a commonly used cylindrical human body phantom [8], [9], [10] is adopted in this paper. A dielectric model for this phantom is consistent with the available data at about 300 MHz [11]. This is approximately the geometric mean frequency of the band of interest ($\sqrt{100 \times 750} = 273.9 \approx 300$). A dielectric constant of $\epsilon_r = 60$ and an electrical conductivity of $\sigma = 0.9$ S/m are chosen. The cylinder has an 18" diameter and is 6' tall. To represent a realistic body integration scheme, the axis of the cylinder is offset by 10" in the positive x-axis (forward) from the center of the antennas. The body model is aligned with the center of the antennas in the y-axis. The antennas and body model are oriented along the z-axis.

B. Modeling

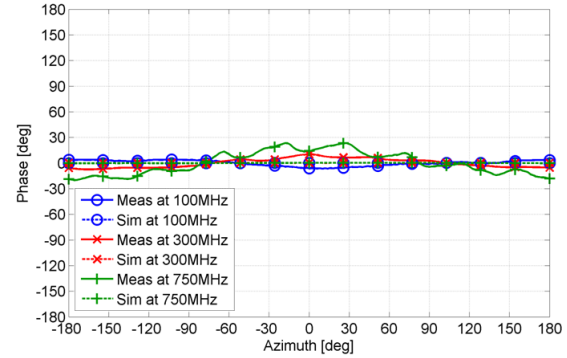
The body-borne direction finding system is simulated using a method of moments code, EMSS FEKO [6]. To emulate operation of a direction finding system, the model is excited by incident plane waves. Signal frequencies from 100-750 MHz in steps of 50 MHz, and angles of arrival from $\phi = -180^\circ$ - 180° in steps of 5° , are used. All signals are incident from the azimuthal plane ($\theta = 90^\circ$). The two wire dipole antennas in the DF system are terminated with 50Ω loads. The phase and amplitude of the induced currents across these terminations are used to characterize the system response as a function of frequency and angle of arrival.

C. Validation

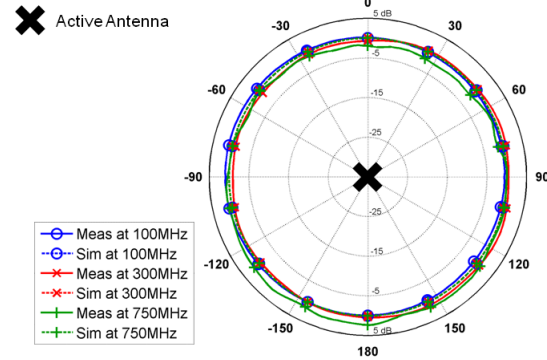
For initial modeling validation, the response of the direction finding system is tested in an anechoic chamber. Two center-fed 20" brass dipoles with a diameter of 0.2" are used with 50Ω printed baluns as the sensors. As in simulations, the antenna response is measured when excited by an incident wave. In these measurements, a broadband log-periodic (LP) source antenna is used. Due to anechoic chamber size limitations, only the 300-750 MHz band is measured.

To characterize the individual sensors, measurements of the free-space performance of a single antenna are taken across the band of interest. In FEKO, a wire antenna model is generated with the same height, and simulated across the same band of interest. The data from the measured and computer simulation tests in free space are shown in Figure 2(a) and 2(b) at three frequencies spanning the band of interest. As seen, good correlation between measurement and simulation is obtained. The observed disagreements are due to the effects of the baluns that are required in the measurements, but are excluded from simulation models.

The performance of the sensors in a two-element array configuration is also measured. As in the direction finding system, the reference point for these tests is the mid-point between the antennas. Accordingly, this reference is located along the axis of rotation in measurements, and at the origin in simulation. In this configuration, the antennas are located at $\pm 90^\circ$ in azimuth, as illustrated in Figure 1. Again, the antennas are characterized in free space, such that the only obstruction is the other antenna, which is terminated in a broadband resistive (50Ω) load. Received amplitude and phase data are gathered for both antennas, and measurements of the antenna located at 90° azimuth are presented in Figure 3(a) and 3(b). The antenna separation is $d/2 = 10''$ from the center of rotation, its received phase varies like $(d/2 \sin \phi)$, where ϕ is the azimuth angle. At the high end of the band, the magnitude of this variation is



(a) Free space phase.



(b) Free space amplitude.

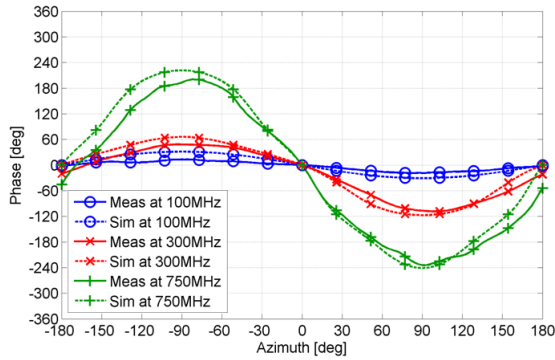
Figure 2. Free space single sensor validation.

approximately 240° , so the phase has been “unwrapped”, so that it may extend beyond $\pm 180^\circ$.

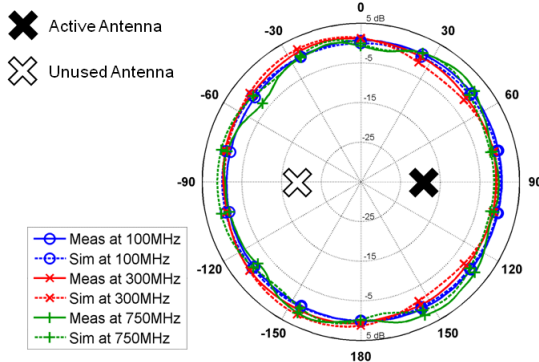
As in the single sensor simulations, there is excellent agreement between simulations and measurements. The spatial dependence exhibited by the system response in Figure 3 is of particular importance. It is this characteristic that will be exploited to generate a direction finding solution.

To evaluate MoM modeling with complex structures, a prototype cylindrical human body phantom is built and tested. Due to limited availability of parts, this model is built with a 12" diameter polyvinyl chloride (PVC) pipe, and is 5' tall. To emulate the dielectric properties (dielectric constant and conductivity) of the human body, a 1% salt water solution is used to fill the model [11]. Two center-fed 20" brass dipoles with a diameter of 0.2" are used with 50Ω printed baluns. The model is tested at an outdoor test facility using a monocone antenna as a source, as shown in Figure 4(a).

As seen in Figure 4(b), a computer model using a cylinder of the same size and shape as the test structure is used for validation. Because of its relatively low dielectric constant, the 0.4" PVC wall thickness is ignored in simulations. To compare the results of the measured and simulated experiments, the relative phase and amplitude



(a) Free space phase.



(b) Free space amplitude.

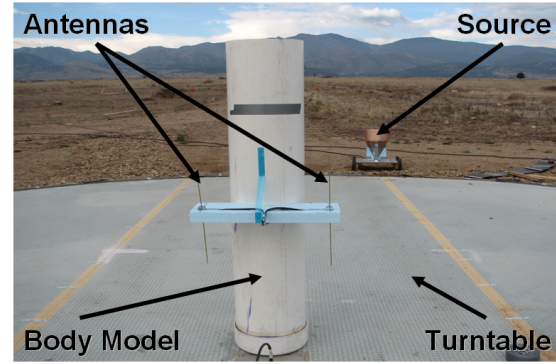
Figure 3. Free space sensor pair validation.

of signals detected by the two sensors in the system are recorded. Due to restrictions on test frequencies at the outdoor test facility, only the 200-600 MHz band is used. Accordingly, the phases and amplitudes of the system response, as a function of azimuth angle for three different frequencies, are shown in Figure 5.

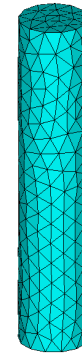
As seen, there is excellent agreement between measurement and simulation in the available part of the band for both the phase and amplitude of the response.

III. PARAMETRIC SYSTEM RESPONSE

While many of the parameters used in the baseline human body and antenna sensor models are favorable for modeling, they are a coarse representation of the real-world realization of the system. Accordingly, the remainder of this study explores the variations in system response to various geometric and model parameters. The objective is to understand how the behavior of the system might be impacted by real-world perturbations of system parameters, so the values by which they are perturbed are chosen to reflect conditions that might be encountered in different realized configurations and/or calibration setups of the system. To determine the variations of the data used by the direction finding system,



(a) Physical prototype test.



(b) Computer validation model.

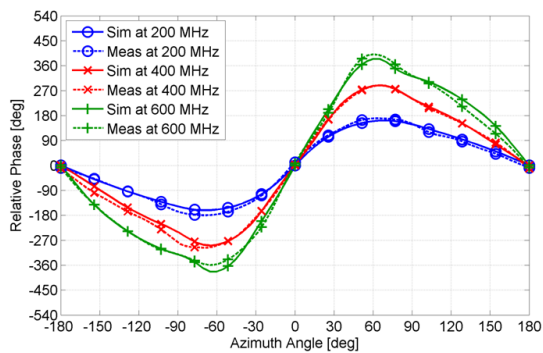
Figure 4. Modeling validation configurations.

twelve model parameters are selected. They are divided into four categories, summarized in I.

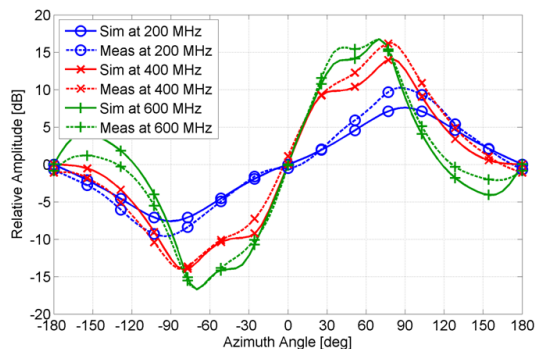
The alternate values for each of these variables are selected to represent changes to the system that might occur due to normal movement of the user. Accordingly, this study is intended to characterize how the phase and amplitude response of the direction finding system are impacted by normal use of the system. Based on these results, “detection thresholds” are selected. These thresholds allow the direction finding system to differentiate changes in phase and amplitude perturbations that are expected with normal system use from phase and amplitude changes associated with signals from different angles of incidence. That is, any phase and amplitude variation below these thresholds will be attributed to normal use and will establish the system uncertainty, while phase and amplitude differences above these thresholds will be used to differentiate larger changes in the system response, associated with the angle of incidence of an incoming signal. In all cases, at least three values of the variable are selected, mainly one above and one below the nominal configuration value. However, in some cases — when the model geometry precludes two-sided alternate configurations — two values that are both above or below the nominal variable are chosen.

Table I
TWELVE VARIABLE CONFIGURATIONS ARE STUDIED IN A PARAMETRIC STUDY.

Category	Variable	Nominal	Alternate	
Radiator Parameters	Radiator Height	20"	15"	25"
	Termination Impedance	50 Ω	25 Ω	75 Ω 100 Ω
Body Parameters	Body Diameter	18"	15"	12"
	Body Height	6'	5.5'	6.5'
	Body ϵ_r	60	20 40	80
System Parameters	Baseline Separation	20"	18"	22"
	Baseline Rotation	0 $^\circ$	5 $^\circ$	10 $^\circ$
	Antenna Z Position	0"	12"	24"
	Body X Position	10"	8"	12"
	Body Y Position	0"	1"	2"
Excitation Parameters	Signal Elevation	90 $^\circ$	105 $^\circ$	120 $^\circ$
	Signal Polarization	0 $^\circ$	45 $^\circ$	90 $^\circ$



(a) Relative phase of system response.



(b) Relative amplitude of system response.

Figure 5. Relative phase and amplitude data from modeling validation.

Frequency-dependent data from the conducted studies are provided for the raw phase and amplitude responses of the direction finding system. As previously shown, the system response at each frequency is a function of incident angle. To represent the distribution of the perturbation to this response across all angles of incidence effectively, these data must be consolidated. If the angular perturbations are considered to lie in some distribution, it is convenient to describe the shape and location of this distribution. Common statistical metrics

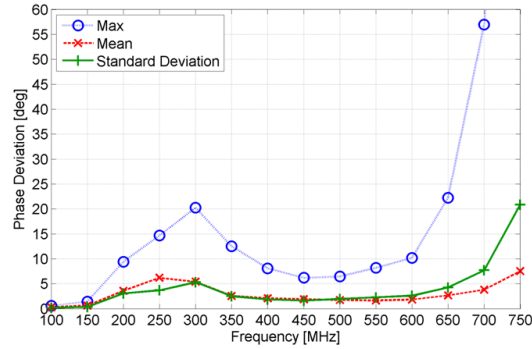
are used to describe the nominal perturbation (mean), the distribution of the perturbations (standard deviation), and their extent (maximum value) [12].

A. Radiator Parameters

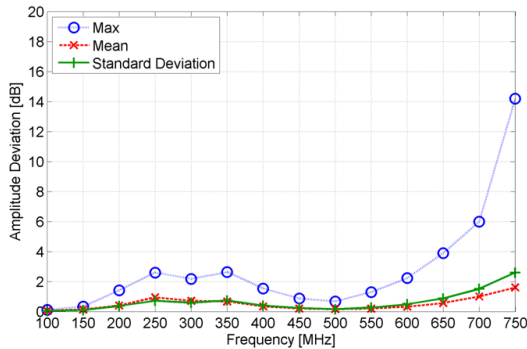
1) *Radiator Height*: As described in the previous section, the nominal radiator height is 20". To study the effects of this parameter on the amplitude and phase response of the system, antenna heights of 15" and 25" are compared to the nominal configuration. The frequency-dependent phase and amplitude response perturbations due to the varied radiator height are provided in Figure 6(a) and Figure 6(b), respectively.

Although it is unlikely that the size of the sensors used in any real-world implementation of this system would change length, it is not inconceivable (e.g. due to damage or improper repair or replacement). As previously discussed, the phase and amplitude of the received signal is dependent on the size and shape of these sensors. Accordingly, it is not surprising that there are significant changes in the response of the system when the sensor height is changed. At 15" and 25", the radiator is resonant at approximately 393 and 236 MHz, respectively. Not surprisingly, there is a correspondingly large perturbation in the system response around these frequencies. The largest perturbation, however, occurs at the high end of the frequency band, driven both by the electrical first anti-resonance of the smaller antenna and the second resonance of the larger antenna. As confirmed by these results, maintaining the expected system performance will be somewhat reliant on maintaining the size and integrity of the sensors.

2) *Radiator Termination Impedance*: The nominal radiator termination is 50 Ω . To study the effects of this parameter on the amplitude and phase response of the system, radiator terminations of 25 Ω , 75 Ω and 100 Ω are compared to the nominal configuration. The frequency-dependent phase and amplitude response perturbations



(a) Phase response perturbation.



(b) Amplitude response perturbation.

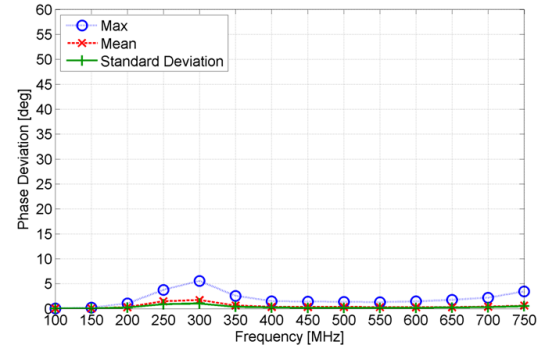
Figure 6. System response to variations of the radiator height.

due to the varied radiator termination are given in Figure 7(a) and Figure 7(b), respectively.

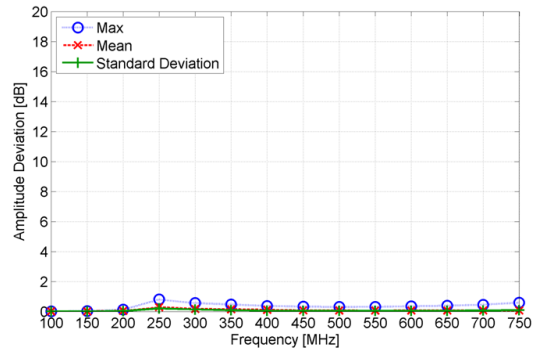
As previously discussed, the two-sensor system must necessarily use the relative amplitude and phase of the system response to generate a direction finding solution. The system response is collected from the currents excited across the terminated port of the antenna. These currents are proportional to the impedance, so it is not surprising that equally changing the termination impedance of both sensors produces almost no change in the system response, except near resonance, around 300 MHz. Near this frequency, the maximum phase deviation is approximately 5.5° , and the maximum amplitude deviation is approximately 0.8dB, indicating that the system is relatively insensitive to perturbations of this parameter.

B. Body Parameters

1) *Body Diameter:* The nominal body diameter is 18". To study the effects of this parameter on the amplitude and phase response of the system, body diameters of 15" and 12" are compared to the nominal configuration. The nominal spacing of the antennas is 20", so body diameters larger than 18" are not studied, as these would engulf the sensors. The frequency-dependent phase and



(a) Phase response perturbation.



(b) Amplitude response perturbation.

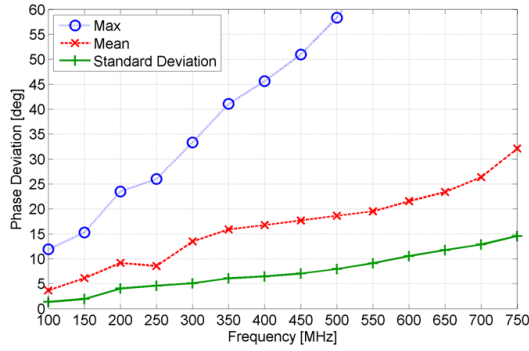
Figure 7. System response to variations of the radiator termination.

amplitude response perturbations due to the varied body diameter are provided in Figure 8(a) and Figure 8(b), respectively.

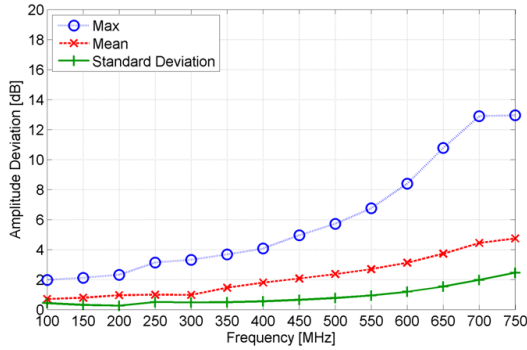
As seen, there is a frequency dependence on both the phase and amplitude perturbations. At 750 MHz, the maximum phase perturbation is approximately 115° , and the maximum amplitude perturbation is approximately 13dB. The standard deviations for these perturbations are approximately 14.5° and 2.5dB, respectively, indicating that the maximum perturbations are relatively rare, 5.7σ away from the mean for the phase and over 3.3σ away from the mean for the amplitude. Still, these results indicate that maintaining the expected system performance is reliant on characterizing the body diameter well, and that system calibration needs to be performed for each user.

2) *Body Height:* The nominal body height is 6'. To study the effects of this parameter on the amplitude and phase response of the system, body heights of 5.5' and 6.5' are compared to the nominal configuration. The body model was selected to represent a tall user, so body heights greater than 6.5' are not studied. The frequency-dependent phase and amplitude response perturbations due to the varied body height are provided in Figure 9(a) and Figure 9(b), respectively.

The frequency dependence of the perturbations due



(a) Phase response perturbation.



(b) Amplitude response perturbation.

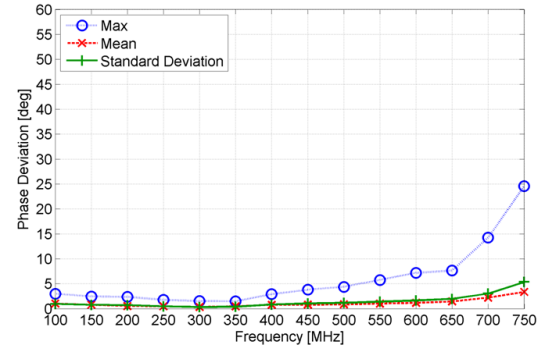
Figure 8. System response to variations of the body diameter.

to the body height are less pronounced than those associated with the body diameter. Still, the largest maximum perturbations occur at 750 MHz: approximately 24.5° for the phase, and 3.9dB for the amplitude. At over 4σ away from the mean, both maximum perturbation values are rare. This is also reflected in the low mean and standard deviation perturbation values for both the phase and amplitude across the frequency band.

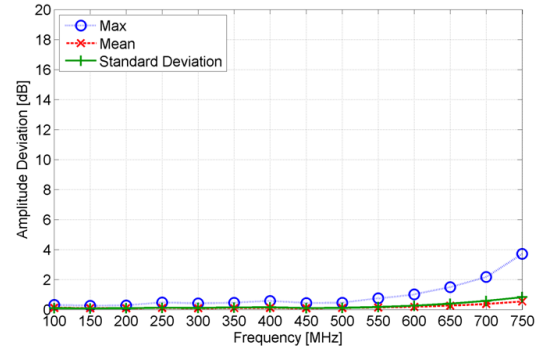
Although the cylindrical human body model provides only a coarse representation of a real user, the height study summarized here and the diameter study summarized above indicate that the nature of the body interaction effects on the phase and amplitude of the system response are impacted more by the diameter of the human body than its height, indicating that real-world implementations of the system may require calibration that considers the stature of the user.

3) *Body Composition*: The nominal body dielectric constant is 60 [11]. To study the effects of this parameter on the amplitude and phase response of the system, dielectric constants of 20, 40, and 80 are compared to the nominal configuration. The frequency-dependent phase and amplitude response perturbations due to the varied body height are provided in Figure 10(a) and Figure 10(b), respectively.

Somewhat surprisingly, these results indicate that



(a) Phase response perturbation.



(b) Amplitude response perturbation.

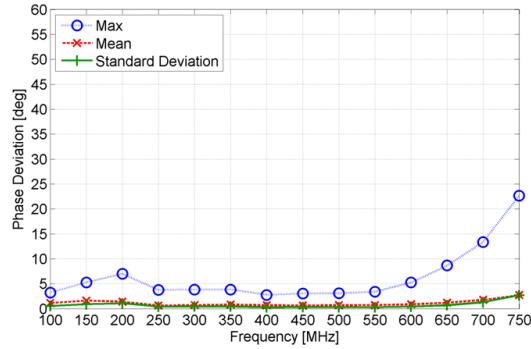
Figure 9. System response to variations of the body height.

the performance of the direction finding system is likely to be relatively insensitive to the composition of the human body, even though the range of constitutive parameters is very large. As previously discussed, the dielectric properties of the human body are dependent on both body composition and frequency. This result is significant, because it indicates that it is the presence of the body that is more important to changing the system dynamics than its specific composition or the signals it is being used to detect.

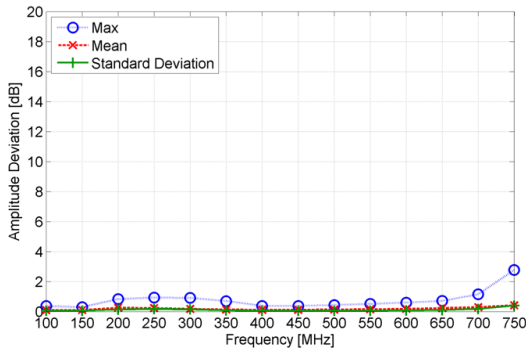
C. System Parameters

1) *Antenna Baseline Separation*: The nominal antenna baseline is 20". To study the effects of this parameter on the amplitude and phase response of the system, antenna baselines of 18" and 22" are compared to the nominal configuration. The frequency-dependent phase and amplitude response perturbations due to the varied antenna baseline separation are provided in Figure 11(a) and Figure 11(b), respectively.

The separation between sensors in a direction finding system has a significant impact on the performance of the system. This phenomenon is confirmed by this study, which indicates that the relative separation of the sensors (not only from one another, but also from the



(a) Phase response perturbation.



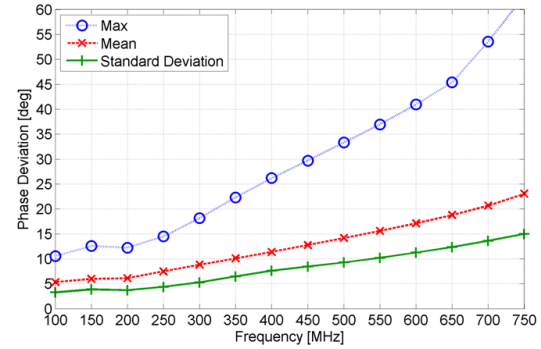
(b) Amplitude response perturbation.

Figure 10. System response to variations of the body composition.

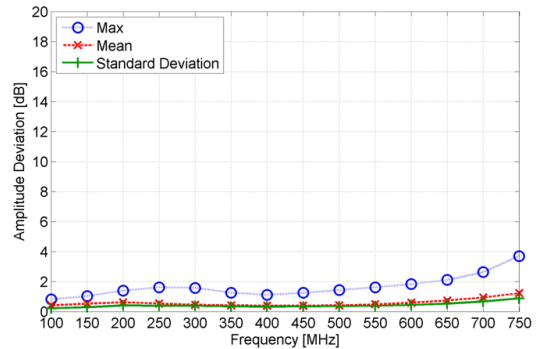
human body) does indeed produce a significant change in the system response. The electrical spacing of the antennas changes the relative time of arrival at signals at the two sensors, accounting for the frequency-dependent effect in the phase response. Somewhat surprisingly, the amplitude response is relatively insensitive to the antenna spacing. In many real-world realizations of this system, this baseline may be mechanically fixed to avoid the perturbations observed here.

2) *Antenna Baseline Rotation*: The nominal antenna baseline oriented parallel to the y-axis. To study the effects of this parameter on the amplitude and phase response of the system, antenna baseline rotations of 5° and 10° are compared to the nominal configuration. The rotational symmetry of the problem precludes the need to study negative rotation values. The frequency-dependent phase and amplitude response perturbations due to the varied antenna baseline rotation are provided in Figure 12(a) and Figure 12(b), respectively.

In the baseline configuration, the antennas are located on the y-axis, perpendicular to the orientation of the user. In real-world applications, it may be possible for the antennas to rotate somewhat with respect to the user. As confirmed by this study, there is a significant perturbation in the system performance if the sensors rotate. The direction finding solution generated by the



(a) Phase response perturbation.



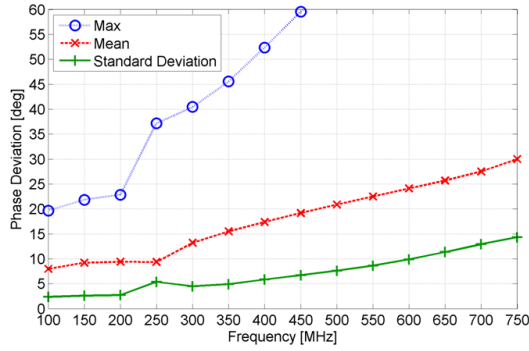
(b) Amplitude response perturbation.

Figure 11. System response to variations of the antenna baseline separation.

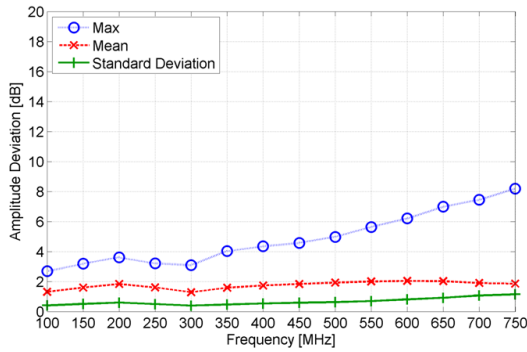
system is referenced to the sensor geometry, so the anticipated result of this rotation is an error in the direction finding solution that is comparable to the rotation of the antennas with respect to the body. However, unlike free space realizations of comparable direction finding systems, this rotation also changes the proximity of the sensors to the body, so additional effects are also expected. The maximum perturbations observed in this study are approximately 121° for the phase and 8.2dB for the amplitude. However, at over 5σ each, these perturbations are relatively uncommon, as reflected in the low mean and standard deviation values.

3) *Antenna Height on Body*: The nominal antenna position is in the middle of the cylindrical body along the z-axis. To study the effects of the positional offset on the amplitude and phase response of the system, antenna baseline heights of 12" and 24" above the nominal plane are computed. The vertical symmetry of the problem precludes the consideration of negative antenna heights. The frequency-dependent phase and amplitude response perturbations due to the varied antenna baseline height are provided in Figure 13(a) and Figure 13(b), respectively.

In the baseline configuration, the sensors are centered at the "equator" of the cylindrical body model.

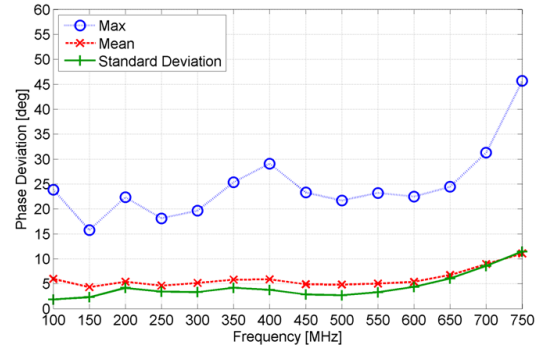


(a) Phase response perturbation.

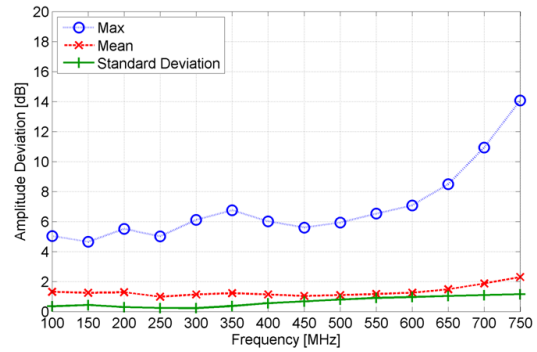


(b) Amplitude response perturbation.

Figure 12. System response to variations of the antenna baseline rotation.



(a) Phase response perturbation.



(b) Amplitude response perturbation.

Figure 13. System response to variations of the antenna baseline height.

Although this configuration may not be realistic for real-world applications, the study summarized here indicates that even large vertical perturbations in the location of the sensors with respect to the body model produce relatively minor perturbations to the phase and amplitude of the system response. In fact, the largest perturbation in phase (approximately 45.5° is over 3σ away from the mean, and the largest perturbation in the amplitude (14dB) is over 10σ above the mean. Much like the results of the body height study, these results indicate that there is relatively little system sensitivity on the relative vertical orientation of the body and the sensors.

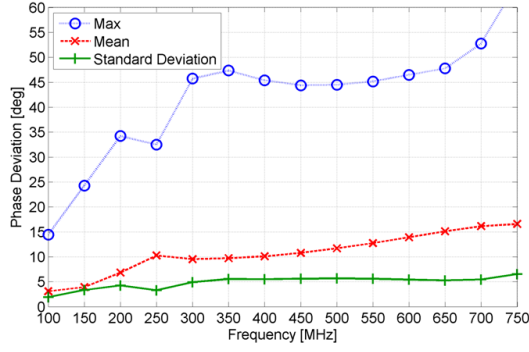
4) *Left/Right Body Centrality*: The nominal body location is centered in the y-axis. To study the effects of this parameter on the amplitude and phase response of the system, left/right (y-axis) body offsets of 1” and 2” are compared to the nominal configuration. The symmetry of the problem makes the use of negative offset values unnecessary. The frequency-dependent phase and amplitude response perturbations due to the varied y-axis body offset are provided in Figure 14(a) and Figure 14(b), respectively.

The performance of the baseline direction finding system is significantly changed in the presence of the body. Given the close electrical proximity of the body

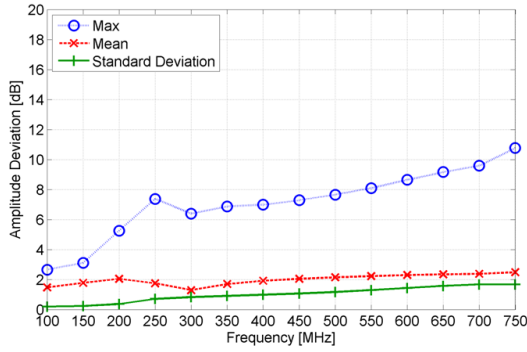
($d \ll \lambda$) to the sensors, the sensitivity of the system response that is associated with changing the location of the body relative to the sensors is important to the stability of the system. The results from this study confirm that slight changes in the relative positions of the sensors and the body may produce significant changes in the nominal system performance.

5) *Forward/Backward Body Centrality*: The nominal body location is offset from the origin by +10” in the x-axis. To study the effects of this parameter on the amplitude and phase response of the system, forward/backward (x-axis) body offsets of 8” and 12” are compared to the nominal configuration. The frequency-dependent phase and amplitude response perturbations due to the varied x-axis body offset are provided in Figure 15(a) and Figure 15(b), respectively.

As with the left/right centrality study, this study confirms that the performance of the baseline direction finding system is significantly influenced by the proximity of the sensors to the body. Between these studies, the most pronounced variation is exhibited by the phase response on the forward/backward sensitivity, where $\sigma_{max} \approx 15^\circ$.

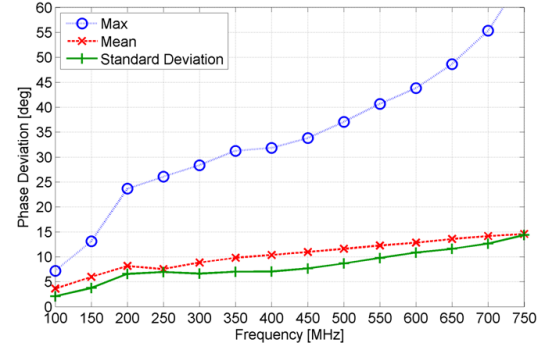


(a) Phase response perturbation.

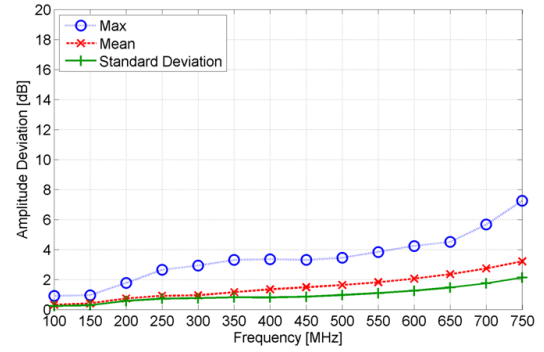


(b) Amplitude response perturbation.

Figure 14. System response to variations of the y-axis body offset.



(a) Phase response perturbation.



(b) Amplitude response perturbation.

Figure 15. System response to variations of the x-axis body offset.

D. Excitation Parameters

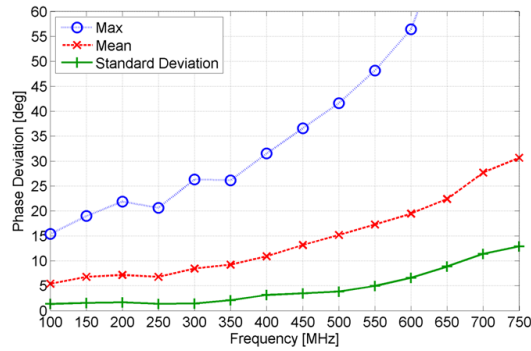
1) *Off-Horizon Signals*: The nominal signals of interest reside in the terrestrial plane ($\theta = 90^\circ$). To study the effects of this parameter on the amplitude and phase response of the system, θ values of 105° and 120° are compared to the nominal configuration. The vertical symmetry of the problem renders above-horizon elevation angle values unimportant to this study. The frequency-dependent phase and amplitude response perturbations due to the varied signal elevation angle are provided in Figure 16(a) and Figure 16(b), respectively.

The phase and amplitude of the currents excited on the sensor depend on the signal's electric field, all scattered modes/fields, and electric field modes supported by the antenna [13]. Accordingly, there is an anticipated change in the system performance when signals arrive from elevation angles away from the azimuthal plane. Although most signals detected by real-world implementations of this system are most likely to arrive from angles within a few degrees of this plane, this study identifies that the system will produce a somewhat different response to signals that are significantly away from the azimuthal plane.

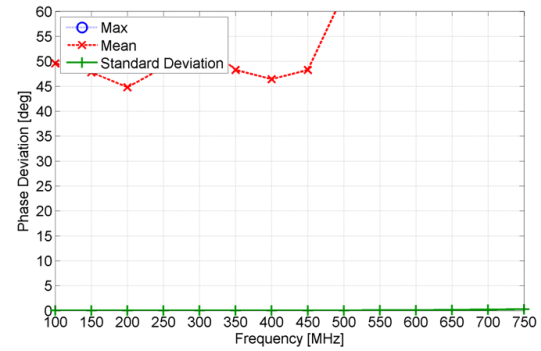
2) *Signal Polarization*: The nominal signals of interest are vertically polarized. To study the effects of this

parameter on the amplitude and phase response of the system, slant- 45° and horizontally polarized signals are compared to the nominal configuration. The frequency-dependent phase and amplitude response perturbations due to the varied signal polarization are provided in Figure 17(a) and Figure 17(b), respectively.

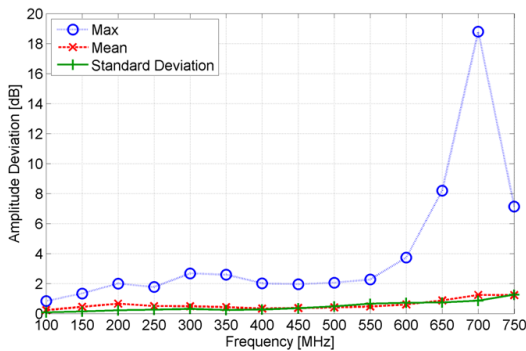
The vertically oriented dipoles used as the system's sensors are vertically polarized. As expected, the perturbation in the system response due to signal polarization is considerable. Specifically, as the signal polarization rotates away from vertical, the system's ability to detect the signal diminishes accordingly. When the signals are slant-polarized, both sensors have an equivalently-diminished ability to detect the signals, and there is little variation in the system, resulting in the very standard deviation values. However, when the signals are horizontally polarized, neither sensor is able to detect the signal well, and there is an unpredictable response, resulting in the large mean and maximum perturbation metrics. Most terrestrial signals are vertically polarized, however, this study identifies the limited nature of the system performance for detecting those signals that are not co-polarized with the sensors.



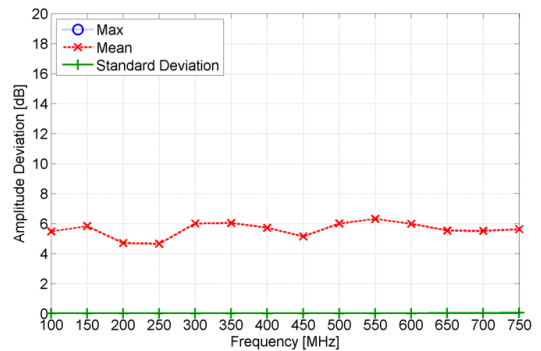
(a) Phase response perturbation.



(a) Phase response perturbation.



(b) Amplitude response perturbation.



(b) Amplitude response perturbation.

Figure 16. System response to variations of the signal elevation angle.

Figure 17. System response to variations of the signal polarization.

E. Detection Thresholds

To combine the results of these studies, frequency-dependent data are collected for the relative phase and amplitude of the response of the direction finding system when seven of the twelve variables are independently perturbed. The seven variables that are selected are body diameter, body height, left/right and forward/backward body centrality, baseline rotation, height on body, and body dielectric constant. These variables represent parameters that are likely to vary among users and with normal user movement. The five variables that are excluded are signal polarization, signal elevation angle, radiator termination impedance, radiator height, and baseline separation. These variables are excluded from this evaluation because they represent fundamental changes to the system that are not likely in the field, or would require a complete recalibration of the system.

As previously discussed, the system response at each frequency is a function of incidence angle. To represent the distribution of the perturbation of the system response across all angles of incidence effectively, these data are consolidated. Specifically, if the angular perturbations are considered to lie in some distribution, it is most convenient to describe the shape of this distribution. Accordingly, the standard deviation of the angular

perturbations is collected as a function of frequency. These data are plotted in Figure 18.

Data from these studies are useful to establish thresholds in phase and amplitude perturbation that will be used to detect incoming signals. Signal perturbations below the levels observed in this study will be ignored by the system, and attributed to slight changes in the system geometry (e.g. due to different users or user movement). Signal perturbations above these levels will be attributed to differences in incoming signals, and will be used to identify these signals and generate direction finding solutions. In these plots, it is clear that there is a frequency dependence in the perturbation of the phase and amplitude of the system response: higher levels of perturbation are seen at higher frequencies. Broken gray lines at approximately 14.5° in Figure 18(a) and just below 2.5dB in Figure 18(b) are used to indicate the maximum signal deviations among each of the selected studies. To simplify the broadband implementation of direction finding techniques, nominal frequency-independent detection thresholds of 10° and 2dB are selected for all frequencies. As highlighted by the “dot-dash” gray lines in Figures 18(a) and 18(b), these threshold levels capture most of the observed deviation values across most of the band of interest. Different techniques for selecting these thresholds are

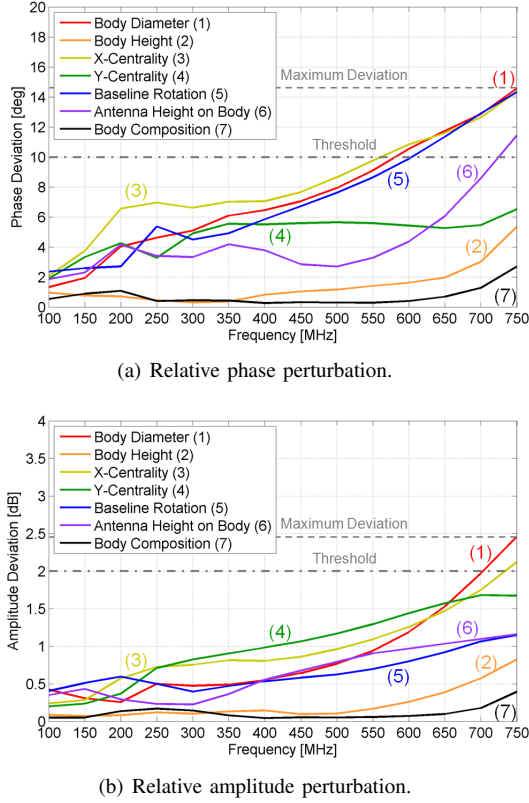


Figure 18. Relative phase and amplitude perturbations from the sensitivity study.

discussed in Section 5.

IV. DIRECTION FINDING CALIBRATION

Having established means of discriminating different signals from one another, it is possible to perform analysis on the performance of the direction finding system. To do so, an auto-correlating direction finding function [7] is used to calibrate the system responses. In this technique, the system response of the direction finding system is auto-correlated using a procedure that produces a correlation error called a direction finding function (DFF). The auto-correlation function uses the spatial signal response, $S(\phi)$, as its input, and identifies parts of the signal that match one another. If the signal is one-to-one, each part of the signal only correlates with itself. If it is not one-to one, multiple portions of the signal will correlate, identifying ambiguities.

For a signal incident from known angle ϕ_0 , the auto-correlation is defined in 1.

$$DFF_{\phi_0}(\phi) \equiv S(\phi_0) - S(\phi) \quad (1)$$

The output of the auto-correlation function is identically equal to 0 when $\phi = \phi_0$, indicating a proper

identification of a signal. However, it is possible that other angles may also minimize the DFF, producing false alarms. The output of this direction finding function at 100 MHz is shown for three different incidence angles in Figure 19(a) and Figure 19(b), using phase and amplitude system responses, respectively, as the input.

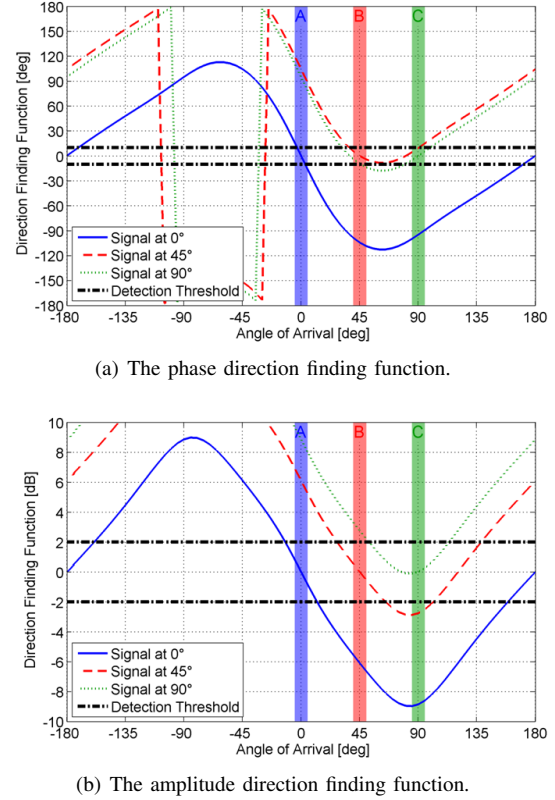


Figure 19. Characterization the phase and amplitude of the system response by the direction finding function.

Note that the three shaded bands on the plots in Figure 19 highlight the areas where the three signals should have zero error (DFF = 0). Indeed, the center of the blue shaded band (labeled “A”) highlights the proper angle for the blue line (0°), the center of the red shaded band (labeled “B”) highlights the zero-crossing of the red line (45°), and the center of the green shaded band (labeled “C”) highlights the zero-crossing of the green line (90°). However, ambiguities are also seen for the incident signals at 0° and 45° . The blue line (0°) has a zero crossing at $\phi_0 = 0^\circ$, but another at $\phi'_0 = \pm 180^\circ$. The red line (45°) has a zero crossing at ($\phi_0 = 45^\circ$, and a false return at $\phi'_0 \approx 120^\circ$ in the phase response, but no false return in the amplitude response.

These data indicate that the phase and amplitude responses can be used to independently generate a direction finding solution. Both approaches are able to identify the proper location of the signal, but may be susceptible to

different ambiguities. An approach to combine these solutions is presented in [14], [15], and is shown to provide better performance than either individual approach.

V. CONCLUSION

In this work, a baseline computational model of a body-borne direction finding system is established. MoM simulations of this system are shown to have excellent agreement with measured data. A parametric system response study is conducted to identify the stability of the system to real-world perturbations. The level of these perturbations is used to establish frequency-independent thresholds that are used by the phase-based and amplitude-based direction finding systems to determine the angle of arrival of incident signals. Based on these data, a calibration technique is used to characterize the performance of the direction finding system, and identify associated ambiguities.

When considered together with the results of the body height and diameter studies, the results of the body composition study indicate that real-world implementations of the system may require specific calibration for different sized users, but will not be susceptible to variations in the user's body composition or the frequency of incoming signals. The raw system response (relative phase and amplitude) is consolidated for signals across all angles of arrival to identify those variables that have the most significant impact on the system. Real-world implementations of the system should be able to control many of these parameters, such as radiator height and separation. However, others may change considerably depending on the user, such as body height and diameter, baseline rotation, and the relative location of the body and the sensors.

A more rigorous theoretical and/or statistical analysis of the perturbation data is recommended for the determination of real-world detection thresholds. Because the focus of this paper is on the computational characterization of the body-borne system, nominal frequency-independent detection thresholds are selected using the data from the parametric system response. These conservative thresholds are useful to highlight their application to a direction finding calibration technique, but do not represent optimized values. Additional work by the authors [14], [15] provides a more thorough description of how the direction finding function can be applied to optimize the performance of a direction finding system. Using the direction finding approach described in the referenced paper, the phase and amplitude detection thresholds can be optimized for various metrics, including accuracy, sensitivity, and false alarm rates.

The results of this study clearly demonstrate the utility of a method of moments in the characterization of direction finding systems. This includes the accurate

replication of body-interaction effects that are observed in measurements. Future examinations based on this work include coupled/multivariable sensitivity studies, improvement of the direction finding calibration, and the extension of the direction finding technique to geolocation applications.

REFERENCES

- [1] S. E. Lipsky, *Microwave Passive Direction Finding*. SciTech, Incorporated, 2003.
- [2] H. de A. Donisthorpe, "The Marconi Marine Radio Direction Finder," *Proceedings of the Institute of Radio Engineers*, vol. 13, no. 1, pp. 29–47, 1925.
- [3] P. Misra and P. Enge, *Global Positioning System - Signals, Measurements, and Performance*. Ganga-Jamuna Press, 2 ed., 2006.
- [4] P. Enge, E. Swanson, R. Mullin, K. Ganther, A. Bommarito, and R. Kelly, "Terrestrial Radio Navigation Technologies," *Navigation*, vol. 42, no. 1, pp. 61–108, 1995.
- [5] H. Jenkins, *Small-Aperture Radio Direction-Finding*. Artech House Publishers, 1991.
- [6] EM Software & Systems, "FEKO." Commercially Licensed Software, 2008.
- [7] A. Bellion, C. L. Meins, A. Julien-Vergonjanne, and T. Monédière, "Generation of Calibration Tables for Direction Finding Antennas Using FEKO," *24th Annual Review of Progress in Applied Computational Electromagnetics (ACES)*, pp. 903–908, 2008.
- [8] N. Uzunoglu, P. Cottis, and P. Papakonstantinou, "Analysis of Thermal Radiation from an Inhomogeneous Cylindrical Human Body Model," *IEEE Trans. Microwave Theory and Techniques*, vol. MTT-35, pp. 761–768, 1987.
- [9] P. Cottis, G. Chatzarakis, and N. Uzunoglu, "Electromagnetic Energy Deposition Inside a Three-Layer Cylindrical Human Body Model Caused by Near-Field Radiators," *IEEE Trans. Microwave Theory and Techniques*, vol. MTT-38, pp. 990–999, 1990.
- [10] K. Gryz, J. Karpowicz, and S. Wincenciak, "Numerical Modeling of Current Flowing in Human Exposed to External Electric Field for Evaluation of Occupational Exposure," *Proceedings of the URSI General Assembly*, 2002.
- [11] Y.-M. Gimm and Y.-J. Ju, "Formulation of the Sugar-Free Human Head Tissue Simulant Liquid for SAR Measurement at 830 MHz," in *Proceedings of the Asia-Pacific Radio Science Conference*, pp. 533–536, 2004.
- [12] J. L. Devore, *Probability and Statistics for Engineering and the Sciences*. Duxbury Press, 6 ed., June 2003.
- [13] W. L. Stutzman and G. A. Thiele, *Antenna Theory and Design*. John Wiley & Sons, second ed., 1998.
- [14] A. Lalezari, F. Lalezari, B. Jeong, and D. Filipović, "Evaluation of Human Body Interaction for the Enhancement of a Broadband Body-Borne Radio Geolocation System," *Proceedings of the Allerton Antenna and Application Symposium*, pp. 436–453, 2008.
- [15] A. C. Lalezari, "Exploitation of Body Interaction Effects for the Enhancement of a Body-Borne Radio Geolocation System," Master's thesis, University of Colorado at Boulder, December 2008.



Arian Lalezari received the B.S. degrees in Electrical Engineering and Applied Mathematics from the University of Colorado in 2005, and the M.S.E.E. degree from the University of Colorado at Boulder in 2008.

Since 2004, he has been working at FIRST RF Corporation in Boulder, CO. At FIRST RF, Mr. Lalezari is currently working on man-portable, low-profile/conformal, satellite communications, and radar antennas.



Farzin Lalezari received the B.S.E.E. and the M.S.E.E degrees from the Polytechnic Institute of Brooklyn in 1976 and 1977, respectively, and completed course work for the PhD degree from the University of Colorado at Boulder from 1977-1978.

Mr. Lalezari is the Principal Engineer for FIRST RF Corporation. He has more than 28 years of experience in antennas and RF systems design. He has a current Top Secret SSBI security clearance. Additionally, Mr.

Lalezari has over 25 patents issued or pending in this field of research. He is responsible for engineering development tasks on government R&D contracts relating to aerospace and defense applications and development of advanced Radio Frequency (RF) technologies including: antennas, antenna systems, electronic warfare (EW) and threat neutralization, algorithms, overall system development for communications, navigation, identification, guidance and control, pointing and control, weapons seekers and fuzing, telemetry, and remote sensing.



Dejan Filipović received the Dipl. Eng. degree in electrical engineering from the University of Nis, Serbia in 1994, and the M.S.E.E. and PhD degrees from the University of Michigan, Ann Arbor in 1999 and 2002 respectively. From 1994 to 1997, he was a Research Assistant at University of Nis. From 1997 to 2002, he was Graduate Student at the University of Michigan. Currently, he is Associate Professor at the University of Colorado, Boulder. His research interests are in

the development of mm-wave components and systems, multi-physics modeling, antenna theory and design, as well as in computational and applied electromagnetics.

Mr. Filipović was the recipient of the prestigious Nikola Tesla Award for his outstanding graduation thesis. He and his students were co-recipients of the Best Paper Award presented at the IEEE Antennas and Propagation Society (AP-S)/URSI and Antenna Application Symposium conferences.

Application of the Normalized Surface Magnetic Source Model to a Blind Unexploded Ordnance Discrimination Test

Fridon Shubitidze¹, Juan Pablo Fernández¹, Irma Shamatava^{1,2},
Leonard R. Pasion², Benjamin E. Barrowes^{1,3}, and Kevin O'Neill^{1,3}

¹ Thayer School of Engineering
Dartmouth College, Hanover, NH 03755-8000, USA
fridon.shubitidze@dartmouth.edu , jpfb@dartmouth.edu

² Sky Research, Inc.
112A-2386 East Mall, Vancouver, BC V6T 1Z3, Canada
irma.shamatava@dartmouth.edu , len.pasion@skyresearch.com

³ USA ERDC Cold Regions Research and Engineering Laboratory
Hanover, NH 03755, USA
benjamin.e.barrowes@usace.army.mil, kevin.o.neill@erdc.usace.army.mil

Abstract—The Normalized Surface Magnetic Source (NSMS) model is applied to unexploded ordnance (UXO) discrimination data collected at Camp Sibert, AL, with the EM63 electromagnetic induction sensor. The NSMS is a fast and accurate numerical forward model that represents an object's response using a set of equivalent magnetic dipoles distributed on a surrounding closed surface. As part of the discrimination process one must also determine the location and orientation of each buried target. This is achieved using a physics-based technique that assumes a target to be a dipole and extracts the location from the measured magnetic field vector and the scalar magnetic potential; the latter is reconstructed from field measurements by means of an auxiliary layer of magnetic charges. Once the object's location is estimated, the measured magnetic field is matched to NSMS predictions to determine the time-dependent amplitudes of the surface magnetic sources, which in turn can be used to generate classifying features. This paper shows the superior discrimination performance of the NSMS model.

Index Terms—UXO, Camp Sibert tests, NSMS model, HAP method, discrimination, inversion.

I. INTRODUCTION

Unexploded ordnance (UXO) is a widespread, long-lasting, and deadly remnant of war and military practice that kills or maims hundreds of people worldwide each year. In the United States alone it is estimated that an area the size of the states of New Hampshire and Vermont put together—as many as 11 million acres of land—may be tainted with UXO, and that the eventual cost of cleaning up the contaminated land will reach the hundreds of billions of dollars [1],[2]. This is not because detecting UXO is difficult: low-frequency electromagnetic induction (EMI) sensors, on which we concentrate here, can easily penetrate the ground and find buried metal, and so can other methods like magnetometry or ground-penetrating radar. What makes the task of decontaminating UXO-polluted land so onerous and expensive is the inability of sensors to single out dangerous ordnance from the morass of innocuous items that usually surrounds them in the field; the latter can comprise smithereens from ordnance that did explode, high-metal-content geology, and anything else from nails to beer cans, all of which, in the absence of further information, must be treated as dangerous. The problem, then, consists of identifying hazardous items and

distinguishing them from clutter as reliably and quickly as possible.

Much research is being presently conducted with the aim of making the UXO remediation process more efficient and economic. To support this effort by providing sound benchmarks, the Strategic Environmental Research and Development Program (SERDP) recently set up UXO discrimination blind tests at sites in Camp Sibert, a former U.S. Army facility near Gadsden, Alabama. Personnel from Sky Research, Inc. under the auspices of SERDP collected data at those test sites using the EM63, a time-domain EMI sensor produced by Geonics Ltd. [3]. The 216 targets buried at the sites include unexploded 4.2" mortars, mortar explosion byproducts like base plates and bent half-shells, smaller shrapnel, and unrelated metallic clutter. In this paper we use those data to demonstrate the discrimination performance of a physically complete, fast, accurate, robust, and clutter-tolerant inverse-scattering approach called the Normalized Surface Magnetic Source (NSMS) model [4], which we present in Section II.

The signal scattered by an object depends both on the intrinsic features of the target (which the NSMS can encapsulate) and on its location and orientation relative to the sensor. Thus an essential step of the discrimination process is determining those extrinsic, observation-dependent factors as accurately as possible for each target. This nonlinear problem is usually attempted simultaneously with the characterization, an approach that often results in ill-posed and computationally expensive optimizations that take time and may yield unreliable answers. Here we bypass that difficulty by employing the physics-based field-potential (HAP) method [5], described in Section III, that pinpoints scatterers quickly and effectively.

The NSMS model and the HAP method ultimately stem from similar considerations. Scattered magnetic fields in the EMI regime are due to eddy currents or magnetic dipoles induced (and in some cases realigned) by the sensor and distributed nonuniformly inside the scatterers. Most of these sources tend to concentrate at some particular points, the so-called "scattered field singularities" (SFS); the study of the mathematical and physical properties of these singularities is part of the discipline known in the literature as

"catastrophe theory" [6]. Recent work shows that under certain conditions the entire scatterer can be replaced with responding elementary sources placed at the SFS [7],[8].

In particular, the NSMS model replaces the scatterer—the UXO or piece of clutter, in this case—with a surrounding spheroid on which a set of radially oriented dipoles is distributed. The strengths of these dipoles are determined as those that best reproduce actual measurements; the composite dipole moment—here referred to as the "total NSMS"—varies significantly for different targets but is remarkably consistent for different specimens of the same object. In turn, the HAP technique assumes that the whole scatterer is a point dipole located at some SFS and finds its location and orientation by means of analytic expressions involving the dipole field and its associated scalar magnetic potential; to construct the latter from the former one distributes elementary sources on an auxiliary layer placed at a location intermediate between the sensor and the object and again finds the dipole moments by fitting measured data.

When combined, the two methods result in a powerful and efficient discrimination method for UXO. The precise location and orientation estimates given by the HAP allow an almost instantaneous determination of the time-dependent total NSMS. This can then be distilled further using an empirical decay law [9] whose fitting parameters can be mixed into discriminating features that tend to group in well-separated tight clusters, resulting in clear-cut classification. In the Camp Sibert blind test only one anomaly out of 216 was not identified correctly. In Section IV we discuss the procedure followed and the results obtained in this study, and in Section V we conclude.

II. THE NORMALIZED SURFACE SOURCE MODEL

The NSMS can be thought of as a generalization of the infinitesimal dipole model [9],[10],[11], with which it coincides in the limit. The dipole model postulates that for any given object it is possible to find a set of three orthonormal "body" axes such that a uniform primary field impinging along any of those directions induces a magnetization—and hence a dipole moment—parallel and linearly proportional

to it. A primary field \mathbf{H}^{pr} pointing along an arbitrary direction thus creates a dipole moment $\mathbf{m} = \bar{\bar{\mathbf{M}}} \cdot \mathbf{H}^{\text{pr}}$, where the polarizability tensor $\bar{\bar{\mathbf{M}}}$ projects \mathbf{H}^{pr} onto the body system, finds the magnetization components there—this being the only step that depends on the object and not on the geometry—and synthesizes the dipole moment back in the global frame. The point dipole model is conceptually simple, fast, and reasonably powerful, and for that reason has been frequently used in discrimination studies [9],[12],[13]. However, its limitations become apparent when the target to be identified is heterogeneous, and thus composed of two or more mutually interacting sections, or when, as is usually the case in EMI measurements, the primary field established by the sensor varies appreciably over the dimensions of the target and strikes each region with a different intensity and direction. These problems can be addressed by substituting the single point dipole with an assembly of responding sources.

In the particular version of the NSMS used for the Camp Sibert test we distribute dipoles on a prolate spheroidal surface that surrounds the object of interest. By choosing a spheroid we simultaneously exploit the realism granted by its orientable elongated shape and the simplicity afforded by its azimuthal symmetry—a quality spheroids share with most UXO. We divide the spheroid S into subsurfaces (either patches or belts) and assign

$$\mathbf{H}^{\text{sc}}(\mathbf{r}) = \oint_S \frac{M(s')}{4\pi R_{s'}^3} \left[\frac{3(\xi_{s'} \cdot \mathbf{R}_{s'})\mathbf{R}_{s'}}{R_{s'}^2} - \xi_{s'} \right] ds', \quad (1)$$

where $\mathbf{R}_{s'} = \mathbf{r} - \mathbf{r}_{s'}$ is a vector that points from the location $\mathbf{r}_{s'}$ of the s' -th infinitesimal patch on the spheroid to the observation point \mathbf{r} and $\xi_{s'}$ is the unit vector normal to the patch, which is most easily found in prolate spheroidal coordinates. All of these quantities clearly depend on the location and orientation of the spheroid relative to the sensor. The dipole directions are fixed by their locations on the spheroid, so to factor out the geometric particulars we set

$$M(s') = \Omega(s') [\xi(s') \cdot \mathbf{H}^{\text{pr}}(s')], \quad (2)$$

which defines a new normalized surface polarization distribution $\Omega(s')$. Such a distribution can be generated by spreading virtual positive magnetic charge over the exterior of an infinitesimally thin spheroidal shell and negative charge on its inner surface, resulting in a double layer. This configuration introduces the proper discontinuities in the tangential components of the magnetic flux density vector \mathbf{B} at the boundary between two media but does not affect its normal component, keeping \mathbf{B} divergence-free and the model consistent with the absence of free magnetic monopoles in nature.

By choosing a suitable quadrature scheme it is possible to transform Eq. (1) into the matrix-vector product $\mathbf{H}^{\text{sc}} = \bar{\bar{\mathbf{Z}}} \cdot \Omega$. Each column of the scattering matrix $\bar{\bar{\mathbf{Z}}}$ corresponds to a different subsurface, and each row to a measurement point at which data are collected. The amplitude vector Ω can be determined directly, and with great speed and accuracy, by minimizing in a least-squares sense the difference between measured data and the predictions of Eq. (1) at a sufficient set of points for a known object-sensor configuration:

$$\min_{\Omega} \frac{1}{2} (\bar{\bar{\mathbf{Z}}} \cdot \frac{1}{2} - \mathbf{H}^{\text{meas}})^2, \quad (3)$$

whose solution is the normal equation

$$\frac{1}{2} = [\bar{\bar{\mathbf{Z}}}^T \cdot \bar{\bar{\mathbf{Z}}}]^{-1} [\bar{\bar{\mathbf{Z}}}^T \cdot \mathbf{H}^{\text{meas}}]. \quad (4)$$

Once Ω is found one can define a “total” or “average” polarizability by integrating over the whole spheroid. The resulting quantity

$$Q = \oint_S \Omega(s') ds' \quad (5)$$

is a global magnetic capacitance of sorts. Different studies [4] have shown that, within reasonable limits, Q for a given object is invariant with respect to the constructs used for its determination: spheroid size and aspect ratio, measurement grid, object location or orientation, primary field, etc. It is thus intrinsic to the object and can be used, on its own or combined with other quantities, in discrimination processing, either within a “genuine” inversion procedure that uses Q itself as a discriminant or through a “pattern matching” method that compares measured fields to those stored in a library of known objects and

determines which known UXO has the catalogued source distribution that best reproduces the signal received by the survey sensor. Used in this way, the NSMS system is a faster forward model than other physically motivated models such as the standardized excitation approach (SEA) [14],[15] or the generalized SEA described in [16],[17].

The actual signal picked up by the sensor is more complicated than Eq. (1), since, in observance of Faraday's Law, it is the negative of the time derivative of the magnetic flux through the receiver coil. Thus it is necessary to perform an additional quadrature to incorporate the surface integral over the coil (and have Q absorb a minus sign). A deeper issue has to do with the time dependence of Q . Equations (1)–(4) are evaluated separately at each time gate and formally yield a “time-dependent” distribution $Q(t)$, even though in rigor the transient response must take into account the complete history of excitation and involve both the impulse response of the target and the waveform of the sensor. Still, it is reasonable to determine and use the amplitude $Q(t)$, even though it has no actual physical reality, because its manifestation is unique. Moreover, we are interested only in the field *outside* the targets, where it can be assumed that electromagnetic phenomena occur instantaneously. A thorough study of this problem, including detailed calculations of full time responses, can be found in Ref. [18].

III. A METHOD TO ESTIMATE THE LOCATION OF A BURIED OBJECT

Consider a point dipole located at \mathbf{r}_d with a moment \mathbf{m} that in general may be dependent on frequency or time. In the magnetoquasistatic regime that concerns us the dipole generates at the observation point \mathbf{r} a field

$$\mathbf{H}(\mathbf{r}) = \frac{1}{4\pi R^3} \left[\frac{3(\mathbf{m} \cdot \mathbf{R})\mathbf{R}}{R^2} - \mathbf{m} \right], \quad (6)$$

where $\mathbf{R} = \mathbf{r} - \mathbf{r}_d$, which in turn can be derived from the scalar potential

$$\psi(\mathbf{r}) = \frac{\mathbf{m} \cdot \mathbf{R}}{4\pi R^3}. \quad (7)$$

A simple algebraic manipulation lets us find \mathbf{r}_d in terms of \mathbf{H} and ψ : take the dot product of \mathbf{H} and \mathbf{R} and use ψ to show that

$$\mathbf{H} \cdot \mathbf{R} = 2 \frac{\mathbf{m} \cdot \mathbf{R}}{4\pi R^3} = 2\psi, \quad (8)$$

which can be cast as

$$\mathbf{H} \cdot \mathbf{r}_d = -2\psi + \mathbf{H} \cdot \mathbf{r}. \quad (9)$$

Given N observation points it is possible to find a least-squares estimate of the dipole location using

$$\begin{bmatrix} H_{x,1} & H_{y,1} & H_{z,1} \\ H_{x,2} & H_{y,2} & H_{z,2} \\ \vdots & \vdots & \vdots \\ H_{x,N} & H_{y,N} & H_{z,N} \end{bmatrix} \begin{bmatrix} x_d \\ y_d \\ z_d \end{bmatrix} = \begin{bmatrix} -2\psi_1 + \mathbf{H}_1 \cdot \mathbf{r}_1 \\ -2\psi_2 + \mathbf{H}_2 \cdot \mathbf{r}_2 \\ \vdots \\ -2\psi_N + \mathbf{H}_N \cdot \mathbf{r}_N \end{bmatrix} \quad (10)$$

since at every point i we know the location \mathbf{r}_i of the sensor and the value \mathbf{H}_i of the vector magnetic field. The only quantity not readily available is the scalar potential, but that can be reconstructed using a method similar to that from the preceding section. We assume that the scattered magnetic field is produced by a set of magnetic sources—charges, in this case—placed on a fictitious surface located just below the measurement points. The field is then

$$\mathbf{H}(\mathbf{r}_i) = \int \frac{q(s')}{4\pi} \frac{\mathbf{r}_i - \mathbf{r}_{s'}}{|\mathbf{r}_i - \mathbf{r}_{s'}|^3} ds', \quad (11)$$

to which corresponds a scalar potential

$$\psi(\mathbf{r}_i) = \int \frac{q(s')}{4\pi |\mathbf{r}_i - \mathbf{r}_{s'}|} ds'. \quad (12)$$

The positions $\mathbf{r}_{s'}$ of the sources are fixed and known by construction, so it remains to determine the charges $q(s')$. This is again achieved by minimizing the difference between model predictions and collected data \mathbf{H}^{meas} at a set of known points. We use a quadrature scheme to turn Eq. (11) into a matrix-vector product and then determine

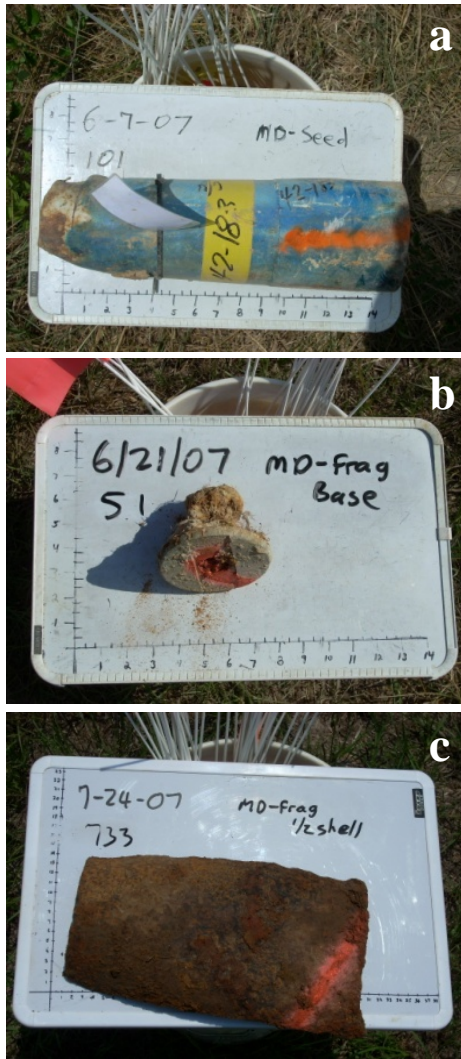


Fig. 1. Example items buried in the ground at the Camp Sibert plots: a) 4.2-inch mortar, b) base plate, c) partial mortar.

$$\min_{\mathbf{q}} \frac{1}{2} \left\| \begin{bmatrix} \mathbf{Z}_x \\ \mathbf{Z}_y \\ \mathbf{Z}_z \end{bmatrix} \cdot \mathbf{q} - \begin{bmatrix} \mathbf{H}_x^{\text{meas}} \\ \mathbf{H}_y^{\text{meas}} \\ \mathbf{H}_z^{\text{meas}} \end{bmatrix} \right\|^2, \quad (13)$$

where each matrix row corresponds to a different measurement point and each column to a subsurface of the underground virtual source layer. This method and its adaptation to monostatic sensors (like that used for the Camp Sibert test) are discussed in detail in Ref. [5].

IV. NUMERICAL RESULTS

The Camp Sibert blind-test data was collected over 216 cells, each of which was a square of side 5 m and contained one anomaly. There were three main kinds of targets: 4.2" UXO, base plates, and partial mortars (Fig. 1), to which were added smaller shrapnel and non-UXO related scrap. We were given a set of calibration data for each type of object, which we used to build a catalog of expected total NSMS values.

The Geonics EM63 collects data over 26 time channels, with the first gate centered at 180 μs and the last at 25 ms. Approximately 700 data points were taken per time channel at each cell; the measurement locations for a typical cell (which in this particular case contained a mortar target) are shown as points in Fig. 2. The figure shows the scattered field values measured by the sensor (left column) and reconstructed by the combined procedure from the previous sections (right column), along with the absolute value of the difference between the two. The top row corresponds to the very first time gate and the bottom row depicts the 20th, centered at 7.65 ms. We see that the predictions agree well with the actual values. Our next task is to see whether these reasonable predictions are realizations of a sound model.

Initially we solved simultaneously for the total NSMS and the location and orientation of each anomaly using a Levenberg-Marquardt nonlinear least-squares optimization [19]. The results of that procedure are presented elsewhere [20]. As seen in that reference, it was difficult to categorize each target reliably because there tended to be a large uncertainty in the location. (To save time we performed the Levenberg-Marquardt search only once per target, so many of those optimizations may have reported finding a local minimum.) We obtained much better results by finding the locations and orientations of the targets using the HAP method and then characterizing the located objects using a 3D NSMS code. The inverted total NSMS strengths for all anomalies appear on Fig. 3. The figure also separates the curves corresponding to each of the major kinds of targets sought.

The total NSMS depends on the size, the geometry, and the material composition of the object it represents. Early time gates bring out the high-frequency response to the shutdown of the

exciting field; since the skin depth $\delta \propto f^{-1/2}$, the eddy currents in this range are superficial, and a large NSMS amplitude at early times correlates with large objects whose surface stretches wide. At late times, where the eddy currents have diffused completely into the object and low-frequency harmonics dominate, the EMI response relates to the metal content (volume) of the target. Thus a smaller but compact object like the base plate of Fig. 1(c) has a relatively weak early response that dies down slowly, while a large but thin, essentially hollow object like the partial mortar (bent half-shell) of Fig. 1(d) has an initially strong response that decays quickly. The unexploded 4.2" mortar, being large and tightly packed, has a substantial early response that persists for a long time.

The previous considerations may be put on a more quantitative footing through discrimination features that summarize these characteristics

(initial amplitude, time constant, etc.) for the different NSMS curves. To that end we employ an empirical power-law/exponential decay expression first proposed by Pasion and Oldenburg [9],

$$Q(t) = kt^{-\beta}e^{-\gamma t}, \quad (14)$$

where t is the time, k , β , and γ are fitting parameters, and $Q(t)$ is the total NSMS from Fig. 3. After investigating different combinations of k , β , and γ we found that the ratio of Q at the 15th time channel to Q at the first time channel, which involves a fixed combination of β and γ , showed good classification ability when plotted against k . Figure 4 depicts $Q(t_{15})/Q(t_1)$ versus k for all items. The results show a clear and robust clustering in this feature space that can result in dependable classification. In particular, we see that the values for the 4.2" mortars are

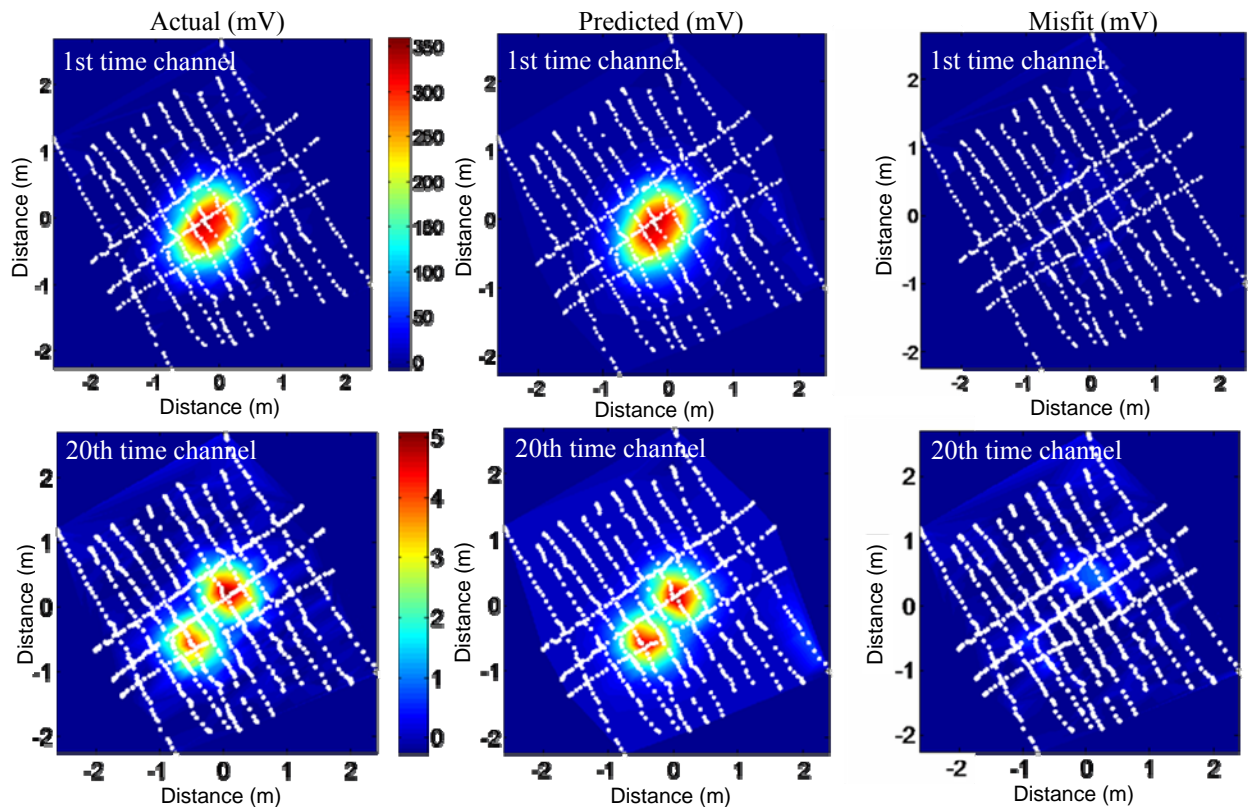


Fig. 2. EM63 data sets: near field distributions for a typical case, measured (left column), predicted (middle), and misfit (right). The white dots show the measurement points on the 5 m-by-5 m square plot. The first time channel (top row) is taken 80 μ s after shutdown; the 20th (bottom) corresponds to 7.65 ms.

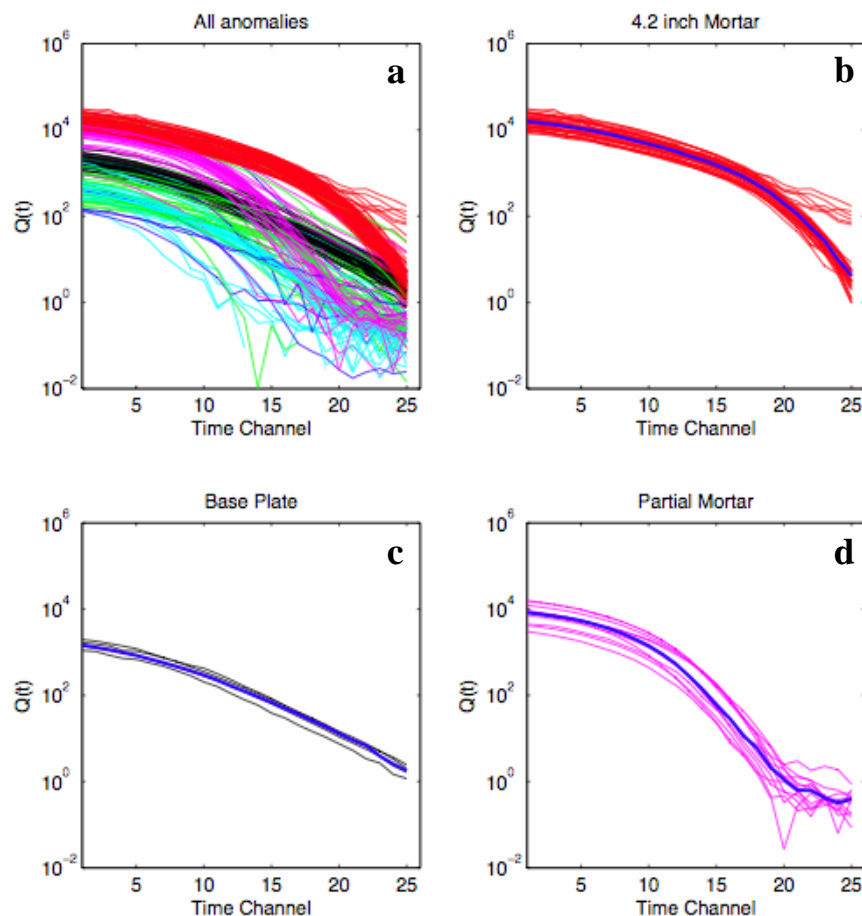


Fig. 3. Inverted total NSMS amplitudes for all anomalies (a) and classification results. The UXO (red, b) have a large spatial extent and thus a large initial amplitude, as do the partial mortars (bent hollow shells) (magenta, d). They are also packed tight and hence have a high metal concentration, just like the base plates (gray, c), resulting in a relatively slow time decay. The other objects are much smaller.

very well grouped and noticeably distinct from those of the base plates and the partial mortars. We knew the ground truth for 66 of the anomalies and used that information to make predictions for the other 150. Our combined NSMS/HAP method correctly identified all UXO and had only one false alarm. The resulting Receiver Operating Characteristic (ROC) curve, omitted here, is an almost perfect square.

The combination of $Q(t_{15})/Q(t_1)$ and k is a solid discriminator but not the only one available. It is possible to study directly the clustering of k , β , and γ in a 3D feature space or perform a similar analysis for the full $Q(t)$. We are in the process of implementing classification algorithms

that do just that and will present the results in forthcoming reports.

V. CONCLUSION

In this paper we applied the NSMS model to the EM-63 Camp Sibert discrimination data sets. First the locations of the objects were inverted for by means of a very efficient and accurate dipole-inspired method; subsequently each anomaly was characterized at each time channel through its total NSMS strength. Classification features were selected and extracted for each object using the Pasion-Oldenburg decay law. Our study reveals that the ratio of an object's late response to its early response provides a good discrimination parameter when plotted against the Pasion-

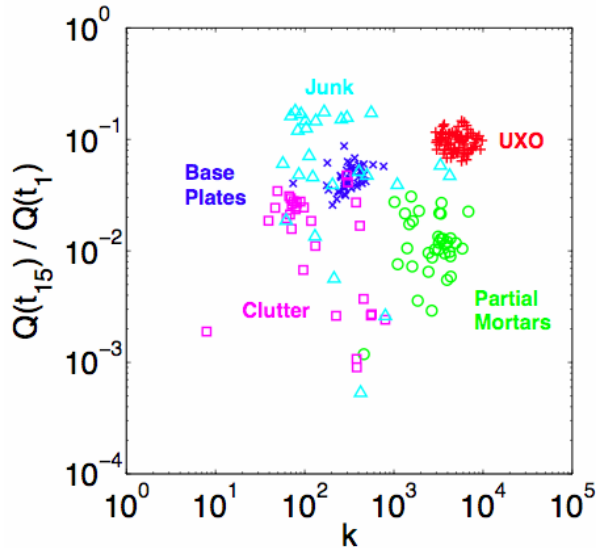


Fig. 4. The total NSMS ratio $Q(t_{15})/Q(t_1)$ becomes a robust classifier when plotted against the feature-space parameter k . The (red) crosses that correspond to the mortars are particularly well clustered and distinctly separate from the markers belonging to the other target types.

Oldenburg amplitude. These results, and those of other tests [21],[22], show that the NSMS/HAP combined procedure is capable of correctly singling out UXO from among munitions-related debris and other clutter, both natural and artificial, that always plagues former battlefields and proving grounds. It is thus a strong candidate to help solve the serious international problem of UXO proliferation.

ACKNOWLEDGEMENT

This work was supported by the Strategic Environmental Research and Development Program through grant # MM-1572.

REFERENCES

- [1] B. Johnson *et al.*, "A research and development strategy for unexploded ordnance sensing," tech. rep. EMP-1, MIT Lincoln Lab, Lexington, MA, 1996.
- [2] Federal Advisory Committee for the Development of Innovative Technologies, "Unexploded ordnance (UXO): An overview," <https://www.denix.osd.mil>, 1996.
- [3] J. D. McNeill and M. Bosnar, "Application of TDEM techniques to metal detection and discrimination: a case history with the new Geonics EM-63 fully time-domain metal detector," tech. note TN-32, Geonics LTD, Mississauga, ON, 2000.
- [4] F. Shubitidze, K. O'Neill, B. Barrowes, I. Shamatava, K. Sun, J. P. Fernández, and K. D. Paulsen, "Application of the normalized surface magnetic charge model to UXO discrimination in cases with overlapping signals," *J. Appl. Geophys.*, vol. 61, pp. 292–303, 2007.
- [5] F. Shubitidze, D. Karkashadze, B. Barrowes, I. Shamatava, and K. O'Neill, "A new physics based approach for estimating a buried object's location, orientation and magnetic polarization for EMI data," *J. Environ. Eng. Geophys.*, vol. 13, pp. 115–130, 2008.
- [6] V. I. Arnold, *Catastrophe Theory*, second edition, Springer, Berlin, 1986.
- [7] A. G. Kyurkchan, B. Yu. Sternin, and V. E. Shatalov, "Singularities of continuation of wave fields," *Phys. Usp.*, vol. 31, pp. 1221–1242, 1996.
- [8] R. Zaridze, G. Bit-Babik, K. Tavzarashvili, D. P. Economou, and N. K. Uzunoglu, "Wave field singularity aspects in large-size scatterers and inverse problems," *IEEE Trans. Antennas Propag.*, vol. 50, pp. 50–58, 2002.
- [9] L. R. Pasion and D. W. Oldenburg, "A discrimination algorithm for UXO using time domain electromagnetics," *J. Environ. Eng. Geophys.*, vol. 6, pp. 91–102, 2001.
- [10] J. Van Bladel, *Electromagnetic Fields*, first edition, McGraw-Hill, New York, 1964.
- [11] F. S. Grant and G. F. West, *Interpretation Theory in Applied Geophysics*, McGraw-Hill, New York, 1965.
- [12] T. H. Bell, B. J. Barrow, and J. T. Miller, "Subsurface discrimination using electromagnetic induction sensors," *IEEE Trans. Geosci. Remote Sens.*, vol. 39, pp. 1286–1293, 2001.
- [13] Y. Zhang, L. Collins, H. Yu, C. E. Baum, and L. Carin, "Sensing of unexploded ordnance with magnetometer and induction data: Theory and signal processing," *IEEE Trans. Geosci. Remote Sens.*, vol. 41, pp. 1005–1015, 2003.
- [14] K. Sun, K. O'Neill, F. Shubitidze, I. Shamatava, and K. D. Paulsen, "Fast data-

derived fundamental spheroidal excitation models with application to UXO discrimination,” *IEEE Trans. Geosci. Remote Sens.*, vol. 43, pp. 2573–2583, 2005.

- [15] J. P. Fernández, B. Barrowes, K. O’Neill, I. Shamatava, F. Shubitidze, and K. Sun, “A data-derived time-domain SEA for UXO identification using the MPV sensor,” *Proc. SPIE*, vol. 6953, no. 6953-1H, 2008.
- [16] F. Shubitidze, B. Barrowes, I. Shamatava, J. P. Fernández, and K. O’Neill, “Data-derived generalized SEA applied to MPV TD data,” Applied Computational Electromagnetics Symposium, Niagara Falls, Mar.–Apr. 2008.
- [17] I. Shamatava, F. Shubitidze, B. Barrowes, E. Demidenko, J. P. Fernández, and K. O’Neill, “The generalized SEA and a statistical signal processing approach applied to UXO discrimination,” *Proc. SPIE*, vol. 6953, no. 6953-53, 2008.
- [18] L.-P. Song, F. Shubitidze, L. R. Pasion, D. W. Oldenburg, and S. D. Billings, “Computing transient electromagnetic responses of a metallic object using a spheroidal excitation approach,” *IEEE Geosci. Remote Sens. Lett.*, vol. 5, pp. 359–363, 2008.
- [19] D. Marquardt, “An algorithm for least-squares estimation of non-linear parameters,” *SIAM J. Appl. Math.*, vol. 11, pp. 431–441, 1963.
- [20] I. Shamatava, F. Shubitidze, B. Barrowes, J. P. Fernández, L. R. Pasion, and K. O’Neill, “Applying the physically complete EMI models to the ESTCP Camp Sibert Pilot Study EM-63 data,” *Proc. SPIE*, vol. 7303, no. 7303-23, 2009.
- [21] F. Shubitidze, B. Barrowes, J. P. Fernández, I. Shamatava, and K. O’Neill, “APG UXO discrimination studies using advanced EMI models and TEMTADS data,” *Proc. SPIE*, vol. 7303, no. 7303-21, 2009.
- [22] I. Shamatava, F. Shubitidze, B. Barrowes, J. P. Fernández, and K. O’Neill, “Physically complete models applied to BUD time-domain EMI data,” *Proc. SPIE*, vol. 7303, no. 7303-22, 2009.



Fridon Shubitidze received the degree of Diploma radio physicist (M.S.) from the Sukhumi branch of Tbilisi State University (TSU), Republic of Georgia, and the Cand.Sci. (Ph.D.) degree in radio physics (applied electromagnetics) from

TSU. He has been a Member of the Laboratory of Applied Electrodynamics at TSU, a Postdoctoral Fellow with the National Technical University of Athens in Greece, and a Visiting Scientist at the University of British Columbia. He is currently a Research Professor with the Thayer School of Engineering, Dartmouth College, Hanover, NH. His current work focuses on numerical modeling of forward and inverse electromagnetic scattering by subsurface and underwater metallic objects and the electrodynamic aspects of DNA sequencing.



Juan Pablo Fernández received the degree of Físico from the Universidad de los Andes in Bogotá, Colombia, the Ph.D. degree in theoretical low-temperature physics from the University of Massachusetts Amherst, and the M.S. degree

in engineering sciences from the Thayer School of Engineering, Dartmouth College, Hanover, NH, where he has also been a Research Associate. He has taught physics, mathematics, astronomy, Spanish, and scientific writing at universities in Colombia and the United States and has worked as a writer, editor, translator, and grant proposal review manager. His current research centers on the discrimination of unexploded ordnance using electromagnetic induction methods and machine learning.



Irma Shamatava received the degree of Diploma radio physicist (M.S.) from the Sukhumi branch of Tbilisi State University, Tbilisi, Georgia, where she was also part of the Computer Center staff and an Assistant Teacher of physics

and mathematics. She is currently a Researcher with the Thayer School of Engineering, Dartmouth College, and with Sky Research, Inc., both in Hanover, NH. Her research interests focus on analytical and numerical modeling of electromagnetic scattering by subsurface metallic objects, especially unexploded ordnance.



Leonard R. Pasion studied mathematical physics at Simon Fraser University in British Columbia and received the M.Sc. and the Ph.D. degrees, both in geophysics, from the University of British Columbia in Vancouver,

where he also was a Post Doctoral Fellow. At present he is Senior Scientist at Sky Research, Inc., in Vancouver, where he manages research programs focused on the detection and discrimination of UXO and landmines using geophysical data and conducts research on data processing techniques for UXO discrimination. He has been principal investigator in various projects funded by the Strategic Environmental Research and Development Program.



Benjamin E. Barrowes received both his B.S. and M.S. degrees in Electrical Engineering from Brigham Young University and the Ph.D. degree from the Massachusetts Institute of Technology. He was a Director's funded Postdoc at

the Physics Division of the Los Alamos National Laboratory in New Mexico. Currently, he is a physicist with the ERDC Cold Regions Research and Engineering Laboratory in Hanover, NH. His research interests center on electromagnetic wave theory and modeling with applications including wind-wave interaction, electromagnetic scattering from the sea surface and from random media, nanoscale energy generation techniques, and electromagnetic induction models for nonspherical geometries. Other interests include automatic code conversion and translation and arbitrary precision computing.



Kevin O'Neill received the B.A. degree from Cornell University, Ithaca, NY, and the M.A., M.S.E., and Ph.D. degrees from Princeton University, Princeton, NJ. After a National Science Foundation Postdoctoral Fellowship at the

Thayer School of Engineering at Dartmouth College and the U.S. Army Corps of Engineers Cold Regions Research and Engineering Laboratory (CRREL), both in Hanover, NH, he joined CRREL as a Research Civil Engineer and the Thayer School as an adjunct professor. He has been a Visiting Fellow in the Department of Agronomy, Cornell University, and a Visiting Scientist with the Center for Electromagnetic Theory and Applications at MIT. His current research centers on electromagnetic remote sensing of surfaces, layers, and especially buried objects such as unexploded ordnance.

ACES COPYRIGHT FORM

This form is intended for original, previously unpublished manuscripts submitted to ACES periodicals and conference publications. The signed form, appropriately completed, MUST ACCOMPANY any paper in order to be published by ACES. PLEASE READ REVERSE SIDE OF THIS FORM FOR FURTHER DETAILS.

TITLE OF PAPER:

RETURN FORM TO:

Dr. Atef Z. Elsherbeni
University of Mississippi
Dept. of Electrical Engineering
Anderson Hall Box 13
University, MS 38677 USA

AUTHORS(S)

PUBLICATION TITLE/DATE:

PART A - COPYRIGHT TRANSFER FORM

(NOTE: Company or other forms may not be substituted for this form. U.S. Government employees whose work is not subject to copyright may so certify by signing Part B below. Authors whose work is subject to Crown Copyright may sign Part C overleaf).

The undersigned, desiring to publish the above paper in a publication of ACES, hereby transfer their copyrights in the above paper to The Applied Computational Electromagnetics Society (ACES). The undersigned hereby represents and warrants that the paper is original and that he/she is the author of the paper or otherwise has the power and authority to make and execute this assignment.

Returned Rights: In return for these rights, ACES hereby grants to the above authors, and the employers for whom the work was performed, royalty-free permission to:

1. Retain all proprietary rights other than copyright, such as patent rights.
2. Reuse all or portions of the above paper in other works.

3. Reproduce, or have reproduced, the above paper for the author's personal use or for internal company use provided that (a) the source and ACES copyright are indicated, (b) the copies are not used in a way that implies ACES endorsement of a product or service of an employer, and (c) the copies per se are not offered for sale.

4. Make limited distribution of all or portions of the above paper prior to publication.

5. In the case of work performed under U.S. Government contract, ACES grants the U.S. Government royalty-free permission to reproduce all or portions of the above paper, and to authorize others to do so, for U.S. Government purposes only.

ACES Obligations: In exercising its rights under copyright, ACES will make all reasonable efforts to act in the interests of the authors and employers as well as in its own interest. In particular, ACES REQUIRES that:

1. The consent of the first-named author be sought as a condition in granting re-publication permission to others.
2. The consent of the undersigned employer be obtained as a condition in granting permission to others to reuse all or portions of the paper for promotion or marketing purposes.

In the event the above paper is not accepted and published by ACES or is withdrawn by the author(s) before acceptance by ACES, this agreement becomes null and void.

AUTHORIZED SIGNATURE

TITLE (IF NOT AUTHOR)

EMPLOYER FOR WHOM WORK WAS PERFORMED

DATE FORM SIGNED

Part B - U.S. GOVERNMENT EMPLOYEE CERTIFICATION

(NOTE: if your work was performed under Government contract but you are not a Government employee, sign transfer form above and see item 5 under Returned Rights).

This certifies that all authors of the above paper are employees of the U.S. Government and performed this work as part of their employment and that the paper is therefor not subject to U.S. copyright protection.

AUTHORIZED SIGNATURE

TITLE (IF NOT AUTHOR)

NAME OF GOVERNMENT ORGANIZATION

DATE FORM SIGNED

PART C - CROWN COPYRIGHT

(NOTE: ACES recognizes and will honor Crown Copyright as it does U.S. Copyright. It is understood that, in asserting Crown Copyright, ACES in no way diminishes its rights as publisher. Sign only if *ALL* authors are subject to Crown Copyright).

This certifies that all authors of the above Paper are subject to Crown Copyright. (Appropriate documentation and instructions regarding form of Crown Copyright notice may be attached).

AUTHORIZED SIGNATURE

TITLE OF SIGNEE

NAME OF GOVERNMENT BRANCH

DATE FORM SIGNED

Information to Authors

ACES POLICY

ACES distributes its technical publications throughout the world, and it may be necessary to translate and abstract its publications, and articles contained therein, for inclusion in various compendiums and similar publications, etc. When an article is submitted for publication by ACES, acceptance of the article implies that ACES has the rights to do all of the things it normally does with such an article.

In connection with its publishing activities, it is the policy of ACES to own the copyrights in its technical publications, and to the contributions contained therein, in order to protect the interests of ACES, its authors and their employers, and at the same time to facilitate the appropriate re-use of this material by others.

The new United States copyright law requires that the transfer of copyrights in each contribution from the author to ACES be confirmed in writing. It is therefore necessary that you execute either Part A-Copyright Transfer Form or Part B-U.S. Government Employee Certification or Part C-Crown Copyright on this sheet and return it to the Managing Editor (or person who supplied this sheet) as promptly as possible.

CLEARANCE OF PAPERS

ACES must of necessity assume that materials presented at its meetings or submitted to its publications is properly available for general dissemination to the audiences these activities are organized to serve. It is the responsibility of the authors, not ACES, to determine whether disclosure of their material requires the prior consent of other parties and if so, to obtain it. Furthermore, ACES must assume that, if an author uses within his/her article previously published and/or copyrighted material that permission has been obtained for such use and that any required credit lines, copyright notices, etc. are duly noted.

AUTHOR/COMPANY RIGHTS

If you are employed and you prepared your paper as a part of your job, the rights to your paper initially rest with your employer. In that case, when you sign the copyright form, we assume you are authorized to do so by your employer and that your employer has consented to all of the terms and conditions of this form. If not, it should be signed by someone so authorized.

NOTE RE RETURNED RIGHTS: Just as ACES now requires a signed copyright transfer form in order to do "business as usual", it is the intent of this form to return rights to the author and employer so that they too may do "business as usual". If further clarification is required, please contact: The Managing Editor, R. W. Adler, Naval Postgraduate School, Code EC/AB, Monterey, CA, 93943, USA (408)656-2352.

Please note that, although authors are permitted to re-use all or portions of their ACES copyrighted material in other works, this does not include granting third party requests for reprinting, republishing, or other types of re-use.

JOINT AUTHORSHIP

For jointly authored papers, only one signature is required, but we assume all authors have been advised and have consented to the terms of this form.

U.S. GOVERNMENT EMPLOYEES

Authors who are U.S. Government employees are not required to sign the Copyright Transfer Form (Part A), but any co-authors outside the Government are.

Part B of the form is to be used instead of Part A only if all authors are U.S. Government employees and prepared the paper as part of their job.

NOTE RE GOVERNMENT CONTRACT WORK: Authors whose work was performed under a U.S. Government contract but who are not Government employees are required so sign Part A-Copyright Transfer Form. However, item 5 of the form returns reproduction rights to the U. S. Government when required, even though ACES copyright policy is in effect with respect to the reuse of material by the general public.

January 2002

INFORMATION FOR AUTHORS

PUBLICATION CRITERIA

Each paper is required to manifest some relation to applied computational electromagnetics. **Papers may address general issues in applied computational electromagnetics, or they may focus on specific applications, techniques, codes, or computational issues.** While the following list is not exhaustive, each paper will generally relate to at least one of these areas:

- 1. Code validation.** This is done using internal checks or experimental, analytical or other computational data. Measured data of potential utility to code validation efforts will also be considered for publication.
- 2. Code performance analysis.** This usually involves identification of numerical accuracy or other limitations, solution convergence, numerical and physical modeling error, and parameter tradeoffs. However, it is also permissible to address issues such as ease-of-use, set-up time, run time, special outputs, or other special features.
- 3. Computational studies of basic physics.** This involves using a code, algorithm, or computational technique to simulate reality in such a way that better, or new physical insight or understanding, is achieved.
- 4. New computational techniques** or new applications for existing computational techniques or codes.
- 5. "Tricks of the trade"** in selecting and applying codes and techniques.
- 6. New codes, algorithms, code enhancement, and code fixes.** This category is self-explanatory, but includes significant changes to existing codes, such as applicability extensions, algorithm optimization, problem correction, limitation removal, or other performance improvement. **Note: Code (or algorithm) capability descriptions are not acceptable, unless they contain sufficient technical material to justify consideration.**
- 7. Code input/output issues.** This normally involves innovations in input (such as input geometry standardization, automatic mesh generation, or computer-aided design) or in output (whether it be tabular, graphical, statistical, Fourier-transformed, or otherwise signal-processed). Material dealing with input/output database management, output interpretation, or other input/output issues will also be considered for publication.
- 8. Computer hardware issues.** This is the category for analysis of hardware capabilities and limitations of various types of electromagnetics computational requirements. Vector and parallel computational techniques and implementation are of particular interest.

Applications of interest include, but are not limited to, antennas (and their electromagnetic environments), networks, static fields, radar cross section, inverse scattering, shielding, radiation hazards, biological effects, biomedical applications, electromagnetic pulse (EMP), electromagnetic interference (EMI), electromagnetic compatibility (EMC), power transmission, charge transport, dielectric, magnetic and nonlinear materials, microwave components, MEMS, RFID, and MMIC technologies, remote sensing and geometrical and physical optics, radar and communications systems, sensors, fiber optics, plasmas, particle accelerators, generators and motors, electromagnetic wave propagation, non-destructive evaluation, eddy currents, and inverse scattering.

Techniques of interest include but not limited to frequency-domain and time-domain techniques, integral equation and differential equation techniques, diffraction theories, physical and geometrical optics, method of moments, finite differences and finite element techniques, transmission line method, modal expansions, perturbation methods, and hybrid methods.

Where possible and appropriate, authors are required to provide statements of quantitative accuracy for measured and/or computed data. This issue is discussed in "Accuracy & Publication: Requiring, quantitative accuracy statements to accompany data," by E. K. Miller, *ACES Newsletter*, Vol. 9, No. 3, pp. 23-29, 1994, ISBN 1056-9170.

SUBMITTAL PROCEDURE

All submissions should be uploaded to ACES server through ACES web site (<http://aces.ee.olemiss.edu>) by using the upload button, journal section. Only pdf files are accepted for submission. The file size should not be larger than 5MB, otherwise permission from the Editor-in-Chief should be obtained first. Automated acknowledgment of the electronic submission, after the upload process is successfully completed, will be sent to the corresponding author only. It is the responsibility of the corresponding author to keep the remaining authors, if applicable, informed. Email submission is not accepted and will not be processed.

PAPER FORMAT (INITIAL SUBMISSION)

The preferred format for initial submission manuscripts is 12 point Times Roman font, single line spacing and single column format, with 1 inch for top, bottom, left, and right margins. Manuscripts should be prepared for standard 8.5x11 inch paper.

EDITORIAL REVIEW

In order to ensure an appropriate level of quality control, papers are peer reviewed. They are reviewed both for

technical correctness and for adherence to the listed guidelines regarding information content and format.

PAPER FORMAT (FINAL SUBMISSION)

Only camera-ready electronic files are accepted for publication. The term “**camera-ready**” means that the material is neat, legible, reproducible, and in accordance with the final version format listed below.

The following requirements are in effect for the final version of an ACES Journal paper:

1. The paper title should not be placed on a separate page. The title, author(s), abstract, and (space permitting) beginning of the paper itself should all be on the first page. The title, author(s), and author affiliations should be centered (center-justified) on the first page. The title should be of font size 16 and bolded, the author names should be of font size 12 and bolded, and the author affiliation should be of font size 12 (regular font, neither italic nor bolded).
2. An abstract is required. The abstract should be a brief summary of the work described in the paper. It should state the computer codes, computational techniques, and applications discussed in the paper (as applicable) and should otherwise be usable by technical abstracting and indexing services. The word “Abstract” has to be placed at the left margin of the paper, and should be bolded and italic. It also should be followed by a hyphen (–) with the main text of the abstract starting on the same line.
3. All section titles have to be centered and all the title letters should be written in caps. The section titles need to be numbered using roman numbering (I. II.)
4. Either British English or American English spellings may be used, provided that each word is spelled consistently throughout the paper.
5. Internal consistency of references format should be maintained. As a guideline for authors, we recommend that references be given using numerical numbering in the body of the paper (with numerical listing of all references at the end of the paper). The first letter of the authors’ first name should be listed followed by a period, which in turn, followed by the authors’ complete last name. Use a coma (,) to separate between the authors’ names. Titles of papers or articles should be in quotation marks (“ ”), followed by the title of journal, which should be in italic font. The journal volume (vol.), issue number (no.), page numbering (pp.), month and year of publication should come after the journal title in the sequence listed here.
6. Internal consistency shall also be maintained for other elements of style, such as equation numbering. As a guideline for authors who have no other preference, we suggest that equation numbers be placed in parentheses at the right column margin.

7. The intent and meaning of all text must be clear. For authors who are not masters of the English language, the ACES Editorial Staff will provide assistance with grammar (subject to clarity of intent and meaning). However, this may delay the scheduled publication date.
8. Unused space should be minimized. Sections and subsections should not normally begin on a new page.

ACES reserves the right to edit any uploaded material, however, this is not generally done. It is the author(s) responsibility to provide acceptable camera-ready pdf files. Incompatible or incomplete pdf files will not be processed for publication, and authors will be requested to re-upload a revised acceptable version.

COPYRIGHTS AND RELEASES

Each primary author must sign a copyright form and obtain a release from his/her organization vesting the copyright with ACES. Copyright forms are available at ACES, web site (<http://aces.ee.olemiss.edu>). To shorten the review process time, the executed copyright form should be forwarded to the Editor-in-Chief immediately after the completion of the upload (electronic submission) process. Both the author and his/her organization are allowed to use the copyrighted material freely for their own private purposes.

Permission is granted to quote short passages and reproduce figures and tables from an ACES Journal issue provided the source is cited. Copies of ACES Journal articles may be made in accordance with usage permitted by Sections 107 or 108 of the U.S. Copyright Law. This consent does not extend to other kinds of copying, such as for general distribution, for advertising or promotional purposes, for creating new collective works, or for resale. The reproduction of multiple copies and the use of articles or extracts for commercial purposes require the consent of the author and specific permission from ACES. Institutional members are allowed to copy any ACES Journal issue for their internal distribution only.

PUBLICATION CHARGES

All authors are allowed for 8 printed pages per paper without charge. Mandatory page charges of \$75 a page apply to all pages in excess of 8 printed pages. Authors are entitled to one, free of charge, copy of the journal issue in which their paper was published. Additional reprints are available for a nominal fee by submitting a request to the managing editor or ACES Secretary.

Authors are subject to fill out a one page over-page charge form and submit it online along with the copyright form before publication of their manuscript.

ACES Journal is abstracted in INSPEC, in Engineering Index, DTIC, Science Citation Index Expanded, the Research Alert, and to Current Contents/Engineering, Computing & Technology.